

EX-DESY-Zeuthen 96-03
sw 96 14

**Interner Bericht
DESY-Zeuthen 96-03
März 1996**

CERN LIBRARIES, GENEVA



CM-P00080939

**A Measurement of the Michel Parameters and
 ν_τ Helicity in τ Lepton Decays
with the L3 Detector at LEP**

Pavel Anatolievitch Kapinos

Thesis-1996-Kapinos

DESY behält sich alle Rechte für den Fall der Schutzrechtserteilung und für die wirtschaftliche Verwertung der in diesem Bericht enthaltenen Informationen vor.

DESY reserves all rights for commercial use of information included in this report, especially in case of filing application for or grant of patents.

**"Die Verantwortung für den Inhalt dieses
Internen Berichtes liegt ausschließlich beim Verfasser"**

**A Measurement of the Michel Parameters and ν_τ Helicity
in τ Lepton Decays with the L3 Detector at LEP**

Dissertation

zur Erlangung des akademischen Grades

Doctor rerum naturalium

(Dr. rer. nat.)

eingereicht an der

Mathematisch-Naturwissenschaftlichen Fakultät-I

Institut für Physik

der Humboldt-Universität zu Berlin

von

Dipl.-Physiker Pavel Anatolievitch Kapinos

geboren am 27 Juni 1964 in Brest (Weißrußland)

Präsidentin der Humboldt-Universität zu Berlin

Prof. Dr. M. Dürkop

Dekan des Fachbereichs Physik

Prof. Dr. M. v. Ortenberg

Gutachter: 1. Prof. Dr. T. Hebbeker
 2. Prof. Dr. T. Lohse
 3. Prof. Dr. P. Söding

Tag der mündlichen Prüfung: 12.02.96

Abstract

This thesis reports on the measurement of Michel parameters ρ_l , η_l , ξ_l , $\delta_l\xi_l$ and the average ν_τ helicity $\langle h_{\nu_\tau} \rangle$ in τ lepton decays with the L3 detector. The $\tau^+\tau^-$ pairs were produced by the LEP e^+e^- collider, located at the European Center for Particle Physics (CERN). The data sample consists of 69 pb^{-1} integrated luminosity collected during the 1991, 1992 and 1993 collider runs with \sqrt{s} ranging from 88.5 GeV to 93.7 GeV.

The values of ρ_l , η_l , ξ_l , $\delta_l\xi_l$ and $\langle h_{\nu_\tau} \rangle$ are extracted together with the average τ lepton polarization P_τ from a simultaneous fit to the distributions of the τ pair decay products in the following channels: $e^+e^- \rightarrow \gamma/Z^0 \rightarrow \tau^+\tau^- \rightarrow ee, e\mu, e\pi, e\rho, eX, \mu\pi, \mu\rho, \mu X, \pi\pi, \pi\rho, \pi X, \rho\rho, \rho X$, where X designates a τ decay not identified as e, μ, π or ρ . Using 32138 events, selected in the above channels, and assuming universality in the τ lepton decays, the measured values are

$$\begin{aligned}\rho_l &= 0.794 \pm 0.039 \pm 0.035 \\ \eta_l &= 0.25 \pm 0.17 \pm 0.11 \\ \xi_l &= 0.94 \pm 0.21 \pm 0.07 \\ \xi_l\delta_l &= 0.81 \pm 0.14 \pm 0.07 \\ \langle h_{\nu_\tau} \rangle &= -0.970 \pm 0.053 \pm 0.016 \\ P_\tau &= -0.154 \pm 0.018 \pm 0.015\end{aligned}$$

where the first error is statistical and the second error is systematic.

The measured values of ρ_l , η_l , ξ_l , $\delta_l\xi_l$ and $\langle h_{\nu_\tau} \rangle$ are in agreement with the $V-A$ structure of the weak charged current interaction in the τ lepton decays.

Contents

1	Introduction	1
2	Standard Electroweak Model	3
2.1	Historical Overview	3
2.2	Structure of weak charged current	5
2.3	Main features of the Standard Electroweak Model	7
2.4	Physical observables in the process $e^+e^- \rightarrow \tau^+\tau^-$	11
2.5	Input parameters and radiative corrections	15
3	Tau Lepton	20
3.1	Discovery and brief history	20
3.2	Main properties of τ lepton and ν_τ	21
3.3	Lorentz structure of the τ lepton decays	22
3.3.1	Leptonic decays	22
3.3.2	Semileptonic decays	25
3.4	Correlated decay distributions	26
4	Analysis Method	31
4.1	Decay Distributions	32
4.1.1	Leptonic decays	32
4.1.2	Semileptonic decays	37
4.2	Global Fit Procedure	41
5	L3 detector at LEP	47
5.1	LEP	47
5.2	The L3 detector	49
5.2.1	General description	49
5.2.2	Magnet	50
5.2.3	Muon Spectrometer	51
5.2.4	Hadron Calorimeter	54
5.2.5	Scintillation Counters	57

5.2.6	Electromagnetic calorimeter	57
5.2.7	Central Tracking System	60
5.2.8	Luminosity Monitor	64
5.2.9	Data Acquisition System and Trigger	65
5.2.10	Event Reconstruction	69
5.2.11	Detector Simulation	71
6	Data Analysis	72
6.1	Dilepton Preselection	72
6.2	Particle Identification	75
6.2.1	Electromagnetic and hadronic shower profiles in the BGO	75
6.2.2	Electron Identification	77
6.2.3	Muon Identification	79
6.2.4	Photon reconstruction and π^0 identification	82
6.2.5	Identification of $\tau \rightarrow \pi(K)\nu$ decay	84
6.2.6	Identification of $\tau \rightarrow \rho\nu$ decay	86
6.3	Event Selection	87
6.4	Energy Resolution and Calibration	93
6.4.1	Muon Momentum Measurement	93
6.4.2	Electromagnetic Energy Measurement	96
6.4.3	Charged Pion Energy Measurement	97
7	Measurement	101
7.1	The Likelihood Function	101
7.2	Fit Results	107
7.3	Systematic Errors	110
8	Conclusions	124
8.1	Results	124
8.2	Outlook and Prospects	125

List of Figures

2.1	A correspondence of the sign of helicity to the handedness of the fermion and antifermion in the relativistic limit.	6
2.2	Interaction vertex for the fermion in the case of scalar (S), pseudoscalar (P), vector (V), axial-vector (A) and tensor (T) types of interaction.	7
2.3	Weak charged current interaction vertex for the fermion.	9
2.4	Electromagnetic current interaction vertex for the fermion.	10
2.5	Weak neutral current interaction vertex for the fermion.	11
2.6	Tree level Feynman diagram of the process $e^+e^- \rightarrow \tau^+\tau^-$	12
2.7	Helicity configurations of the initial and final state fermions in the process $e^+e^- \rightarrow \tau^+\tau^-$, allowed by helicity conservation in the relativistic limit.	14
2.8	Pure QED radiative corrections to the process $e^+e^- \rightarrow \tau^+\tau^-$ due to the initial-state and final-state radiation.	17
2.9	High-order electroweak corrections to the process $e^+e^- \rightarrow \tau^+\tau^-$ due to the propagator corrections, vertex corrections and box diagrams.	17
2.10	The effect of radiative corrections (R.C.) on A_{FB} and P_τ for leptons. The curves are calculated using analytical calculations from the ZFITTER program [26].	18
4.1	Spectral functions $h_0, h_\rho, h_\xi, h_{\xi\delta}$ of the $\tau \rightarrow e\bar{\nu}_e\nu_\tau$ decay shown as histograms, obtained with the KORALZ generator [62] and the modified TAUOLA matrix element [64]. Superimposed solid lines represent Born level calculations.	34
4.2	Spectral functions $h_0, h_\eta, h_\rho, h_\xi, h_{\xi\delta}$ of the $\tau \rightarrow \mu\bar{\nu}_\mu\nu_\tau$ decay shown as histograms, obtained with the KORALZ generator [62] and the modified TAUOLA matrix element [64]. Superimposed solid lines represent Born level calculations.	35
4.3	The ratio of equally normalized h_η and h_0 spectral functions (in Born level) of the $\tau \rightarrow \mu\bar{\nu}_\mu\nu_\tau$ decay shows relative sensitivity of polarization independent part of the muon spectrum to η parameter.	36

4.4	Spectral functions h_0 and h_1 of $\tau \rightarrow \pi\nu_\tau$ decay shown as histograms, obtained with the KORALZ generator [62]. Their difference $h_0 - h_1$ and the sum $h_0 + h_1$ give the π spectrum from <i>left-handed</i> and <i>right-handed</i> τ decays, respectively. Superimposed solid lines represent Born level calculations.	39
4.5	Spectral functions h_0 and h_1 of $\tau \rightarrow \rho\nu_\tau$ decay shown as histograms, obtained with the KORALZ generator [62]. Their difference $h_0 - h_1$ and the sum $h_0 + h_1$ give the ρ spectrum from <i>left-handed</i> and <i>right-handed</i> τ decays, respectively.	42
5.1	The LEP ring with locations of the four detectors.	48
5.2	Perspective view of the L3 detector.	50
5.3	Layout of the muon spectrometer octant and the drift cells of the P-chambers.	52
5.4	Longitudinal cut view of the hadron calorimeter and muon filter.	54
5.5	$r - \varphi$ and $r - z$ cut view of long module in HCAL barrel with chambers grouped into readout towers.	56
5.6	Longitudinal cut view of the BGO electromagnetic calorimeter showing the projective geometry of the crystal arrangement.	59
5.7	A BGO crystal side view. Two photodiodes are used to measure the light output.	59
5.8	The central tracking system, consisting of TEC (1-6), PSF (7-9) and Z-Detector (10-13) [94].	62
5.9	The wire configuration in one inner and in part of two outer TEC sectors.	62
5.10	Energy trigger segmentation in the $r - \theta$ plane. Elements of the BGO endcaps are not shown.	66
6.1	The distance of closest approach (DCA) of tracks to the nominal beam axis as measured by the TEC. The tracks are from $Z^0 \rightarrow \mu^+\mu^-(\gamma)$ events with two entries per event. The solid line is the result of a gaussian fit to the central part of this distribution.	73
6.2	Scintillator time-of-flight distribution for the same sample used for Figure 6.1. The solid line is the result of a gaussian fit to the central part of this distribution.	74
6.3	Concentric rings used for estimate of expected energy in a BGO crystal from an electromagnetic shower at the depth of one radiation length.	76
6.4	Electromagnetic (a) and hadronic (b) shower profiles in the BGO. A(R) is the normalized energy density.	76

6.5	Displacement in φ between the extrapolation of the TEC track to the BGO surface and the shower maximum in the BGO for golden Bhabha events. The solid line is the result of a gaussian fit to the central part of this distribution.	78
6.6	Displacement in θ between the extrapolation of the TEC track to the BGO surface and the shower maximum in the BGO for golden Bhabha events. The solid line is the result of a gaussian fit to the central part of this distribution.	78
6.7	χ_{mip}^2 for muons from $Z^0 \rightarrow \mu^+\mu^-$ decays in data. All other cuts for muon identification have been applied.	80
6.8	Illustration of the procedure used for neutral cluster reconstruction in the BGO.	83
6.9	The compatibility of the TEC momentum and calorimetric energy measurements for $\tau \rightarrow \pi(K)\nu$ candidate decays after all other cuts have been applied. The arrow indicates the final cut value.	84
6.10	The invariant mass spectrum of two photons for selected $\tau \rightarrow \rho\nu$ decays. It comprises two cases: when both photons are reconstructed as separate neutral clusters in the BGO and when a single neutral cluster is identified as a π^0	85
6.11	The $\pi^\pm\pi^0$ invariant mass distribution. The arrows indicate the range of $M_{\pi^\pm\pi^0}$ accepted for the $\tau \rightarrow \rho\nu$ identification.	86
6.12	An event selected for the $e\mu$ channel.	90
6.13	An event consisting of a pion candidate in the left hemisphere and a candidate for the $\tau \rightarrow \rho\nu$ decay in the right hemisphere.	91
6.14	Identification efficiency in the fiducial volume for the different τ decay modes used in the analysis. $\tau \rightarrow \mu\bar{\nu}\nu$ corresponds to an identified muon traversing at least three layers of the muon spectrometer ("triplets").	94
6.15	The resolution of $1/p_\mu$ for "triplet" muons from $Z^0 \rightarrow \mu\mu$ decays and the BGO energy resolution for electrons in Bhabha events. The solid lines are the results of a gaussian fit to the central part of these distributions.	95
6.16	The muon momentum resolution for "triplets".	96
6.17	The TEC p_t resolution in the barrel as a function of φ_{local} as obtained from dimuon events in 1993. φ_{local} spans a size of one Inner TEC sector, i.e. $\varphi_{local}^{max} = \pi/6$. The leftmost and rightmost dashed vertical lines give the anode positions in Outer TEC. The middle line corresponds to the anode plane in Inner TEC and the cathode plane of Outer TEC.	98
6.18	Average energy resolution for charged pions attained by combining independent measurements of TEC momentum and calorimetric energy.	100

7.1	Functions $h_0, h_\rho, h_\xi, h_{\xi\delta}$ of the decay $\tau \rightarrow e\bar{\nu}_e\nu_\tau$ convoluted with the detector resolution are shown as solid histograms. Superimposed (dotted) histograms represent these functions before the detector resolution has been applied.	103
7.2	Functions $h_0, h_\eta, h_\rho, h_\xi, h_{\xi\delta}$ of the decay $\tau \rightarrow \mu\bar{\nu}_\mu\nu_\tau$ convoluted with the detector resolution are shown as solid histograms. Superimposed (dotted) histograms represent these functions before the detector resolution has been applied.	104
7.3	Functions h_0 and h_1 of the decay $\tau \rightarrow \pi\nu_\tau$ convoluted with the detector resolution are shown as solid histograms. Superimposed (dotted) histograms represent these functions before the detector resolution has been applied. The difference $h_0 - h_1$ and the sum $h_0 + h_1$ give the π spectrum from <i>left-handed</i> and <i>right-handed</i> τ decays, respectively. . .	105
7.4	Shown as solid histograms are the h_0 and h_1 functions of the decay $\tau \rightarrow \rho\nu_\tau$ as obtained from selected Monte Carlo $\tau \rightarrow \rho\nu_\tau$ decays after the full detector simulation and reconstruction have been applied. Superimposed (dotted) histograms represent these functions before the detector resolution has been applied. Their difference $h_0 - h_1$ and the sum $h_0 + h_1$ give the ρ spectrum from <i>left-handed</i> and <i>right-handed</i> τ decays, respectively.	106
7.5	Distributions of x_e for the eX channel and x_μ for the μ X channel. The data are shown as points with statistical error bars. The solid-line histogram represents the result of the fit. Total background is superimposed as a hatched histogram.	111
7.6	Distributions of x_π for the π X channel and ω_ρ for the ρ X channel. The data are shown as points with statistical error bars. The solid-line histogram represents the result of the fit. Total background is superimposed as a hatched histogram.	112
7.7	Distributions of x_e for the ee channel shown for five (four) slices of the distribution on the opposite hemisphere. The data are shown as points with statistical error bars. The solid-line histogram represents the result of the fit. Total background is superimposed as a hatched histogram. . .	113
7.8	Distributions of x_e and x_μ for the e μ channel shown for five slices of the distribution on the opposite hemisphere. The data are shown as points with statistical error bars. The solid-line histogram represents the result of the fit. Total background is superimposed as a hatched histogram. . .	114

7.9	Distributions of x_e and x_π for the $e\pi$ channel shown for five slices of the distribution on the opposite hemisphere. The data are shown as points with statistical error bars. The solid-line histogram represents the result of the fit. Total background is superimposed as a hatched histogram. .	115
7.10	Distributions of x_e and ω_ρ for the $e\rho$ channel shown for five slices of the distribution on the opposite hemisphere. The data are shown as points with statistical error bars. The solid-line histogram represents the result of the fit. Total background is superimposed as a hatched histogram. .	116
7.11	Distributions of x_μ and x_π for the $\mu\pi$ channel shown for five slices of the distribution on the opposite hemisphere. The data are shown as points with statistical error bars. The solid-line histogram represents the result of the fit. Total background is superimposed as a hatched histogram. .	117
7.12	Distributions of x_μ and ω_ρ for the $\mu\rho$ channel shown for five slices of the distribution on the opposite hemisphere. The data are shown as points with statistical error bars. The solid-line histogram represents the result of the fit. Total background is superimposed as a hatched histogram. .	118
7.13	Distributions of x_π for the $\pi\pi$ channel shown for five slices of the distribution on the opposite hemisphere. The data are shown as points with statistical error bars. The solid-line histogram represents the result of the fit. Total background is superimposed as a hatched histogram. . .	119
7.14	Distributions of x_π and ω_ρ for the $\pi\rho$ channel shown for five slices of the distribution on the opposite hemisphere. The data are shown as points with statistical error bars. The solid-line histogram represents the result of the fit. Total background is superimposed as a hatched histogram. .	120
7.15	Distributions of ω_ρ for the $\rho\rho$ channel shown for five slices of the distribution on the opposite hemisphere. The data are shown as points with statistical error bars. The solid-line histogram represents the result of the fit. Total background is superimposed as a hatched histogram. . .	121

List of Tables

2.1	The electrical charge, hypercharge and weak isospin assignments for the fermions in the Standard Electroweak Model.	8
2.2	Contributions from γ -, Z^0 -exchange and their interference to the form-factors in the differential cross section.	13
2.3	Experimental values of the most accurately measured input parameters of the Standard Electroweak Model. The relative uncertainty is given in parts per million (ppm).	16
4.1	A set of generated samples used in obtaining $h_0(x)$, $h_\eta(x)$, $h_\rho(x)$, $h_\xi(x)$ and $h_{\xi\delta}(x)$ function estimators for $\tau \rightarrow e\bar{\nu}_e\nu_\tau$ and $\tau \rightarrow \mu\bar{\nu}_\mu\nu_\tau$ decays. . .	33
4.2	A set of generated samples used for the construction of $h_0(x)$ and $h_1(x)$ estimators in the $\tau \rightarrow \pi(K)\nu_\tau$ and $\tau \rightarrow \rho\nu_\tau$ decays	38
4.3	Results of the fit to the generated spectra, produced with different sets of Michel parameters.	44
4.4	Averaged correlation matrix for the fit of the Set A.	45
6.1	Number of selected events for the considered $Z^0 \rightarrow \tau^+\tau^- \rightarrow AB$ decay channels together with the average acceptance ε and the background from $Z^0 \rightarrow \tau\tau \not\rightarrow AB$ and $Z^0 \not\rightarrow \tau\tau$ sources.	92
7.1	The parameter correlation matrix of the fit, assuming universality in τ decays.	108
7.2	The range of the decay variables and number of selected events for every channel considered in the fit, assuming universality in the τ decays, are shown together with the background fraction, number of fitted bins, number of bins populated by the data and the resulting χ^2 of the fit. .	109
7.3	The parameter correlation matrix of the fit, not assuming universality in τ decays.	110
7.4	Systematic uncertainties on parameters of the fit, assuming universality in the τ decays.	122
7.5	Systematic uncertainties on parameters of the fit, not assuming universality in the τ decays.	122

8.1	Comparison of the results for $\rho_l, \eta_l, \xi_l, \xi_l \delta_l$ and $\xi_h \equiv \langle h_{\nu\tau} \rangle$ of this measurement with other measurements.	126
8.2	Comparison of the results for $\rho, \eta, \xi, \xi \delta$ and ξ_h without assuming universality in τ decays.	127

Acknowledgements

This measurement would not have been possible without all those physicists, engineers and technicians who designed, built and maintained the L3 detector and the LEP collider. It is a pleasure for me to thank all of them.

I would like to thank all my colleagues from the DESY-IfH (Zeuthen) group in the L3 collaboration for their constant support and encouragement during my graduate research contract. My special thanks goes to Dr. Wolfgang Lohmann, who has been a leader of the Zeuthen group in L3. His patience and guidance finally lead to the results presented here.

I wish to thank all people of the τ analysis group for giving me such a nice opportunity to work on τ lepton physics in L3. The quality of the results described here is due to the enormous efforts made by this group on the understanding of the detector and its use for τ physics.

I thank Professor Thomas Hebbeker for his assistance at Humboldt University in Berlin and enlightening discussions.

Finally, I am grateful to Dr. Steven Goldfarb and Ron Moore for their careful reading of the draft of this thesis.

Chapter 1

Introduction

In the standard model of electroweak interaction [1, 2, 3], the $V-A$ form of the weak charged current appears *by construction* to be in agreement with numerous experimental results, including nuclear β -decay, muon decay and the weak interactions of other elementary particles. At the same time, the standard electroweak model implies a universality between three generations of fermions, in particular, lepton universality.

In the case of a muon decay, it has been shown in [4] that the $V-A$ form of the charged leptonic weak interaction follows from, within the experimental errors, a small set of existing experiments, which yield a lower limit for $V-A$ and an upper limit for *all other* types of interactions.

Since its discovery in 1975 at the SPEAR e^+e^- storage ring at SLAC, the τ lepton has been a subject of extensive study, aimed at establishing its nature as a sequential lepton. A measurement of the Lorentz structure of the τ lepton decays is a necessary experimental step towards proving or disproving the $V-A$ hypothesis in the weak charged interaction of the τ lepton.

In the framework of the most general, local, derivative-free four-fermion interaction Hamiltonian, the leptonic τ decay is described by ten complex coupling constants. At present, their values are accessed only through a measurement of Michel parameters ρ , η , ξ and $\delta\xi$, which completely describe the energy spectrum of daughter leptons in pure leptonic τ decays. In the case of $\tau \rightarrow \rho\nu_\tau$ and $\tau \rightarrow \pi\nu_\tau$ decays, knowledge of the hadronic current structure, e.g. from $\pi \rightarrow \mu\bar{\nu}_\mu$ decay, reduces the number of possible types of interactions. Still, the hadronic chirality parameter ξ_h , which gives the average ν_τ helicity in these decays, remains a free parameter.

In this thesis a simultaneous measurement of Michel parameters ρ , η , ξ and $\delta\xi$ of the leptonic τ decays

$$\tau \rightarrow e\bar{\nu}_e\nu_\tau \quad \text{and} \quad \tau \rightarrow \mu\bar{\nu}_\mu\nu_\tau$$

and the hadronic chirality parameter ξ_h of the semi-leptonic τ decays

$$\tau \rightarrow \rho\nu_\tau \quad \text{and} \quad \tau \rightarrow \pi\nu_\tau$$

is presented. This measurement employs correlated distributions of τ pair decay products in the process

$$e^+e^- \rightarrow Z^0 \rightarrow \tau^+\tau^- \rightarrow AB$$

where A and B are both identified as e, μ, π and ρ , along with a single side spectra of τ decays into e, μ, π and ρ when the decay of other τ in an event is not identified for these channels.

The $\tau^+\tau^-$ pairs are produced by the LEP e^+e^- collider and have been detected by the L3 experiment. The data sample used in the analysis consists of about 69 pb^{-1} integrated luminosity collected during the 1991, 1992 and 1993 collider runs at a center-of-mass energies around the Z^0 mass, ranging from 88.5 GeV to 93.7 GeV.

In the next chapter an overview of the lepton sector in the Standard Electroweak Model is given. Then, physical observables in the process $e^+e^- \rightarrow \tau^+\tau^-$, such as a total cross-section, forward-backward and polarization asymmetries as well as the longitudinal spin correlation of the produced τ 's, are derived.

Chapter 3 describes the Lorentz structure of the τ decays. It is shown there how the correlated distributions of the τ decay products result from the longitudinal spin correlation of their parent τ pair.

Chapter 4 explains the method of measuring τ decay parameters together with P_τ from a global fit to the correlated decay spectra and single decay distributions of the τ pair decay products.

Chapter 5 gives a description of the L3 detector at LEP.

Chapter 6 discusses the data analysis, including the preselection of Z^0 decays to charged leptons, the particle identification algorithm used for one-prong τ decays, the final event selection. It contains a summary of the energy measurement for muons, electrons (photons) and charged pions, and attained resolutions.

Chapter 7 is devoted to the measurement of the Michel parameters $\rho, \eta, \xi, \delta\xi$ and the hadronic chirality parameter ξ_h along with the average τ lepton polarization P_τ . It explains how the binned likelihood function is constructed, presents the results, obtained with and without assumption of the universality in the τ decays, and an evaluation of the systematic errors.

Finally, a summary of this measurement is presented and a comparison of the obtained results to other measurements is made.

Throughout this thesis all quantities are expressed in units in which $\hbar = c = 1$.

Chapter 2

Standard Electroweak Model

2.1 Historical Overview

Almost a century ago, in 1898, Lord Rutherford [5] discovered that the so-called Becquerel ray actually consisted of two distinct types of radiation: one that is readily absorbed which he called α -radiation and another of a more penetrating character which he called β -radiation, known today as the β -decay of thorium. The history of the weak interactions began.

As known now, weak interactions are responsible for a large number of various physical processes, e.g. nuclear β -decay, numerous decays of elementary particles, reactions induced by neutrinos. All known leptons and hadrons are subject to the weak interaction. It plays an important role in such astrophysical phenomena as the sun's burning and supernova explosions. Understanding of the weak interactions developed over a long period, from the neutrino hypothesis, suggested by W. Pauli in 1931 to "save" energy conservation in β -decay [6], the celebrated Fermi theory of four-fermion interaction [7], through the suggestion of parity non conservation in any weak interaction made by T. D. Lee and C. N. Yang [8] and successfully confirmed by several decisive experiments in 1957 [9], and the emerging $V-A$ theory [10], which successfully described all the known weak decay process at that time, the end of the 1950's.

But the nature of the weak interaction has been revealed via its unification with the electromagnetic interaction into the electroweak model. The first brick of what would become this model was the formulation of non-Abelian gauge field theory by C. N. Yang and R. L. Mills in 1954 [11]. In the context of the strong nuclear interaction, they generalized the idea of the local gauge invariance to the case of $SU(2)$ isotopic-spin group. Three years later, in 1957, J. Schwinger suggested that leptons also must carry isotopic spin like the strongly interacting particles [12]. With renormalizability as a starting point, S. L. Glashow proposed in 1961 a model of unified weak and electromagnetic interactions incorporating Yang-Mills gauge symmetry [1]. In his model the weak in-

teractions are mediated by massive charged vector bosons, W^+ and W^- , and a new neutral current weak interaction is proposed, which is mediated by a massive neutral vector boson, Z . Masses of the gauge bosons are put by hand. Unfortunately, the model turned out not to be renormalizable for the case of massive gauge bosons.

A method for generating gauge boson masses has been proposed by P. W. Higgs [13]. In the field theory with global symmetries, it was known that if the vacuum state does not respect the original symmetry, then additional massless particles known as Goldstone bosons occur. P. W. Higgs showed that if the original theory is locally gauge invariant, then the Goldstone bosons are not present. Instead, originally massless gauge bosons can acquire a mass by what is now known as the Higgs mechanism. This mechanism is known as well as “spontaneous symmetry breaking” because it did not require any explicit mass terms in the Lagrangian to manifestly violate gauge invariance. The price paid for generating gauge boson masses this way is the appearance of massive scalars – Higgs bosons.

In 1967 S. Weinberg published a model of leptons using the idea of spontaneously broken gauge symmetry [2]. The difference with the Glashow model was that the W^\pm and Z gauge bosons acquired their masses via the Higgs mechanism. Furthermore, it provided a relationship between the couplings of the as yet unobserved neutral current interaction and the Z boson mass. Almost simultaneously, A. Salam [3] independently proposed the same model. The weak and electromagnetic interactions have been unified under a combined gauge group which is denoted by the product $SU(2)_L \otimes U(1)_Y$. Aside from the fact that the weak neutral current had not been observed, the model faced two serious obstacles. Firstly, it did not attempt to describe the weak interactions of hadrons. Secondly, it was not known whether Yang-Mills theories were renormalizable.

An extension of weak interaction to the quarks was made by S. L. Glashow, J. Iliopoulos and L. Maiani in 1970 [14], by introducing the fourth quark – charm. The observation that the symmetry between leptons and quarks requires the existence of the fourth quark was made already by M. Gell-Mann in 1964 [15]. The Glashow-Weinberg-Salam model was placed on solid theoretical ground when G. 't Hooft published a proof of the renormalizability of the spontaneously broken gauge theories in 1971 [16].

The first observation of weak neutral current events of type $\bar{\nu}_\mu e^- \rightarrow \bar{\nu}_\mu e^-$ in 1973 at CERN was key in establishing the validity of the theory [17]. Direct confirmation of the Standard Electroweak Model came in 1983 with the discovery of W^\pm and Z^0 bosons with the predicted masses by UA1 and UA2 experiments at CERN SPS collider [18].

2.2 Structure of weak charged current

The Lorentz structure of the weak charged current is crucial for the construction of the Standard Electroweak Model.

At low energies all weak charged processes are well described by the effective four-fermion lagrangian [19, 20]:

$$\mathcal{L} = \frac{4G_F}{\sqrt{2}} J^\mu J_\mu^+ \quad (2.1)$$

with the current J^μ having the following form

$$J^\mu = \bar{u}\gamma^\mu \frac{1}{2}(1 - \gamma^5)v, \quad (2.2)$$

where v and u are the spinors of the initial and final particles, $\bar{u} = u^\dagger \gamma^0$ the conjugate bispinor, $\gamma^\mu = (\gamma^0, \boldsymbol{\gamma})$ Dirac matrices and $\gamma^5 = i\gamma^0\gamma^1\gamma^2\gamma^3$ [19]. The form of (2.2) is, apparently, the difference between a vector $\bar{u}\gamma^\mu v$ (V) and an axial-vector $\bar{u}\gamma^\mu\gamma^5 v$ (A), referred as $V-A$ interaction. In virtue of the anticommunication of the γ^5 and γ^μ matrices and $(\gamma^5)^2 = 1$,

$$J^\mu = \bar{u}\gamma^\mu \frac{1}{2}(1 - \gamma^5)v = \bar{u} \frac{1}{2}(1 + \gamma^5)\gamma^\mu \frac{1}{2}(1 - \gamma^5)v = \bar{u}_L \gamma^\mu v_L, \quad (2.3)$$

where

$$v_L \equiv \frac{1 - \gamma^5}{2}v \quad \text{and} \quad \bar{u}_L \equiv \bar{u} \frac{1 + \gamma^5}{2}. \quad (2.4)$$

The suffix L indicates that v_L and \bar{u}_L are the left-handed components of the Dirac bispinors. Thus, the $V-A$ structure of weak charged current means that only left-handed components of spinors are involved in the interaction. Due to its $V-A$ structure, the charged current interaction violates space and charge symmetries [19, 20]. In order to clarify physical meaning of the *handedness* (or *chirality*), consider a bispinor

$$u = \begin{pmatrix} \varphi \\ \chi \end{pmatrix}, \quad (2.5)$$

which satisfies the Dirac equation

$$(\hat{p} - m)u = (E\gamma^0 - \mathbf{p}\boldsymbol{\gamma} - m)u = 0. \quad (2.6)$$

Using the explicit Dirac-Pauli representation of the γ matrices

$$\gamma^0 = \begin{pmatrix} 1 & 0 \\ 0 & -1 \end{pmatrix}, \quad \boldsymbol{\gamma} = \begin{pmatrix} 0 & \boldsymbol{\sigma} \\ -\boldsymbol{\sigma} & 0 \end{pmatrix}, \quad \gamma^5 = i\gamma^0\gamma^1\gamma^2\gamma^3 = \begin{pmatrix} 0 & 1 \\ 1 & 0 \end{pmatrix}, \quad (2.7)$$

where $\boldsymbol{\sigma}$ are 2×2 Pauli matrices, the equation (2.6) yields a relationship between φ and χ :

$$\chi = \frac{\boldsymbol{\sigma}\mathbf{p}}{E + m}\varphi \quad (2.8)$$

and the left-handed spinor contains only the $\varphi - \chi$ combination and not $\varphi + \chi$:

$$u_L \equiv \frac{1 - \gamma^5}{2} u = \frac{1}{2} \begin{pmatrix} 1 & -1 \\ -1 & 1 \end{pmatrix} \begin{pmatrix} \varphi \\ \chi \end{pmatrix} = \frac{1}{2} \begin{pmatrix} \varphi - \chi \\ \chi - \varphi \end{pmatrix}. \quad (2.9)$$

Taking the expression (2.8) for χ ,

$$\varphi - \chi = \left(1 - \frac{\boldsymbol{\sigma} \mathbf{p}}{E + m} \right) \varphi, \quad (2.10)$$

which in the relativistic limit ($E \gg m$, $\beta = |\mathbf{p}|/E \rightarrow 1$) and in the coordinate system with z -axis along the direction of the particle motion $\mathbf{n} = \mathbf{p}/|\mathbf{p}|$ approaches very simple form

$$\varphi - \chi = \left(1 - \frac{\boldsymbol{\sigma} \mathbf{p}}{E + m} \right) \varphi \rightarrow (1 - \boldsymbol{\sigma} \mathbf{n}) \varphi = (1 - \sigma_z) \varphi = 2 \begin{pmatrix} 0 & 0 \\ 0 & 1 \end{pmatrix} \varphi. \quad (2.11)$$

$$\begin{array}{l} \boldsymbol{\sigma} \cdot \mathbf{p} < 0 \quad \overleftarrow{\hspace{1.5cm}} \hspace{0.5cm} \longrightarrow \quad u_L; \bar{u}_R \\ \boldsymbol{\sigma} \cdot \mathbf{p} > 0 \quad \overrightarrow{\hspace{1.5cm}} \hspace{0.5cm} \longrightarrow \quad u_R; \bar{u}_L \end{array}$$

Figure 2.1: A correspondence of the sign of helicity to the handedness of the fermion and antifermion in the relativistic limit.

Now notice, that the two-component spinor $\varphi_\uparrow = \begin{pmatrix} 1 \\ 0 \end{pmatrix}$ describes fermion with a spin along z -axis, and $\varphi_\downarrow = \begin{pmatrix} 0 \\ 1 \end{pmatrix}$ describes fermion with a spin opposite to z -axis. It appears that $u_L = 0$ if $\varphi = \varphi_\uparrow$, and $u_L \neq 0$ if $\varphi = \varphi_\downarrow$. Thus, u_L represents a particle with a spin in the direction opposite to its momentum, or having negative helicity (Figure 2.1). A left-handed conjugate bispinor \bar{u}_L in the relativistic limit represents a particle with a spin along its momentum, or having positive helicity (Figure 2.1).

For the sake of completeness, here it is the definition of right-handed component of the Dirac bispinors:

$$u_R \equiv \frac{1 + \gamma^5}{2} u \quad \text{and} \quad \bar{u}_R \equiv \bar{u} \frac{1 - \gamma^5}{2}. \quad (2.12)$$

By the same procedure, outlined above, it is straightforward to show that u_R (\bar{u}_R) represents a particle with a spin along (opposite to) the direction of its momentum (Figure 2.1).

It can be shown from Lorentz invariance that there are only five possible forms of current, which can be involved in the effective four-fermion interaction [20]. They have the following forms and are named after their Lorentz transformation properties:

$$\bar{u} v = \bar{u}_L v_R + \bar{u}_R v_L \quad (\text{scalar}) \quad (2.13)$$

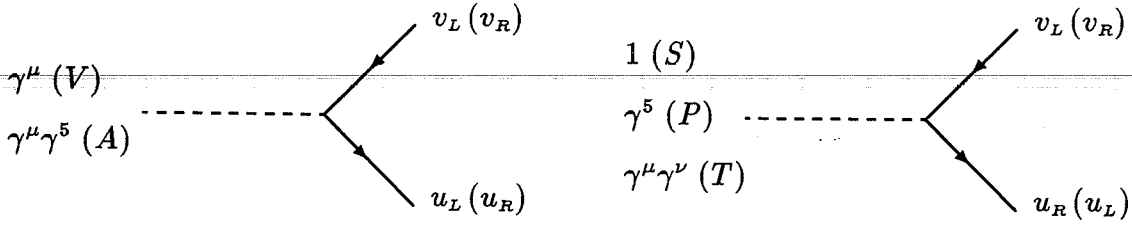


Figure 2.2: Interaction vertex for the fermion in the case of scalar (S), pseudoscalar (P), vector (V), axial-vector (A) and tensor (T) types of interaction.

$$\bar{u}\gamma^5 v = \bar{u}_L v_R - \bar{u}_R v_L \quad (\text{pseudoscalar}) \quad (2.14)$$

$$\bar{u}\gamma^\mu v = \bar{u}_L \gamma^\mu v_L + \bar{u}_R \gamma^\mu v_R \quad (\text{vector}) \quad (2.15)$$

$$\bar{u}\gamma^\mu \gamma^5 v = \bar{u}_R \gamma^\mu v_R - \bar{u}_L \gamma^\mu v_L \quad (\text{axial-vector}) \quad (2.16)$$

$$\bar{u}\gamma^\mu \gamma^\nu v = \bar{u}_L \gamma^\mu \gamma^\nu v_R + \bar{u}_R \gamma^\mu \gamma^\nu v_L \quad (\text{tensor}). \quad (2.17)$$

As it is seen from their definitions in terms of the fermions with definite handedness, vector and axial-vector interactions preserve, whereas scalar, pseudoscalar and tensor interactions flip the handedness (chirality) of the interacting fermions (Figure 2.2).

2.3 Main features of the Standard Electroweak Model

The fermion sector of the Standard Electroweak Model has been constructed to be consistent with the following assumptions derived from the available experimental data:

1. the weak charged current interaction has a $V-A$ form;
2. neutrinos are massless;
3. there is an absence of a flavor changing neutral current between the known fermions ¹.

The success of the $V-A$ form of the weak charged interaction suggests that the left-handed fermions form $SU(2)$ doublets. The minimal choice for the right-handed fermions is that they form $SU(2)$ singlets. Hence, the fermions are arranged in three generations, with left-handed weak isospin doublets and right-handed weak isospin singlets. Due to the absence of lepton flavor violation, the leptonic weak eigenstates correspond to the mass eigenstates. The weak eigenstates of ‘down’ (or ‘up’) type quarks, on the other hand, are mixed with respect to their mass eigenstates to allow

¹This section follows the treatment of the subject given in [20].

<i>Fermions</i>	<i>Generations</i>			<i>Q</i>	<i>Y</i>	<i>T</i>	<i>T₃</i>
Leptons	$\begin{pmatrix} \nu_e \\ e^- \end{pmatrix}_L$	$\begin{pmatrix} \nu_\mu \\ \mu^- \end{pmatrix}_L$	$\begin{pmatrix} \nu_\tau \\ \tau^- \end{pmatrix}_L$	0	-1	1/2	+1/2
	e^-_R	μ^-_R	τ^-_R	-1	-1	1/2	-1/2
				-1	-2	0	0
Quarks	$\begin{pmatrix} u \\ d' \end{pmatrix}_L$	$\begin{pmatrix} c \\ s' \end{pmatrix}_L$	$\begin{pmatrix} t \\ b' \end{pmatrix}_L$	+2/3	+1/3	1/2	+1/2
	u_R	c_R	t_R	+2/3	+4/3	0	0
	d'_R	s'_R	b'_R	-1/3	-2/3	0	0

Table 2.1: The electrical charge, hypercharge and weak isospin assignments for the fermions in the Standard Electroweak Model.

each ‘up’ quark to interact with each ‘down’ quark, in what is observed as weak decays of hyperons, charmed and beauty hadrons. Weak interaction between quarks is assumed to be ‘color blind’.

The gauge symmetry group $SU(2)_L \otimes U(1)_Y$ is chosen so that the charged current interaction is contained in the $SU(2)_L$ group of weak isospin, while the third component of weak isospin and the $U(1)_Y$ group of weak hypercharge, which transforms as weak isosinglet, mix to give the electromagnetic and the weak neutral current interactions. Hence, there is the isotriplet of weak currents

$$J_i^\mu = \bar{\chi}_L \gamma^\mu \frac{\tau_i}{2} \chi_L, \quad (2.18)$$

where τ_i , $i = 1, 2, 3$ are the Pauli matrices, interacting only with left-handed fermions

$$\chi_L = \begin{pmatrix} \nu_{eL} \\ e^-_L \end{pmatrix}, \quad (2.19)$$

and the current of weak hypercharge

$$j_Y^\mu = \bar{\psi} \gamma^\mu Y \psi, \quad (2.20)$$

where the generator Y of the $U(1)_Y$ group of weak hypercharge is defined by the operator of electric charge and the third component of the weak isospin as

$$Q = T_3 + \frac{Y}{2}, \quad (2.21)$$

interacting with both chirality states of the fermions

$$\psi = \begin{pmatrix} \nu_{eL} \\ e^-_L \\ e^-_R \end{pmatrix}. \quad (2.22)$$

From (2.21), the electromagnetic current is given by

$$j_{em}^\mu = J_3^\mu + \frac{j_Y^\mu}{2}. \quad (2.23)$$

Weak isospin and weak hypercharge assignments of the fermions are summarized in Table 2.1.

Before spontaneous symmetry breaking, local gauge invariance results in the interaction of the massless gauge fields of the $SU(2)_L \otimes U(1)_Y$ group with the currents of weak isospin and weak hypercharge:

$$-igJ_i^\mu W_{i\mu} - i\frac{g'}{2}j_Y^\mu B_\mu, \quad (2.24)$$

where $W_{i\mu}$ is the $SU(2)_L$ isotriplet of gauge fields with coupling g to the weak isospin current, and B_μ is the $U(1)_Y$ gauge field with coupling $\frac{1}{2}g'$ to the weak hypercharge current.

After spontaneous breaking of local gauge invariance, the fields

$$W_\mu^\pm = \frac{1}{\sqrt{2}}(W_{1\mu} \mp iW_{2\mu}) \quad (2.25)$$

acquire masses and become charged bosons of the weak charged current interaction (see Figure 2.3).

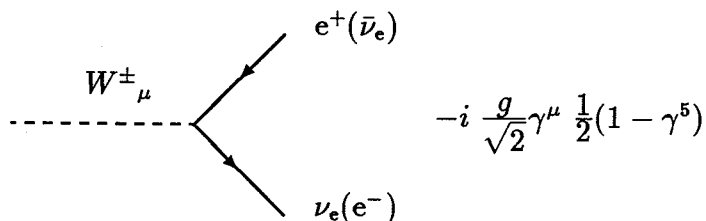


Figure 2.3: Weak charged current interaction vertex for the fermion.

By requiring the matrix element of weak charged current process to agree with tree level calculations in $V-A$ theory, e.g. muon life time, g coupling could be expressed through the Fermi constant G_F and mass of the W^\pm boson M_W :

$$g^2 = \frac{8G_F M_W^2}{\sqrt{2}}. \quad (2.26)$$

The neutral fields $W_{3\mu}$ and B_μ are mixed, resulting in one massless field identified with the electromagnetic interaction and one massive field identified with the weak

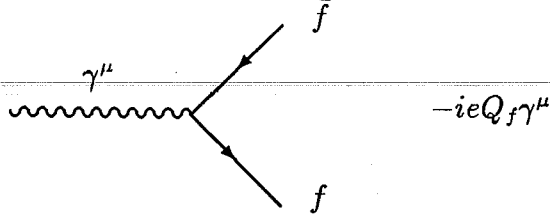


Figure 2.4: Electromagnetic current interaction vertex for the fermion.

neutral current interaction. In terms of the massless fields $W_{3\mu}$ and B_μ , the new physical fields are expressed as

$$A_\mu = B_\mu \cos \theta_W + W_{3\mu} \sin \theta_W \quad (\text{massless}) \quad (2.27)$$

$$Z_\mu = -B_\mu \sin \theta_W + W_{3\mu} \cos \theta_W \quad (\text{massive}), \quad (2.28)$$

where θ_W is the so-called weak mixing angle. The expression for the electroweak neutral current interaction can then be written as

$$\begin{aligned} -igJ_3^\mu W_{3\mu} - i\frac{g'}{2}j_Y^\mu B_\mu &= -i \left(g \sin \theta_W J_3^\mu + g' \cos \theta_W \frac{j_Y^\mu}{2} \right) A_\mu \\ &\quad -i \left(g \cos \theta_W J_3^\mu - g' \sin \theta_W \frac{j_Y^\mu}{2} \right) Z_\mu. \end{aligned} \quad (2.29)$$

If the electromagnetic interaction $-iej_{em}^\mu A_\mu$ is to be identified with the massless photon field A_μ , then

$$g \sin \theta_W = g' \cos \theta_W = e, \quad (2.30)$$

where e is the electromagnetic coupling constant. Thus all interactions of the gauge fields are defined by the electron charge and only one free parameter – the weak mixing angle.

The massive field is responsible for the weak neutral current interaction and, using (2.30) and (2.23), it can be written

$$-i \left(g \cos \theta_W J_3^\mu - g' \sin \theta_W \frac{j_Y^\mu}{2} \right) Z_\mu = -i \frac{g}{\cos \theta_W} (J_3^\mu - \sin^2 \theta_W j_{em}^\mu) Z_\mu, \quad (2.31)$$

where the weak neutral current is identified as

$$J_{NC}^\mu = J_3^\mu - \sin^2 \theta_W j_{em}^\mu. \quad (2.32)$$

For a given fermion f , with the third component of weak isospin T_3 and electric charge Q , this expression becomes

$$J_{NC}^\mu = T_3 \bar{f}_L \gamma^\mu f_L - Q \sin^2 \theta_W \bar{f} \gamma^\mu f \quad (2.33)$$

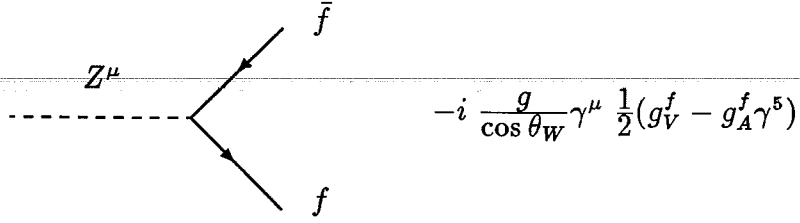


Figure 2.5: Weak neutral current interaction vertex for the fermion.

$$= \bar{f} \gamma^\mu \frac{1}{2} \left[(T_3 - 2Q \sin^2 \theta_W) - T_3 \gamma^5 \right] f \quad (2.34)$$

$$= \bar{f} \gamma^\mu \frac{1}{2} (g_V - g_A \gamma^5) f = \frac{g_V + g_A}{2} \bar{f}_L \gamma^\mu f_L + \frac{g_V - g_A}{2} \bar{f}_R \gamma^\mu f_R, \quad (2.35)$$

where it has been introduced the weak neutral current couplings of the fermion:

$$g_V = T_3 - 2Q \sin^2 \theta_W \quad (2.36)$$

$$g_A = T_3. \quad (2.37)$$

The weak neutral current (2.35) is diagonal, i.e. it transforms fermions only into themselves, and for charged fermions ($Q \neq 0$) it contains right-handed components along with left-handed components of spinors, as $g_V^f \neq g_A^f$.

The spontaneous symmetry breaking mechanism provides a relationship between the weak mixing angle θ_W and the masses of the weak gauge bosons W^\pm and Z . To lowest order in the Standard Electroweak Model:

$$\rho \equiv \frac{M_W^2}{M_Z^2 \cos^2 \theta_W} = 1. \quad (2.38)$$

Combining (2.26), (2.30) and (2.38), an expression for the weak mixing angle in terms of the fine-structure constant $\alpha = e^2/4\pi$, the Fermi constant G_F and the mass of the Z^0 boson at the Born level reads:

$$\sin^2 \theta_W \cos^2 \theta_W = \frac{\pi \alpha}{\sqrt{2} G_F M_Z^2}. \quad (2.39)$$

Thus, given measurements of α , G_F , M_Z^2 and $\sin^2 \theta_W$, the weak neutral couplings, g_V and g_A , can be determined for the various fermions.

2.4 Physical observables in the process $e^+ e^- \rightarrow \tau^+ \tau^-$

To lowest order in perturbation theory, the amplitude of the process

$$e^-(k_1) + e^+(k_2) \rightarrow \tau^-(p_1, s_1) + \tau^+(p_2, s_2) \quad (2.40)$$

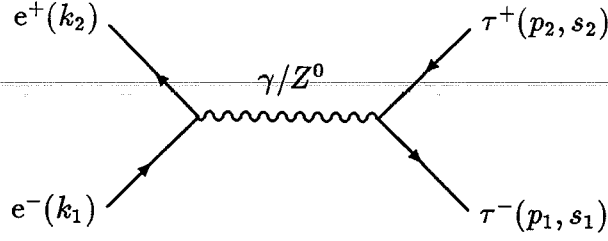


Figure 2.6: Tree level Feynman diagram of the process $e^+e^- \rightarrow \tau^+\tau^-$.

is given in the Standard Electroweak Model by the sum of the contributions associated with γ - and Z^0 -exchanges (Figure 2.6). A contribution from the Higgs boson exchange is neglected, due to the relative smallness of its Yukawa couplings to the electron. Then, the amplitude yields [21, 22]

$$\begin{aligned} \mathcal{M} = & i \frac{4\pi\alpha}{s} q_e q_\tau \bar{v}(k_2) \gamma_\mu u(k_1) \bar{u}(p_1, s_1) \gamma^\mu v(p_2, s_2) \\ & + i\sqrt{2}G_F M_Z^2 \rho \chi_0(s) \bar{v}(k_2) \gamma_\mu (g_V^e - g_A^e \gamma_5) u(k_1) \bar{u}(p_1, s_1) \gamma^\mu (g_V^\tau - g_A^\tau \gamma_5) v(p_2, s_2), \end{aligned} \quad (2.41)$$

where $\alpha = \alpha(M_Z)$ is the running fine-structure constant, q_e and q_τ are the electric charges of the electron and τ lepton in units of e , g_V and g_A are the weak neutral couplings of the electron and τ lepton, $M_Z(\Gamma_Z)$ is the physical mass (width) of the Z^0 , G_F is the Fermi constant, ρ is a phenomenological constant describing the relative strength of weak neutral current compare to the weak charged current (see (2.38)), $\chi_0(s)$ is the Z -boson propagator, which in the lowest Breit-Wigner approximation has the following form:

$$\chi_0(s) = \frac{1}{s - M_Z^2 + i s \Gamma_Z / M_Z}, \quad (2.42)$$

and $s = (k_1 + k_2)^2$.

Using the amplitude (2.41) and averaging over the helicity states of the incoming electron and positron, the differential cross section is obtained for the τ pair production with polarization vectors s_1 and s_2 ². In the center of mass system of the incoming e^- and e^+ and choosing the z -axis along the τ^- direction and the e^- momentum lying in the $(x - z)$ plane, such as

$$k_1^\mu = (k, k \sin \theta, 0, k \cos \theta) \quad k_2^\mu = (k, -k \sin \theta, 0, -k \cos \theta) \quad (2.43)$$

² s^μ is a covariant polarization vector, satisfying $sp = 0$, $s^2 = -1$. If s^* is a unit vector in the direction of particle polarization in its rest frame, then

$$s^0 = \frac{ps^*}{m}; \quad s = s^* + \frac{p(ps^*)}{m(m+E)}.$$

	γ	γZ	Z
$F_0(s)$	$q_e^2 q_\tau^2$	$2q_e q_\tau g_V^e g_V^\tau \text{Re} P_0(s)$	$(g_V^e{}^2 + g_A^e{}^2)(g_V^\tau{}^2 + g_A^\tau{}^2) P_0(s) ^2$
$F_1(s)$		$2q_e q_\tau g_A^e g_A^\tau \text{Re} P_0(s)$	$4g_V^e g_A^e g_V^\tau g_A^\tau P_0(s) ^2$
$F_2(s)$	$-q_e^2 q_\tau^2$	$-2q_e q_\tau g_V^e g_V^\tau \text{Re} P_0(s)$	$(g_V^e{}^2 + g_A^e{}^2)(g_A^\tau{}^2 - g_V^\tau{}^2) P_0(s) ^2$
$G_0(s)$		$2q_e q_\tau g_V^e g_A^\tau \text{Re} P_0(s)$	$2(g_V^e{}^2 + g_A^e{}^2) g_V^\tau g_A^\tau P_0(s) ^2$
$G_1(s)$		$2q_e q_\tau g_A^e g_V^\tau \text{Re} P_0(s)$	$2g_V^e g_A^e (g_V^\tau{}^2 + g_A^\tau{}^2) P_0(s) ^2$
$G_2(s)$		$2q_e q_\tau g_V^e g_A^\tau \text{Im} P_0(s)$	$-2(g_V^e{}^2 + g_A^e{}^2) g_V^\tau g_A^\tau P_0(s) ^2$

Table 2.2: Contributions from γ -, Z^0 -exchange and their interference to the form-factors in the differential cross section.

$$p_1^\mu = (E, 0, 0, p) \quad p_2^\mu = (E, 0, 0, -p) \quad (2.44)$$

and

$$s_1 = (\beta\gamma s_{1z}^*, s_{1x}^*, s_{1y}^*, \gamma s_{1z}^*) \quad s_2 = (-\beta\gamma s_{2z}^*, s_{2x}^*, s_{2y}^*, \gamma s_{2z}^*), \quad (2.45)$$

the differential cross section reads:

$$\begin{aligned} \frac{d\sigma}{d\Omega}(s_1^*, s_2^*) &= \frac{\alpha^2}{8s} \{ (1 + s_{1z}^* s_{2z}^*) [F_0(s)(1 + \cos^2 \theta) + F_1(s)2 \cos \theta] \\ &\quad - (s_{1z}^* + s_{2z}^*) [G_0(s)(1 + \cos^2 \theta) + G_1(s)2 \cos \theta] \\ &\quad + [(s_{1y}^* s_{2y}^* - s_{1x}^* s_{2x}^*) F_2(s) + (s_{1y}^* s_{2x}^* + s_{1x}^* s_{2y}^*) G_2(s)] \sin^2 \theta \}, \end{aligned} \quad (2.46)$$

where s_1^* (s_2^*) designates a unit vector in the direction of the τ^- (τ^+) polarization in its own rest frame and θ is the angle between the momenta of the e^- and the τ^- [21, 22]. The functions F_0, F_1, F_2 are associated with parity conserving terms, whereas G_0, G_1, G_2 correspond to parity violating observables. They are given in Table 2.2, where

$$P_0(s) = \frac{s \chi_0(s)}{4 \sin^2 \theta_W \cos^2 \theta_W}. \quad (2.47)$$

Only the terms proportional to $(1 + \cos^2 \theta)$ in (2.46) contribute to the total cross-section:

$$\sigma_{total} = \frac{4\pi\alpha^2}{3s} F_0(s). \quad (2.48)$$

Therefore, $F_0(s)$ represents the normalization of production cross-section with respect to the point QED cross-section. On the Z^0 peak the pure Z^0 -exchange dominates, but the contribution from the γZ^0 interference vanishes.

From the main result (2.46) the different asymmetries and polarization variables are identified. The linear dependence on $\cos \theta$ in the cross-section leads to a forward-

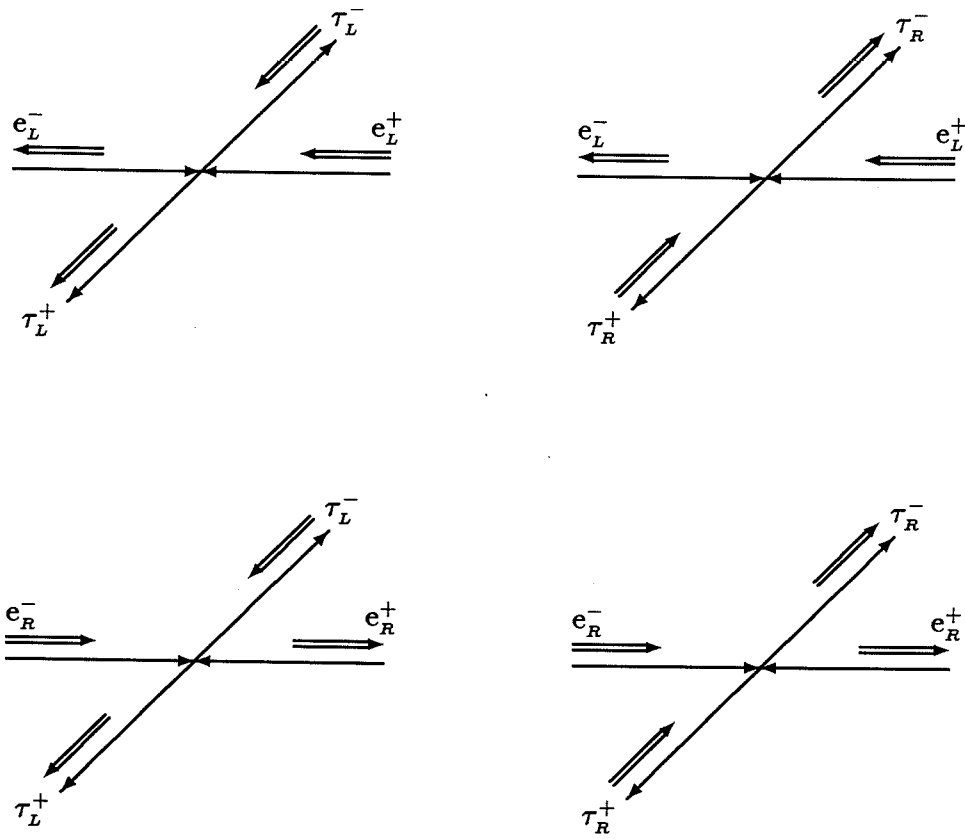


Figure 2.7: Helicity configurations of the initial and final state fermions in the process $e^+e^- \rightarrow \tau^+\tau^-$, allowed by helicity conservation in the relativistic limit.

backward asymmetry when the final polarization of the τ lepton is not measured

$$A_{FB} = \frac{\sigma(\cos \theta > 0) - \sigma(\cos \theta < 0)}{\sigma_{total}} = \frac{3 F_1(s)}{4 F_0(s)} = 3 \frac{g_V^e g_A^e}{g_V^{e^2} + g_A^{e^2}} \frac{g_V^\tau g_A^\tau}{g_V^{\tau^2} + g_A^{\tau^2}}. \quad (2.49)$$

From (2.46) the effect of the longitudinal spin correlations of the produced τ leptons is observed. The correlation is such that if $s_{1z}^* = \pm 1$, then the cross-section is maximum when $s_{2z}^* = \pm 1$, i.e. the helicities of τ^+ and τ^- prefer to be opposite to each other (Figure fig:fig/helacorr) [27]. Integrating over transverse components of the spin and considering only its longitudinal part, the longitudinal polarization asymmetry of the τ lepton is defined by the following expression

$$\begin{aligned} P_\tau(\cos \theta) &= \frac{\sigma(h_{\tau^-} = +1) - \sigma(h_{\tau^-} = -1)}{\sigma_{total}} \\ &= \frac{G_0(s)(1 + \cos^2 \theta) + G_1(s)2 \cos \theta}{F_0(s)(1 + \cos^2 \theta) + F_1(s)2 \cos \theta} = \frac{P_\tau + P_Z \frac{2 \cos \theta}{1 + \cos^2 \theta}}{1 + P_\tau P_Z \frac{2 \cos \theta}{1 + \cos^2 \theta}}, \end{aligned} \quad (2.50)$$

where $h_{\tau^-} \equiv s_{1z}^*$ is the helicity of the τ^- . The $P_\tau(\cos \theta)$ averaged over the all τ production angles is given by $G_0(s)/F_0(s)$ and on the Z^0 -peak could be expressed through the τ lepton electroweak couplings only

$$P_\tau = -\frac{G_0(s)}{F_0(s)} = -\frac{2g_V^\tau g_A^\tau}{g_V^{\tau^2} + g_A^{\tau^2}}. \quad (2.51)$$

The dependence of the τ lepton polarization on the production angle gives a possibility to measure a polarization forward-backward asymmetry A_{FB}^P , which on the Z^0 -peak is given by the electroweak couplings of electron

$$A_{FB}^P = \frac{3}{4} P_Z = -\frac{3 G_1(s)}{4 F_0(s)} = -\frac{3}{2} \frac{g_V^e g_A^e}{g_V^{e^2} + g_A^{e^2}}. \quad (2.52)$$

The transverse spin correlations observed in (2.46) are of two types: between transverse-transverse within the production plane and transverse-normal to the production plane components of the polarization. A detailed analysis of this transverse spin correlations has been performed in [23], where it was shown that they lead to azimuthal correlations of τ decay products.

2.5 Input parameters and radiative corrections

The Born level calculations of physical observables are, in most cases, a good approximation to experimentally measured values. Nevertheless, confronting Standard Electroweak Model predictions with more and more precise experimental data requires the best possible measurements of its input parameters as well as an adequate knowledge of the radiative corrections to the studied processes.

Parameter	Measurement	Value	Uncertainty (ppm)
α	$(g-2)_e$ [24]	$1/137.035\,989\,5(61)$	0.045
G_F	muon lifetime τ_μ [24]	$1.166\,39(2) \times 10^{-5} \text{ GeV}^{-2}$	17
M_Z	lineshape (LEP) [25]	$91.1888(44) \text{ GeV}$	48

Table 2.3: Experimental values of the most accurately measured input parameters of the Standard Electroweak Model. The relative uncertainty is given in parts per million (ppm).

There are three independent very accurately measured parameters that play an important role as inputs to the Standard Electroweak Model: the fine-structure constant α , the muon decay constant G_μ , which may be regarded as the modern definition of the Fermi constant, and the Z^0 mass. Their experimental values together with the relative uncertainty are given in Table 2.3. As it is seen from (2.39), they together describe the gauge sector of the Standard Electroweak Model.

Due to the fact, that the Standard Electroweak Model is a renormalizable quantum field theory, radiative corrections to any physical processes are finite and calculable within that theory. In the neutral current processes, electroweak corrections could be separated into two categories: QED (pure photonic) corrections and genuine electroweak (non-photonic) corrections [28]. This separation is possible since QED corrections form a gauge invariant subgroup. Moreover, QED corrections depend on the details of the experimental apparatus, whereas such dependence of electroweak corrections is negligible.

At the Z^0 peak the dominant contribution to QED corrections arises from the diagrams where a photon is radiated off the initial state fermion (Figure 2.8, left). QED corrections due to the initial-state radiation are treated by convoluting the differential Born cross-section (2.46), $\sigma_0(s)$, with the so-called radiator function $R(z, s)$ [29]:

$$\sigma(s) = \int_{4m_f^2/s}^1 dz \sigma_0(zs) R(z, s), \quad (2.53)$$

where m_f is a mass of the produced fermion. This initial-state radiation modifies the effective center-of-mass energy and has a drastic effect on the Z^0 lineshape: decrease of the peak position by $\simeq 110 \text{ MeV}$, increase of the width by $\simeq 400 \text{ MeV}$ and reduction of the peak cross-section by about 25%. Nevertheless, these large effects are calculated with a precision of 0.1 % [29]. Final-state radiation (Figure 2.8, right) exhibits a much smaller effects. The correction arising from the interference between initial- and final-state radiation is suppressed for \sqrt{s} close to M_Z .

Electroweak (non-photonic) corrections come through propagator corrections, vertex corrections and box diagrams (Figure 2.9). They are absorbed in the lowest-order

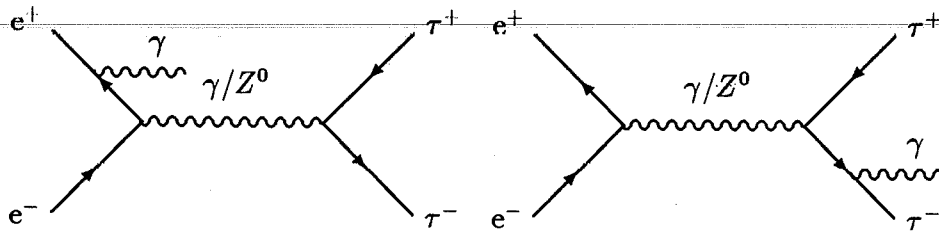


Figure 2.8: Pure QED radiative corrections to the process $e^+e^- \rightarrow \tau^+\tau^-$ due to the initial-state and final-state radiation.

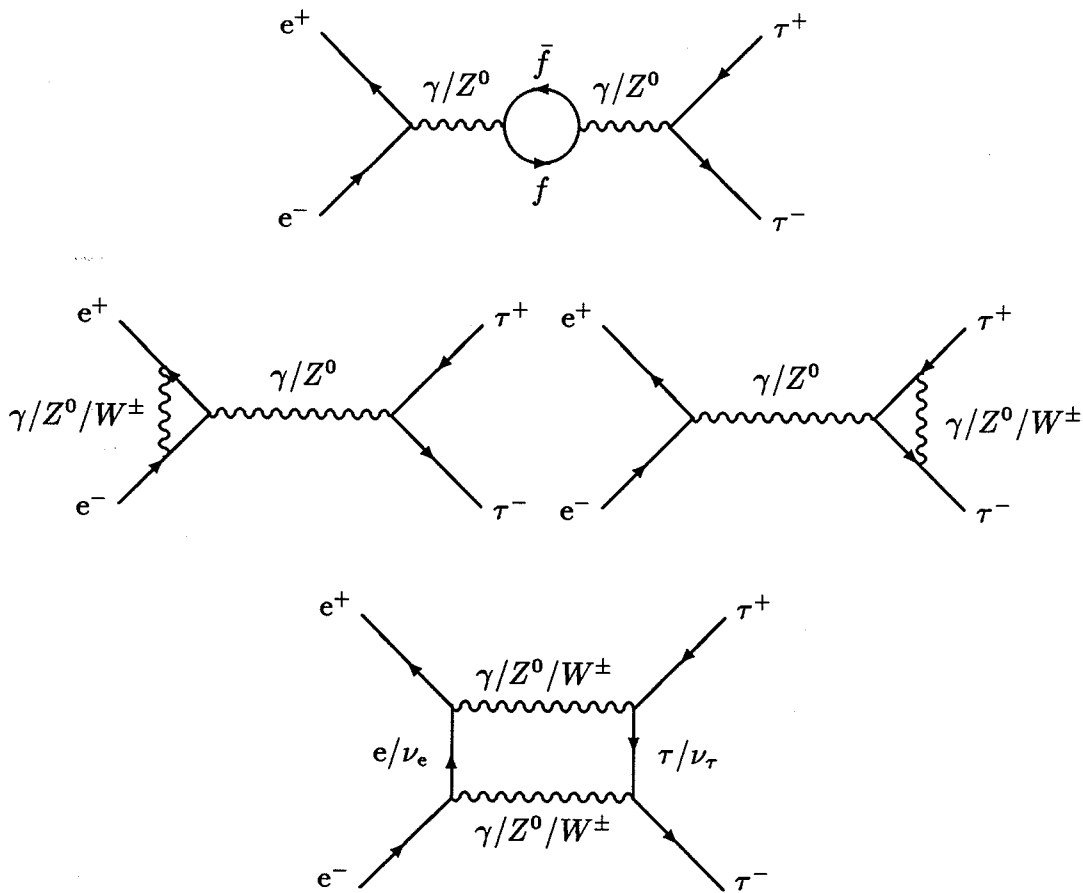


Figure 2.9: High-order electroweak corrections to the process $e^+e^- \rightarrow \tau^+\tau^-$ due to the propagator corrections, vertex corrections and box diagrams.

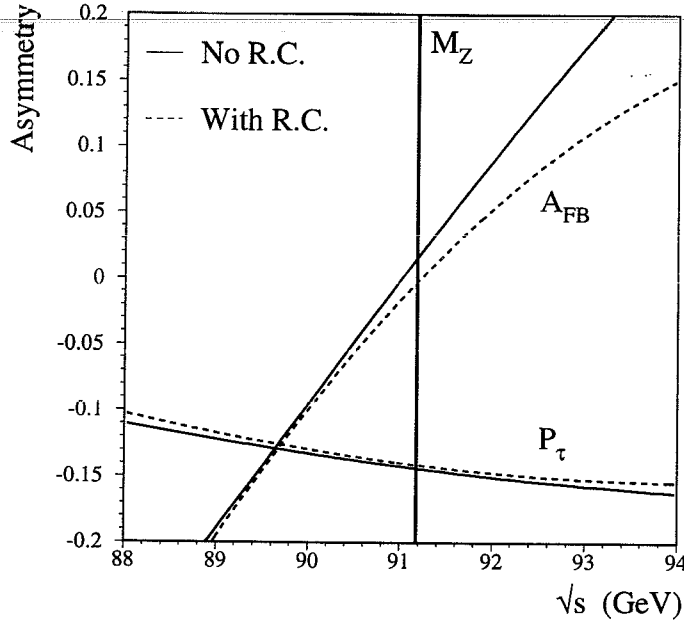


Figure 2.10: The effect of radiative corrections (R.C.) on A_{FB} and P_τ for leptons. The curves are calculated using analytical calculations from the ZFITTER program [26].

Born formulae by modifications, which can be summarized as following:

1. modifying α by an s -dependent photon vacuum polarization correction $\Delta\alpha(s)$:

$$\alpha(s) = \frac{\alpha(0)}{1 - \Delta\alpha(s)}; \quad (2.54)$$

2. the Z^0 -boson width entering in the Z^0 propagator becomes s -dependent:

$$\Gamma_Z(s) = \frac{s}{m_Z^2} \Gamma_Z; \quad (2.55)$$

3. introducing an s -dependent *effective* vector and axial-vector coupling constants of the weak neutral current:

$$g_V^f(s) = \sqrt{\rho_f(s)} (T_{3,f} - 2\kappa_f(s)Q_f \sin^2 \theta_W) \quad (2.56)$$

$$g_A^f(s) = \sqrt{\rho_f(s)} T_{3,f}, \quad (2.57)$$

where $\sin^2 \theta_W \equiv 1 - M_W^2/M_Z^2$, $\rho_f(s)$ and $\kappa_f(s)$ are fermion flavor dependent form-factors.

These modifications form the so-called *improved Born approximation*.

The effect of the radiative corrections on the forward-backward asymmetry and on the polarization asymmetry of the τ lepton is illustrated in Figure 2.10, where it is seen that P_τ is much less affected by the radiative corrections compare to A_{FB} .

Radiative corrections play a crucial role in the evaluation of M_W and $\sin^2 \theta_W$ through (2.38) and (2.39). In particular, (2.39) becomes:

$$\sin^2 \theta_W \cos^2 \theta_W = \frac{\pi \alpha}{\sqrt{2} G_F M_Z^2 (1 - \Delta r)}, \quad (2.58)$$

where Δr includes the radiative corrections [28]. For $M_t^2/M_Z^2 \gg 1$ and $M_H^2/M_Z^2 \gg 1$, in the leading approximation $\Delta r \sim -M_t^2/M_Z^2$ and $\Delta r \sim \ln(M_H^2/M_Z^2)$, therefore, constraints on the top mass M_t and the Higgs boson mass M_H are inferred from precision electroweak measurements and a detailed knowledge of the radiative corrections.

Chapter 3

Tau Lepton

3.1 Discovery and brief history

The possibility of a third, sequential lepton l^\pm , heavier than the muon, was investigated in detail by Y. S. Tsai in 1971 [27]. He predicted the correlations between the decay products of l^+ and l^- produced in the colliding-beam e^+e^- experiment, and calculated the decay widths of l^\pm into the major anticipated decay modes, dependent on the hypothetical lepton's mass. The first experimental confirmation of its existence took place in 1975 using the Mark I detector at the SPEAR storage ring at SLAC (Stanford Linear Accelerator Center). M. L. Perl *et al.* [30] observed 64 “anomalous events” (they detected a total of 86 $e^\pm\mu^\mp$ events with a calculated background of 22 events) of the type

$$e^+e^- \rightarrow e^\pm\mu^\mp + \text{missing energy},$$

which were interpreted as the production and subsequent decay of a heavy, sequential lepton [31]. Analysis of data from the PLUTO experiment at the DORIS e^+e^- storage ring at DESY (Deutsches Elektronen-Synchrotron) confirmed this hypothesis [32] and the name of the new lepton, τ from the Greek $\tau\rho\iota\tau\omicron\nu$ (third), was proposed in August 1977 [33]. As it is known now, it was the discovery of the first fermion from the third generation.

Most of our knowledge of the τ -lepton came from studies of its production and decay at e^+e^- colliders, which offer a “clean” experimental environment for this. Many of the properties of the τ -lepton were established near the production threshold in the few years after its discovery. Its mass, spin, electromagnetic current coupling, leptonic and major semi-hadronic decay modes were all measured by 1978 by several experiments, running on the SPEAR and DORIS colliders at $\sqrt{s} = 4$ GeV. The τ lifetime measurement required the higher center-of-mass energies of PETRA ($\sqrt{s} = 30 - 46$ GeV) and PEP ($\sqrt{s} = 29$ GeV) and was performed only in 1982 [34]. New generation of experiments at CESR and DORIS II ($\sqrt{s} = 10$ GeV), and at TRISTAN

($\sqrt{s} = 56 - 60$ GeV) yielded a wealth of new information and refined the previous results [35].

The basic properties of the τ lepton and its neutrino are now being measured with improved precision at the BEPC collider, at CESR, at LEP and at SLC.

3.2 Main properties of τ lepton and ν_τ

A precise measurement of the τ lepton mass has been performed by the BES Collaboration at the BEPC collider [36]. A data driven scan of the energy threshold for τ pair production in e^+e^- collisions resulted in the value of m_τ :

$$m_\tau = 1776.96^{+0.18+0.25}_{-0.21-0.17} \text{ MeV.}$$

Due to the so large mass, τ lepton has a very short lifetime ($\tau_\tau \propto G_F^{-2} m_\tau^{-5}$) and decays into the variety of the final states. In particular, τ lepton is the only presently known lepton which is massive enough to decay into hadrons. The present world average value of the τ lifetime is [37]:

$$\tau_\tau = 291.6 \pm 1.6 \text{ fs.}$$

At LEP this value corresponds to the τ 's mean travel distance of $\langle l_\tau \rangle = \beta_\tau \gamma_\tau \tau_\tau \simeq 2.3$ mm. The present world average values of the branching ratios for the major, exclusive and inclusive, τ decay modes are summarized below [37, 38], where h^\pm stands for π^\pm or K^\pm :

Decay Mode	BR (%)
$e^- \bar{\nu}_e \nu_\tau$	17.79 ± 0.09
$\mu^- \bar{\nu}_\mu \nu_\tau$	17.33 ± 0.09
$\pi^- \nu_\tau$	11.09 ± 0.15
$\pi^- \pi^0 \nu_\tau$	24.91 ± 0.21
$\pi^- 2\pi^0 \nu_\tau$	9.09 ± 0.14
$h^- 3\pi^0 \nu_\tau$	1.15 ± 0.15
$h^- 4\pi^0 \nu_\tau$	0.16 ± 0.07
$h^- \bar{K}^0 \nu_\tau$	1.03 ± 0.09
$h^- \pi^0 \bar{K}^0 \nu_\tau$	0.53 ± 0.06
$K^- \nu_\tau$	0.68 ± 0.04
$K^* \nu_\tau$	1.36 ± 0.08
particle $^- \geq 0$ neutrals ν_τ	85.41 ± 0.23
$2h^- h^+ \geq 0$ neutrals ν_τ	14.49 ± 0.23
$3h^- 2h^+ \geq 0$ neutrals ν_τ	0.10 ± 0.01

An upper limit for the τ neutrino mass

$$m_{\nu_\tau} < 23.8 \text{ MeV at 95\% CL}$$

recently has been given by the ALEPH Collaboration [39].

Results of the measurement of the Michel parameters ρ , η , ξ , $\xi\delta$ and the average τ neutrino helicity from the ARGUS experiment [122, 125, 126, 123, 124] at DORIS II and ALEPH [121] at LEP are summarized in the last chapter, where the result of this thesis's measurement is compared with them.

All experimental results obtained so far suggest that τ lepton is the third sequential charged lepton with its own conserved lepton number and associated neutrino ν_τ [40].

3.3 Lorentz structure of the τ lepton decays

3.3.1 Leptonic decays

Both leptonic decays of the τ

$$\tau^\mp \rightarrow e^\mp \nu_e \nu_\tau \quad \text{and} \quad \tau^\mp \rightarrow \mu^\mp \nu_\mu \nu_\tau$$

can be described by the most general, parity-nonconserving, local and derivative-free, lepton-number conserving Hamiltonian, representing four-fermion point interaction [41, 42]:

$$\mathcal{M} = \frac{G_F}{\sqrt{2}} \sum_{\alpha=S,P,V,A,T} \langle \bar{l} | \Gamma^\alpha | \nu_l \rangle \langle \bar{\nu}_\tau | \Gamma_\alpha (C_\alpha + C'_\alpha \gamma^5) | \tau_\mu \rangle, \quad (3.1)$$

where Γ^α ($\alpha = S, P, V, A, T$) matrices define properties of the lepton currents under Lorentz transformations:

$$\Gamma^S = 1 \quad (\text{scalar}) \quad (3.2)$$

$$\Gamma^P = \gamma^5 \quad (\text{pseudoscalar}) \quad (3.3)$$

$$\Gamma^V = \gamma^\mu \quad (\text{vector}) \quad (3.4)$$

$$\Gamma^A = \gamma^\mu \gamma^5 \quad (\text{axial-vector}) \quad (3.5)$$

$$\Gamma^T = \frac{i}{2\sqrt{2}} (\gamma^\mu \gamma^\nu - \gamma^\nu \gamma^\mu) \quad (\text{tensor}), \quad (3.6)$$

C_α and C'_α ($\alpha = S, P, V, A, T$) are ten complex coupling constants.

The Fierz transformations [46] allow various forms for this Hamiltonian. In the "helicity projection form" which is characterized by spinors of a definite handedness (or *chirality*), the matrix element is given by [47, 48]:

$$\mathcal{M} = \frac{4G_F}{\sqrt{2}} \sum_{\substack{\alpha=S,V,T \\ \epsilon, \mu=R,L}} g_{\epsilon\mu}^\alpha \langle \bar{l}_\epsilon | \Gamma^\alpha | (\nu_l)_\epsilon \rangle \langle (\bar{\nu}_\tau)_m | \Gamma_\alpha | \tau_\mu \rangle, \quad (3.7)$$

The chiralities n and m of the ν_l and $\bar{\nu}_\tau$ are uniquely determined by given α , ϵ and μ : in the case of vector and axial-vector interactions the chirality of a neutrino is equal to the chirality of its associated charged lepton, while it is opposite in the case of scalar, pseudoscalar and tensor interactions.

From the twelve complex coupling constants, $g_{\epsilon\mu}^\alpha$, only ten are relevant, as the g_{LL}^T and g_{RR}^T couplings are excluded due to their linear dependency on the others¹. The $g_{\epsilon\mu}^\alpha$ couplings give only the relative strength of the different interactions and have a simple physical interpretation: $n_\alpha |g_{\epsilon\mu}^\alpha|^2$ is equal to the relative probability for a μ -handed τ lepton to decay into an ϵ -handed daughter lepton (electron or muon) by the interaction Γ^α , where the factors $n_S = 1/4$, $n_V = 1$ and $n_T = 3$ take care of the proper normalization. $V-A$ interaction thus corresponds to $g_{LL}^V = 1$, all other couplings being zero. Any other interaction contributing to the leptonic τ decay shows a different kind of chirality structure with at least some of the particles being right-handed.

Langacker and London in [49] have shown that, neglecting neutrino masses, explicit lepton-number nonconservation still leads to a matrix element (3.7) with a one-to-one correspondence between the coupling constants in the lepton-number-conserving case and combinations of parameters in the lepton-number-violating case.

Taking the matrix element (3.7) and integrating over the unobserved massless neutrinos, the energy spectra of the daughter lepton is obtained. In the rest-frame of the τ lepton, neglecting radiative corrections and $\mathcal{O}(\frac{m_l^2}{m_\tau^2})$ terms this reads:

$$\frac{d\Gamma(\tau^\mp \rightarrow l^\mp \bar{\nu}_l \nu_\tau)}{dx_l d\Omega_l} = \frac{G_F^2 m_\tau^5}{192\pi^4} x_l^2 \left\{ 3(1-x_l) + \rho \left(\frac{8x_l}{3} - 2 \right) + \eta \frac{m_l}{m_\tau} \frac{6(1-x_l)}{x_l} \right. \\ \left. \mp (\mathbf{s}_\tau^* \mathbf{n}_l^*) \left[\xi(1-x_l) + \xi\delta \left(\frac{8x_l}{3} - 2 \right) \right] \right\}, \quad (3.8)$$

where $x_l = E_l/E_l^{max}$ is the lepton energy divided by its maximum energy $E_l^{max} = m_\tau/2$; \mathbf{s}_τ^* is τ polarization vector, \mathbf{n}_l^* is a direction of the daughter lepton; ρ , η , ξ and $\xi\delta$ are real, bilinear combinations of the coupling constants, known as the Michel parameters [41, 42, 43, 44, 45]:

$$\rho = \frac{3}{4} \{ 1 - [|g_{LR}^V|^2 + |g_{RL}^V|^2 + 2|g_{LR}^T|^2 + 2|g_{RL}^T|^2 + \text{Re}(g_{LR}^S g_{LR}^{T*} + g_{RL}^S g_{RL}^{T*})] \} \quad (3.9)$$

$$\eta = \frac{1}{2} \text{Re}(6g_{RL}^V g_{LR}^{T*} + 6g_{LR}^V g_{RL}^{T*} + g_{RR}^S g_{LL}^{V*} + g_{RL}^S g_{LR}^{V*} + g_{LR}^S g_{RL}^{V*} + g_{LL}^S g_{RR}^{V*}) \quad (3.10)$$

$$\xi = |g_{LL}^V|^2 + 3|g_{LR}^V|^2 - 3|g_{RL}^V|^2 - |g_{RR}^V|^2 + \frac{1}{4}(|g_{LL}^S|^2 - |g_{LR}^S|^2 + |g_{RL}^S|^2 - |g_{RR}^S|^2) \\ + 5(|g_{LR}^T|^2 - |g_{RL}^T|^2) + 4\text{Re}(g_{LR}^S g_{LR}^{T*} - g_{RL}^S g_{RL}^{T*}) \quad (3.11)$$

$$\xi\delta = \frac{3}{4} \{ |g_{LL}^V|^2 - |g_{RR}^V|^2 + \frac{1}{4}(|g_{LL}^S|^2 - |g_{LR}^S|^2 + |g_{RL}^S|^2 - |g_{RR}^S|^2) \\ - |g_{LR}^T|^2 + |g_{RL}^T|^2 + \text{Re}(g_{LR}^S g_{LR}^{T*} - g_{RL}^S g_{RL}^{T*}) \}. \quad (3.12)$$

¹For the relation between $g_{\epsilon\mu}^\alpha$ and C_α , C'_α see [47, 48].

The $V-A$ structure of the charged current gives the following values for these parameters:

$$\rho = \frac{3}{4}, \quad \eta = 0, \quad \xi = 1, \quad \xi\delta = \frac{3}{4}.$$

Unfortunately, for a complete determination of the Lorentz structure of the leptonic τ decays, a measurement of only these Michel parameters is not enough. As it has been shown by W. Fetscher in [50], the Lorentz structure can be unambiguously determined by combined analysis of the following measurements:

- τ lifetime and the corresponding branching ratios;
- Michel asymmetry parameters ξ and $\xi\delta$;
- the polarization ξ' of the outgoing lepton;
- the cross-section of the inverse τ decay $\nu_\tau e^- \rightarrow \tau^- \nu_e$.

The importance of ξ and $\xi\delta$ asymmetry parameters comes from the fact that they define the fraction of right-handed τ 's contributing to the decay:

$$Q_R^\tau = \frac{1}{4}|g_{RR}^S|^2 + \frac{1}{4}|g_{LR}^S|^2 + |g_{RR}^V|^2 + |g_{LR}^V|^2 + 3|g_{LR}^T|^2 = \frac{1}{2} \left\{ 1 + \frac{1}{9}(3\xi - 16\xi\delta) \right\}. \quad (3.13)$$

Thus a measurement of Q_R^τ gives simultaneous limits to five of the ten complex couplings constants.

The so-called low-energy parameter η receives contributions from the interference between vector and scalar and vector and tensor interactions, and is thus particularly sensitive to non $V-A$ couplings. Besides that, η may give a contribution to the total decay rate of the τ lepton ². This fact makes η to be of a particular importance for establishing lepton universality. Including electroweak radiative corrections [52] and finite mass effects, the partial decay width of leptonic τ decay can be written as

$$\Gamma(\tau \rightarrow l\bar{\nu}_l\nu_\tau) = \frac{G_F^2 m_\tau^5}{192\pi^3} \left[f\left(\frac{m_l^2}{m_\tau^2}\right) + 4\eta \frac{m_l}{m_\tau} \right] \left[1 + \frac{3}{5} \frac{m_\tau^2}{m_W^2} \right] \left[1 + \frac{\alpha(m_\tau)}{2\pi} \left(\frac{25}{4} - \pi^2 \right) \right], \quad (3.14)$$

where $f\left(\frac{m_l^2}{m_\tau^2}\right)$ is a phase-space factor

$$f(x) = 1 - 8x + 8x^3 - x^4 - 12x^2 \ln x. \quad (3.15)$$

Measurement of the ρ Michel parameter is not one of the key experiments, as any combination of the six couplings $g_{LL}^S, g_{LR}^S, g_{RL}^S, g_{RR}^S, g_{RR}^V, g_{LL}^V$ with the other four couplings being zero yields the $V-A$ value $\rho = \frac{3}{4}$. But, it would be very exciting if $\rho \neq \frac{3}{4}$, indicating the presence of non $V-A$ interaction.

²Other combinations of $g_{\epsilon\mu}^\alpha$ couplings may contribute as well to the total decay rate, but their contributions are suppressed by the ν_τ mass, see [51].

It is necessary to emphasize that, in principle, both pure leptonic τ decays have to be described by their own set of Michel parameters:

$$\begin{aligned}\tau^{\mp} &\rightarrow e^{\mp} \nu_e \nu_{\tau} & \rho_e, \eta_e, \xi_e, \xi_e \delta_e \\ \tau^{\mp} &\rightarrow \mu^{\mp} \nu_{\mu} \nu_{\tau} & \rho_{\mu}, \eta_{\mu}, \xi_{\mu}, \xi_{\mu} \delta_{\mu}\end{aligned}$$

which allows to test $e-\mu$ universality of the weak charged current in the leptonic τ decays. Assuming this universality *a priori*, both leptonic decays are described by the same set of parameters $\rho_l, \eta_l, \xi_l, \xi_l \delta_l$.

3.3.2 Semileptonic decays

The general matrix element for the semileptonic decay $\tau^{\mp} \rightarrow \nu_{\tau} h^{\mp}$ is written in the form:

$$\mathcal{M} = \frac{G_F}{\sqrt{2}} \sum_{\alpha=S, P, V, A, T} f^{\alpha} \langle \bar{h} | \Gamma^{\alpha} | 0 \rangle \langle \bar{\nu}_{\tau} | \Gamma_{\alpha} | \tau \rangle, \quad (3.16)$$

In fact, knowledge of the structure of the hadronic current reduces a number of possible types of interactions Γ^{α} .

For the decay modes with the lowest multiplicity,

$$\tau \rightarrow \nu_{\tau} \pi \quad \text{and} \quad \tau \rightarrow \nu_{\tau} K,$$

the structure of the relevant hadronic currents is already known from the measured decays $\pi \rightarrow \mu \bar{\nu}_{\mu}$ and $K \rightarrow \mu \bar{\nu}_{\mu}$:

$$\langle \pi(p) | \Gamma^A | 0 \rangle = \langle \pi(p) | \gamma^{\mu} \gamma_5 | 0 \rangle = i\sqrt{2} f_{\pi} p^{\mu} \cos \theta_C \quad (3.17)$$

$$\langle K(p) | \Gamma^A | 0 \rangle = \langle K(p) | \gamma^{\mu} \gamma_5 | 0 \rangle = i\sqrt{2} f_K p^{\mu} \sin \theta_C, \quad (3.18)$$

where f_{π}, f_K are decay constants and θ_C is the Cabbibo angle.

In the Cabbibo allowed modes with $J^P = 1^-$, the matrix element of the vector charged current is obtained through an isospin rotation from the isovector part of the e^+e^- annihilation cross-section into hadrons at low energies, which measures the hadronic matrix element of the $I = 1$ component of the electromagnetic current. For the hadronic current in the $\tau \rightarrow \nu_{\tau} \rho$ decay this gives the following:

$$\langle \rho(p, \epsilon) | \Gamma^V | 0 \rangle = \langle \rho(p, \epsilon) | \gamma^{\mu} | 0 \rangle = i\sqrt{2} f_{\rho} \epsilon^{\mu} \quad (3.19)$$

where ϵ^{μ} is a polarization 4-vector of the ρ -meson, $\epsilon^{\mu} p_{\mu} = 0$.

For the exclusive τ decays into final hadronic states with $J^P = 1^+$, e.g. $\tau \rightarrow \nu_{\tau} a_1$, or Cabbibo suppressed modes with $J^P = 1^-$, e.g. $\tau \rightarrow \nu_{\tau} K^*$, the matrix element can not be predicted with the same degree of confidence.

Hence, in the case of $\tau \rightarrow \nu_\tau \pi(K)$ and $\tau \rightarrow \nu_\tau \rho$ decays, only vector and axial-vector types of interactions are considered:

$$\mathcal{M} = \frac{G_F}{\sqrt{2}} \langle \bar{h} | v_h \Gamma^V + a_h \Gamma^A | 0 \rangle \langle \bar{\nu}_\tau | v_\tau \Gamma_V + a_\tau \Gamma_A | \tau \rangle, \quad (3.20)$$

where the structure of the hadronic current $\langle \bar{h} | v_h \Gamma^V + a_h \Gamma^A | 0 \rangle$ should be specified for each particular final state and depends on the momenta of the final hadrons.

Taking \mathcal{M} for the decay $\tau \rightarrow \nu_\tau \pi$, as the simplest case, a pion distribution in the τ lepton rest frame is obtained:

$$\frac{1}{\Gamma} \frac{d\Gamma(\tau^\mp \rightarrow \pi^\mp \nu_\tau)}{d\Omega_\pi} = \frac{1}{4\pi} \left\{ 1 \mp \xi_h(\mathbf{s}_\tau^* \mathbf{n}_\pi^*) \right\} \quad (3.21)$$

where

$$\xi_h \equiv \langle h_{\nu_\tau} \rangle = \frac{2\text{Re}(v_\tau a_\tau^*)}{|v_\tau|^2 + |a_\tau|^2} \quad (3.22)$$

is known as the *hadronic chirality parameter* or the average τ *neutrino helicity*.

In the case of the $\tau \rightarrow \nu_\tau \rho$ decay, a similar distribution is obtained:

$$\frac{1}{\Gamma} \frac{d\Gamma(\tau^\mp \rightarrow \rho^\mp \nu_\tau)}{d\Omega_\rho} = \frac{1}{4\pi} \left\{ 1 \mp \alpha \xi_h(\mathbf{s}_\tau^* \mathbf{n}_\rho^*) \right\}, \quad (3.23)$$

but with reduced sensitivity to the τ polarization by the factor $\alpha = \frac{m_\tau^2 - 2m_\rho^2}{m_\tau^2 + 2m_\rho^2} \simeq 0.46$ due to the possible two helicity states of the ρ -meson: 0 or -1 . Nevertheless, the sensitivity can be regained by measuring the helicity of ρ -meson through the decay distribution of pions from the $\rho \rightarrow \pi\pi$ [53, 54, 55].

It should be noticed that each semileptonic τ decay is described, in principle, by its own chirality parameter, ξ_π for $\tau \rightarrow \nu_\tau \pi$ and ξ_ρ for $\tau \rightarrow \nu_\tau \rho$.

3.4 Correlated decay distributions

Due to the small lifetime of the τ lepton, in practice only τ decay products, except missing neutrino(s), are measured. Therefore, in order to employ the spin correlations in the τ pair, the production cross-section (2.46) must be transformed into the correlated decay distribution of their decay products.

Decay correlations were discussed for the first time in the famous paper of Y.-S. Tsai [27]. The potentialities of the correlated decay distributions as analyzers of the parameters of weak charged current processes in the τ decay have been noticed by Charles A. Nelson in [59]. They have been discussed in [50, 60] for low-energy τ -factories, where the production of τ pairs proceeds via γ exchange only. This presentation follows [21, 22], where an explicit formula for the correlated decay distributions (3.41) in terms of the average τ -polarization has been derived for the first time.

As it has seen in the previous section, the general form of the decay distribution of the polarized τ lepton could be written in the τ rest frame as [56]:

$$d\Gamma^{(s^*)}(\tau^\mp(s^*) \rightarrow \nu_\tau + A^\mp + \dots) = \Gamma(\tau \rightarrow \nu_\tau + A + \dots) \{V_0^{(A)} \mp (s_\tau^* q_A^*) V_1^{(A)}\} d^3 q_A^*, \quad (3.24)$$

where $V_0^{(A)}$ and $V_1^{(A)}$ are functions of the momentum q_A^* of the decay product A and contain a dependence on the τ decay parameters, such as the Michel parameters in leptonic τ decays or hadronic chirality parameter in semileptonic τ decays.

Consider the production and subsequent decay process:

$$e^- e^+ \rightarrow \gamma, Z \rightarrow \tau^-(s_1^*) + \tau^+(s_2^*) \rightarrow A^- + B^+ + \dots \quad (3.25)$$

A joint distribution of the final state particles A and B is obtained following a recipe formally proven in [56, 57, 58]. Thus,

$$d\sigma(e^+ e^- \rightarrow AB) = 4 d\sigma(\mathbf{n}_A^*, \mathbf{n}_B^*) \times \frac{d\Gamma_A}{\Gamma} \times \frac{d\Gamma_B}{\Gamma}, \quad (3.26)$$

where $d\sigma(\mathbf{n}_A^*, \mathbf{n}_B^*)$ is obtained from $d\sigma(\mathbf{s}_1^*, \mathbf{s}_2^*)$ in (2.46) by the substitution

$$\mathbf{s}_1^* \rightarrow \mathbf{n}_A^* = -\frac{V_1^{(A)}}{V_0^{(A)}} \mathbf{q}_A^* \quad (3.27)$$

$$\mathbf{s}_2^* \rightarrow \mathbf{n}_B^* = -\frac{V_1^{(B)}}{V_0^{(B)}} \mathbf{q}_B^*, \quad (3.28)$$

$d\Gamma_A(d\Gamma_B)$ is the differential decay rate of $\tau \rightarrow A + \dots$ ($\tau \rightarrow B + \dots$) for an unpolarized τ lepton

$$d\Gamma_A = \frac{1}{2} \sum_s d\Gamma_A^{(s)} = \Gamma(\tau \rightarrow A + \dots) V_0^{(A)} d^3 q_A^* \quad (3.29)$$

and Γ denotes the total τ decay rate.

Using these results and (2.46), the cross-section for the combined production and decay process is (3.25):

$$\begin{aligned} \frac{d^8 \sigma}{d\Omega_\tau d^3 q_A^* d^3 q_B^*} &= K(s) \{ [V_0^{(A)} V_0^{(B)} + V_1^{(A)} V_1^{(B)} q_A^* q_B^* \cos \theta_A^* \cos \theta_B^*] \\ &\quad \times [F_0(s)(1 + \cos^2 \theta) + F_1(s)2 \cos \theta] \\ &\quad + [V_1^{(A)} V_0^{(B)} q_A^* \cos \theta_A^* + V_0^{(A)} V_1^{(B)} q_B^* \cos \theta_B^*] \\ &\quad \times [G_0(s)(1 + \cos^2 \theta) + G_1(s)2 \cos \theta] \\ &\quad + V_1^{(A)} V_1^{(B)} q_A^* q_B^* \sin \theta_A^* \sin \theta_B^* \sin^2 \theta \\ &\quad \times [F_2(s) \cos(\phi_2^* - \phi_1^*) + G_2(s) \sin(\phi_2^* - \phi_1^*)] \}, \quad (3.30) \end{aligned}$$

with

$$K(s) = \frac{1}{2s} Br(\tau \rightarrow A) Br(\tau \rightarrow B). \quad (3.31)$$

This cross-section depends on the τ lepton direction in the laboratory, as well as on the momenta \mathbf{q}_A^* and \mathbf{q}_B^* of the decay products A and B in the respective τ rest frames. Without a sufficiently precise reconstruction of the τ direction, one cannot measure these variables experimentally. Instead, the cross section in terms of the laboratory frame variables, independent of the τ direction, is derived.

A momentum of the τ decay products \mathbf{q}_i^* ($i = A, B$) is boosted to the laboratory frame along the direction of their parent τ leptons. So, the variables in the two systems are related by

$$\begin{aligned} E_i^* &= \gamma(E_i - \beta q_i \cos \theta_i) \\ q_i^* \cos \theta_i^* &= \gamma(q_i \cos \theta_i - \beta E_i) \\ q_i^* \sin \theta_i^* &= q_i \sin \theta_i \\ \phi_i^* &= \phi_i, \end{aligned} \quad (3.32)$$

where $\gamma = \sqrt{s}/2m_\tau$ is the Lorentz factor of the τ and $\beta = \sqrt{1 - \gamma^{-2}}$, with a jacobian of this transformation being

$$\frac{\partial(q_i^*, \cos \theta_i^*)}{\partial(q_i, \cos \theta_i)} = \frac{E_i^*}{q_i^{*2}} \frac{q_i^2}{E_i}. \quad (3.33)$$

The range of the angular variables depends on the decay channel. For semileptonic decays, two-body kinematics implies that the energy and the angle are not independent variables

$$\cos \theta_i = \cos \zeta_i \equiv \frac{\gamma E_i - E_i^*}{\beta \gamma q_i} \quad (3.34)$$

where E_i^* is the particle energy in the τ rest frame

$$E_i^* = \frac{m_\tau^2 + m_i^2}{2m_\tau}, \quad (3.35)$$

and, as in the case of leptonic decays, three body kinematics gives $0 \leq \theta_i \leq \zeta_i$.

However, the variables $\theta_A, \phi_A; \theta_B, \phi_B$, which refer to the A and B directions with respect to the their parent τ^\mp , are not directly observable. The measurable quantities are instead the opening angle θ_{AB} between A and B , sometimes defined as the acollinearity $\epsilon = \pi - \theta_{AB}$, and the orientation of the $(\mathbf{q}_A, \mathbf{q}_B)$ plane with respect to the electron beam. The acollinearity angle ϵ is related to the azimuthal angle $\phi = \phi_A + \phi_B$ between the $(\tau^- A^-)$ and $(\tau^+ B^+)$ momentum planes in the laboratory frame

$$\cos \epsilon = \cos \theta_A \cos \theta_B - \sin \theta_A \sin \theta_B \cos \phi \quad (3.36)$$

with a jacobian

$$\frac{\partial \phi}{\partial \cos \epsilon} = \frac{1}{Q}, \quad (3.37)$$

where

$$Q = \sqrt{\sin^2 \theta_A \sin^2 \theta_B - (\cos \theta_A \cos \theta_B - \cos \epsilon)^2}. \quad (3.38)$$

The transverse and normal spin correlations appear in (3.30) associated with the azimuthal variable $\phi' = \phi_A - \phi_B$, related to the orientation of the $(\mathbf{q}_A, \mathbf{q}_B)$ momentum plane. These correlations then give rise to aplanarity observables, considered in [23]. Here, ϕ' is considered as irrelevant and integrated out.

Substituting new variables and integrating over the unmeasured ones, the following expression for the cross-section is obtained from (3.30):

$$\frac{d^5 \sigma}{d\Omega_\tau d q_A d q_B d \cos \epsilon} = 2 \int \left(\frac{q_A^{*2} q_B^{*2} d^3 \sigma}{d\Omega_\tau d^3 q_A d^3 q_B} \right) d \cos \theta_A d \cos \theta_B d \phi' \left| \frac{\partial(q_A^*, \cos \theta_A^*)}{\partial(q_A, \cos \theta_A)} \right| \left| \frac{\partial(q_B^*, \cos \theta_B^*)}{\partial(q_B, \cos \theta_B)} \right| \left| \frac{\partial \phi}{\partial \cos \epsilon} \right|. \quad (3.39)$$

To express the cross-section in terms of the energies of the final particles, the following equality

$$q_i dq_i = E_i dE_i$$

is used as well.

Finally, using the explicit form of (3.30), the cross-section as a function of physical observables measured in the laboratory frame is obtained

$$\begin{aligned} \frac{d^5 \sigma}{d\Omega_\tau dE_A dE_B d \cos \epsilon} &= 4\pi K(s) q_A q_B \int \frac{E_A^* E_B^*}{Q} d \cos \theta_A d \cos \theta_B \\ &\quad \left\{ [V_0^{(A)} V_0^{(B)} + V_1^{(A)} V_1^{(B)}] q_A^* \cos \theta_A^* q_B^* \cos \theta_B^* \right\} \\ &\quad \times [F_0(s)(1 + \cos^2 \theta) + F_1(s)2 \cos \theta] \\ &\quad + [V_1^{(A)} V_0^{(B)} q_A^* \cos \theta_A^* + V_0^{(A)} V_1^{(B)} q_B^* \cos \theta_B^*] \\ &\quad \times [G_0(s)(1 + \cos^2 \theta) + G_1(s)2 \cos \theta] \}, \quad (3.40) \end{aligned}$$

where E_i^* and $q_i^* \cos \theta_i^*$ are given in (3.32) in terms of laboratory variables $E_i, q_i, \cos \theta_i$.

Integrating (3.40) over the acollinearity ϵ and over the τ -direction and making explicit transformation of all observables to the laboratory frame, the normalized cross-section becomes

$$\begin{aligned} \frac{1}{\sigma} \frac{d^2 \sigma}{dE_A dE_B} &= H_0^{(A)}(E_A) H_0^{(B)}(E_B) + H_1^{(A)}(E_A) H_1^{(B)}(E_B) \\ &\quad - P_\tau [H_1^{(A)}(E_A) H_0^{(B)}(E_B) + H_0^{(A)}(E_A) H_1^{(B)}(E_B)], \quad (3.41) \end{aligned}$$

where $P_\tau = -G_0(s)/F_0(s)$ is the averaged τ lepton polarization and functions $H_0^{(i)}$ and $H_1^{(i)}$ ($i = A, B$) define, respectively, polarization independent and polarization dependent parts of the τ decay spectrum in the laboratory system

$$\frac{1}{\Gamma_X} \frac{d\Gamma_X}{dE} (\tau^\mp \rightarrow X^\mp + \dots) = H_0^{(X)}(E) \mp P_{\tau^\mp} H_1^{(X)}(E) \quad (3.42)$$

with their explicit form depending on the particular τ decay channel. The correlated decay distribution in the form (3.41) reveals its obvious feature: being integrated over one τ decay, it reproduces the τ decay spectra on the other side of the event. Around the Z^0 resonance, it has been found that the s -dependence of the energy-energy correlations (3.41) is quite smooth [21].

In the next chapter it will be considered how to employ (3.41) for a measurement of the Michel parameters and the hadronic chirality parameter from the correlated spectra of the τ pair decay products.

Chapter 4

Analysis Method

As it has been shown in Chapter 2, the assumption of only vector (g_V) and axial-vector (g_A^f) couplings in the fermion pair production vertex $Z\bar{f}f$ result in helicity conservation. In the approximation of massless fermions, a fermion with negative helicity will always be created in a pair with an anti-fermion with positive helicity, and vice versa. When the produced fermions have finite mass, this helicity anti-correlation is not complete, but favored, as other possible spin states are suppressed by the terms $\sim \gamma^{-2} = (\frac{4m_f}{\sqrt{s}})^2$. Due to this, the τ leptons produced in the Z^0 decays have opposite helicities with negligible corrections of order 10^{-3} . At the same time, parity violation in the Z^0 production and decay leads to a net polarization of the produced fermions:

$$P_f = \frac{\sigma_R - \sigma_L}{\sigma_R + \sigma_L} \quad (4.1)$$

where σ_R and σ_L are the cross-sections for the production of right-handed and left-handed fermions. These two facts allow us to consider decay distributions of τ^- and τ^+ in their general form:

$$\frac{1}{\Gamma} \frac{d\Gamma_{\tau\mp}}{d\alpha} = H_0(\alpha) \mp P_{\tau\mp} H_1(\alpha) \quad (4.2)$$

and, since $P_\tau \equiv P_{\tau^-} = -P_{\tau^+}$,

$$\frac{1}{\Gamma} \frac{d\Gamma_{\tau\mp}}{d\alpha} = H_0(\alpha) - P_\tau H_1(\alpha), \quad (4.3)$$

where α is a set of observables sensitive to the τ decay parameters ¹.

Experimentally measurable quantities in the process

$$e^-e^+ \rightarrow \gamma, Z \rightarrow \tau^-\tau^+ \rightarrow A^-B^+ + \dots \quad (4.4)$$

are the momenta of the τ pair decay products, i.e. charged leptons and hadrons. The information on the τ leptons itself is indirect, in particular. Since both τ 's are produced

¹By τ decay parameters here, Michel parameters $\rho, \eta, \xi, \xi\delta$ for the leptonic decays, and hadronic chirality parameter ξ_h for the semileptonic decays are assumed.

in a pair, their energies are determined by energy and momentum conservation, but their directions are hard to measure due to the short τ life time. Thus, all the variables sensitive to the τ decay parameters should be defined in the laboratory frame. In the following sections these variables for each τ decay mode exploited in the analysis are described. Effects of the radiative corrections on their distributions will be accounted for in their construction.

Anti-correlation of the τ helicities in the process (4.4) leads to the correlated distribution of the τ pair decay products

$$\begin{aligned} \frac{1}{\sigma} \frac{d^2\sigma}{d\alpha d\beta} &= H_0^{(A)}(\alpha) H_0^{(B)}(\beta) + H_1^{(A)}(\alpha) H_1^{(B)}(\beta) \\ &- P_\tau \left[H_1^{(A)}(\alpha) H_0^{(B)}(\beta) + H_0^{(A)}(\alpha) H_1^{(B)}(\beta) \right], \end{aligned} \quad (4.5)$$

Given a non-zero P_τ and studying correlated distributions of the decay products in such topologies as lepton-lepton, lepton-hadron and hadron-hadron, makes it possible to access all τ decay parameters in one measurement. The method of obtaining these parameters simultaneously with P_τ from the global fit to the correlated decay spectra (4.5) and single decay distributions (4.3) will be presented in the last section.

4.1 Decay Distributions

4.1.1 Leptonic decays

In the leptonic decay modes the decay angle between the τ polarization and the momentum of the final charged lepton in the τ rest frame cannot be reconstructed since there are two missing neutrinos. Only the energy distribution of electrons and muons are measured. The transformation from the τ rest frame to the laboratory is the Lorentz boost along the τ momentum and, neglecting lepton mass,

$$E_l = \gamma_\tau (E_l^* + \beta_\tau p_l^* \cos \theta^*) \simeq \frac{E_{\text{beam}}}{m_\tau} E_l^* (1 + \cos \theta^*). \quad (4.6)$$

Thus, the measurable lepton energy $x = E_l/E_l^{\text{max}} = E_l/E_{\text{beam}}$ in the laboratory frame is related to the τ rest frame parameter $x^* = E_l^*/E_l^{*\text{max}} = 2E_l^*/m_\tau$ by $2x = x^*(1 + \cos \theta^*)$. The laboratory decay distribution is obtained from (3.8) by

$$\frac{1}{\Gamma} \frac{d\Gamma}{dx} = \int_x^1 2x^* \left\{ V_0(x^*, \rho, \eta) - P_\tau \frac{2x - x^*}{x^*} V_1(x^*, \xi, \xi\delta) \right\} dx^*, \quad (4.7)$$

where, V_0 and V_1 are functions linear to the Michel parameters [61]. This feature allows us to write the laboratory decay distribution as

$$\begin{aligned} \frac{1}{\Gamma} \frac{d\Gamma}{dx} &= H_0(x) - P_\tau H_1(x) \\ &= h_0(x) + \eta h_\eta(x) + \rho h_\rho(x) - P_\tau [\xi h_\xi(x) + \xi\delta h_{\xi\delta}(x)], \end{aligned} \quad (4.8)$$

where the functions $h_0(x)$, $h_\eta(x)$, $h_\rho(x)$, $h_\xi(x)$ and $h_{\xi\delta}(x)$ incorporate all kinematical effects, including radiative corrections. Their integrals over the spectrum of the final leptons have the following values:

$$\int h_0(x)dx = 1 \quad (4.9)$$

$$\int h_\eta(x)dx = 4\frac{m_l}{m_\tau} \quad (4.10)$$

$$\int h_\rho(x)dx = \int h_\xi(x)dx = \int h_{\xi\delta}(x)dx = 0. \quad (4.11)$$

In order to take into account all these effects, the representation of these h -functions is obtained, using a Monte Carlo technique.

The Monte Carlo program KORALZ 3.8 [62] generates the process

$$e^+e^- \rightarrow \gamma, Z^0 \rightarrow \tau^+\tau^-$$

including effects of the τ mass, longitudinal spin correlations and complete $\mathcal{O}(\alpha)$ QED corrections as well as electroweak loop corrections. The τ lepton decay itself is generated by the versatile TAUOLA library [63], which provides the final state topology including the effects of the τ polarization. There is available as well a modified TAUOLA matrix element for the leptonic τ decays [64], which allows to use different settings of the Michel parameters in the generation.

Using these generators, h -function estimators are easily obtained in the form of histograms, which provide an adequate solution for our purpose. One possible set of generated samples is shown in Table 4.1. In the case of 20 bins of lepton energy, the

Sample	ρ	η	ξ	$\xi\delta$
A (all τ)	0	0	0	0
B (all τ)	0.75	0	0	0
C (all τ)	0	1	0	0
DL (only τ_L)	0	0	1	0
DR (only τ_R)	0	0	1	0
EL (only τ_L)	0.5	0	0	0.5
ER (only τ_R)	0.5	0	0	0.5

Table 4.1: A set of generated samples used in obtaining $h_0(x)$, $h_\eta(x)$, $h_\rho(x)$, $h_\xi(x)$ and $h_{\xi\delta}(x)$ function estimators for $\tau \rightarrow e\bar{\nu}_e\nu_\tau$ and $\tau \rightarrow \mu\bar{\nu}_\mu\nu_\tau$ decays.

number of generated decays in each sample should be $\sim 10^6$ to maintain a precision of the estimation for each bin better than 1%. After histogramming of the lepton energy spectra for each generator sample and their normalization, h -function estimators are

$$\tau \rightarrow e \bar{\nu}_e \nu_\tau$$

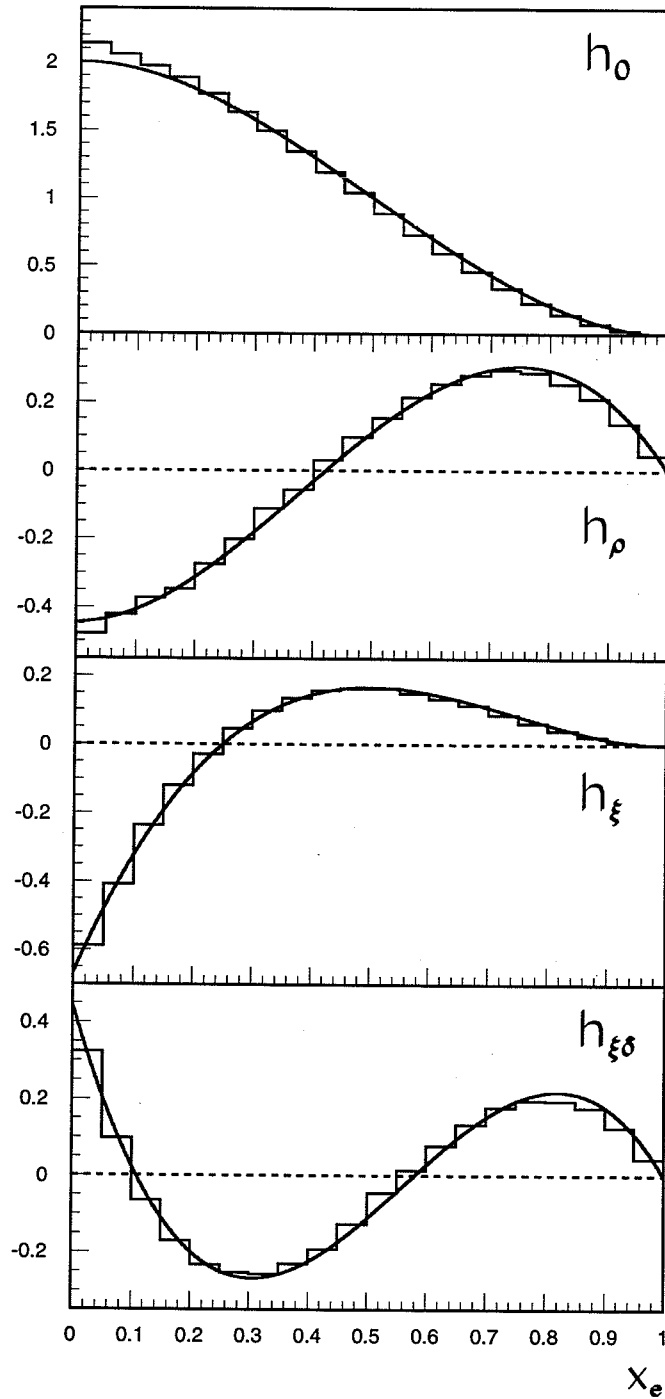


Figure 4.1: Spectral functions h_0 , h_ρ , h_ξ , $h_{\xi\delta}$ of the $\tau \rightarrow e \bar{\nu}_e \nu_\tau$ decay shown as histograms, obtained with the KORALZ generator [62] and the modified TAUOLA matrix element [64]. Superimposed solid lines represent Born level calculations.

$$\tau \rightarrow \mu \bar{\nu}_\mu \nu_\tau$$

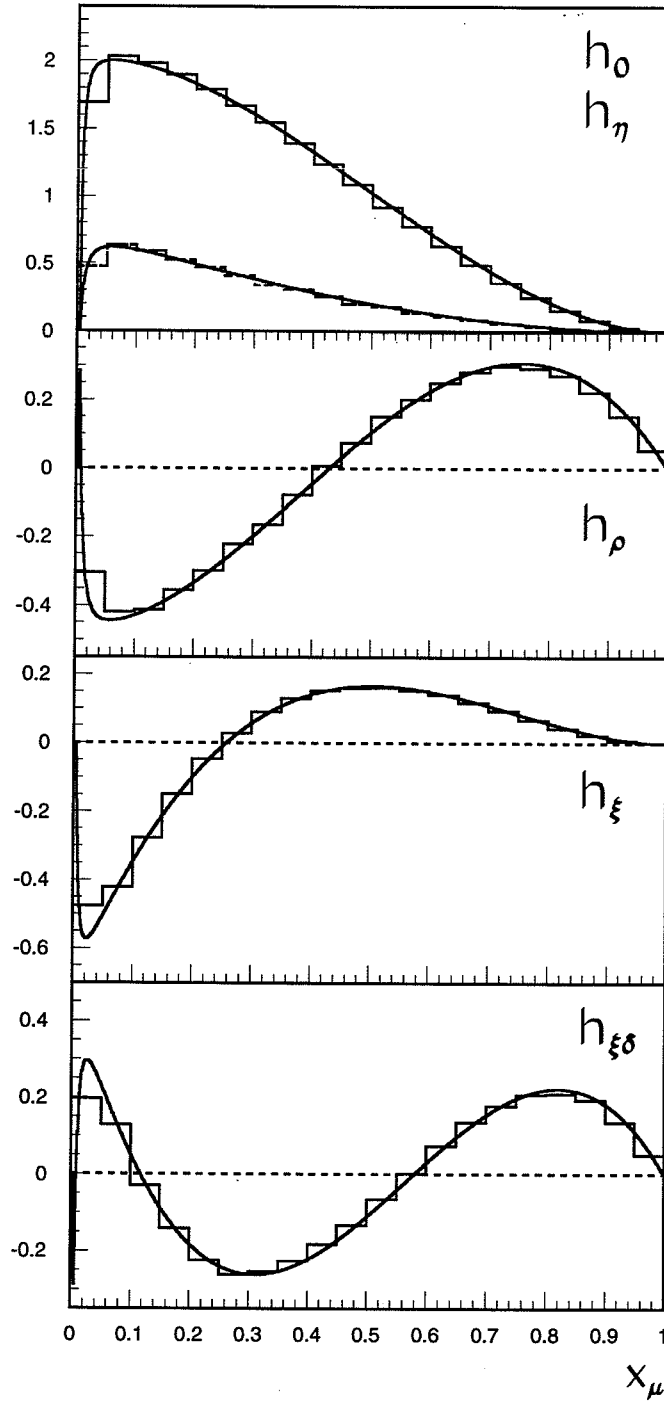


Figure 4.2: Spectral functions h_0 , h_η , h_ρ , h_ξ , $h_{\xi\delta}$ of the $\tau \rightarrow \mu \bar{\nu}_\mu \nu_\tau$ decay shown as histograms, obtained with the KORALZ generator [62] and the modified TAUOLA matrix element [64]. Superimposed solid lines represent Born level calculations.

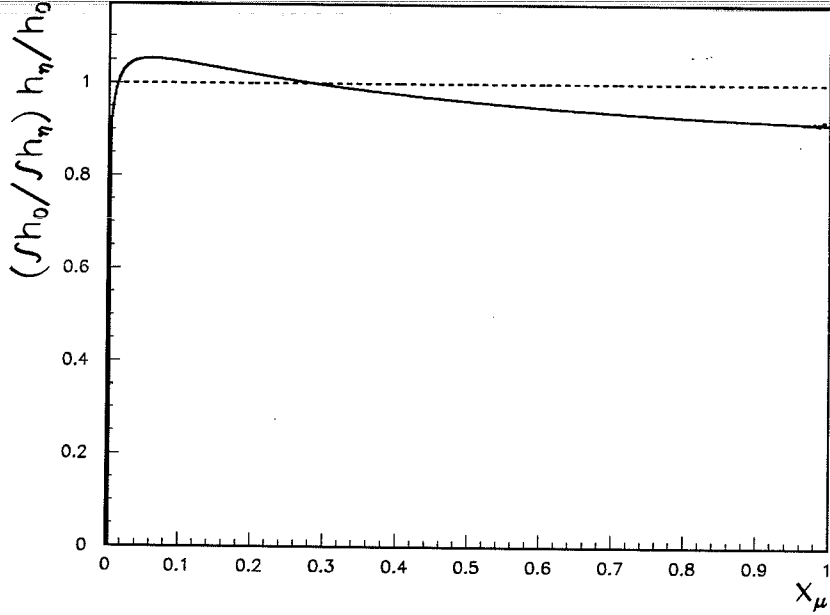


Figure 4.3: The ratio of equally normalized h_η and h_0 spectral functions (in Born level) of the $\tau \rightarrow \mu \bar{\nu}_\mu \nu_\tau$ decay shows relative sensitivity of polarization independent part of the muon spectrum to η parameter.

simply obtained by the following operations, written in the symbolic form as:

$$h_0(x) = A \quad (4.12)$$

$$h_\rho(x) = \frac{4}{3}(B - A) \quad (4.13)$$

$$h_\eta(x) = \frac{\Gamma_1}{\Gamma_0}C - A \quad (4.14)$$

$$h_\xi(x) = \frac{1}{2}(DR - DL) \quad (4.15)$$

$$h_{\xi\delta}(x) = ER - EL, \quad (4.16)$$

where Γ_1 (Γ_0) is the total τ decay rate (3.14) for $\eta = 1$ ($\eta = 0$), so that

$$\frac{\Gamma_1}{\Gamma_0} = \frac{f(\frac{m_l^2}{m_\tau^2}) + 4\eta \frac{m_l}{m_\tau}}{f(\frac{m_l^2}{m_\tau^2})}, \quad (4.17)$$

$f(\frac{m_l^2}{m_\tau^2})$ is a phase-space factor, $f(x) = 1 - 8x + 8x^3 - x^4 - 12x^2 \ln x$.

Results of this procedure for $\tau \rightarrow e \bar{\nu}_e \nu_\tau$ and $\tau \rightarrow \mu \bar{\nu}_\mu \nu_\tau$ decays are shown as histograms in Figures 4.1 and 4.2 together with tree level Born calculations superimposed. The effect of the radiative corrections on the decay spectrum is quite visible for the

$\tau \rightarrow e\bar{\nu}_e\nu_\tau$ decay, where the Born prediction shows harder behavior. For the $\tau \rightarrow e\bar{\nu}_e\nu_\tau$ decay, the $h_\eta(x)$ function is not plotted as it would be invisible at the given scale. This loss of sensitivity to η_e is due to the mass factor m_e/m_τ suppression in (3.8). As it is seen from Figs. 4.1 and 4.2, due to the high boost of the τ lepton, the sensitivity to other Michel parameters lies over the whole energy spectrum of the decay lepton. The possibility to measure η_μ comes from the different energy dependence of the h_0 and h_η spectral functions, seen on Figure 4.3. On the other hand, it is quite clear that all Michel parameters cannot be disentangled from the decay energy spectrum only.

4.1.2 Semileptonic decays

$\tau \rightarrow \pi(K)\nu_\tau$

For the hadronic τ decays, since there is only one missing neutrino, the τ rest frame decay angle can be calculated from the laboratory hadronic energy, assuming the τ lepton energy is equal to E_{beam} [61] :

$$E_h = \gamma_\tau(E_h^* + \beta_\tau p_h^* \cos \theta^*) \quad (4.18)$$

$$E_h^{\min} = \gamma_\tau(E_h^* - \beta_\tau p_h^*) = \frac{E_{\text{beam}}}{m_\tau} \left(\frac{m_\tau^2 + m_h^2}{2m_\tau} - \beta_\tau \frac{m_\tau^2 - m_h^2}{2m_\tau} \right) \simeq E_{\text{beam}} \left(\frac{m_h}{m_\tau} \right)^2 \quad (4.19)$$

$$E_h^{\max} = \gamma_\tau(E_h^* + \beta_\tau p_h^*) = \frac{E_{\text{beam}}}{m_\tau} \left(\frac{m_\tau^2 + m_h^2}{2m_\tau} + \beta_\tau \frac{m_\tau^2 - m_h^2}{2m_\tau} \right) \simeq E_{\text{beam}} \quad (4.20)$$

$$\gamma_\tau E_h^* = \frac{E_h^{\max} + E_h^{\min}}{2} \quad (4.21)$$

$$\gamma_\tau \beta_\tau p_h^* = \frac{E_h^{\max} - E_h^{\min}}{2} \quad (4.22)$$

hence,

$$\cos \theta^* = \frac{2E_h - (E_h^{\max} + E_h^{\min})}{E_h^{\max} - E_h^{\min}} = \frac{2E_h/E_{\text{beam}} - 1 - (m_h/m_\tau)^2}{(1 - (m_h/m_\tau)^2) \beta_\tau}, \quad (4.23)$$

where $\beta_\tau = \sqrt{1 - (m_\tau/E_{\text{beam}})^2}$. In the case of the $\tau \rightarrow \pi(K)\nu_\tau$ decay there are no other observables. In the approximation $(m_h/m_\tau)^2 \ll 1$, which is quite good for the $\tau \rightarrow \pi\nu_\tau$ decay, and $(m_\tau/E_{\text{beam}})^2 \ll 1$, (4.23) can be simplified to

$$\cos \theta^* = 2x_h - 1, \quad \text{where} \quad x_h = 2E_h/E_{\text{beam}}. \quad (4.24)$$

Thus, the decay distribution in the laboratory system is simply obtained from (3.21) using (4.24) and has the following form:

$$\frac{1}{\Gamma} \frac{d\Gamma}{dx_h} = 1 - P_\tau \xi_h (2x_h - 1). \quad (4.25)$$

In the general form, without a simplification of the decay kinematic and not neglecting radiative corrections, the decay distribution could be written as

$$\begin{aligned} \frac{1}{\Gamma} \frac{d\Gamma}{dx_h} &= H_0(x_h) - P_\tau H_1(x_h) \\ &= h_0^{(h)}(x_h) - P_\tau \xi_h h_1^{(h)}(x_h), \end{aligned} \quad (4.26)$$

where the functions $h_0^{(h)}$ and $h_1^{(h)}$ satisfy

$$\int h_0^{(h)}(x) dx = 1 \quad (4.27)$$

$$\int h_\xi^{(h)}(x) dx = 0. \quad (4.28)$$

The estimators of the functions h_0 and h_1 could be constructed from the generator in the same way as for the leptonic τ decays. One possible set of generated samples is shown in Table 4.2. To attain the precision of an estimation for every histogram bin

Sample	v	a
AL (only τ_L)	1	-1
AR (only τ_R)	1	-1

Table 4.2: A set of generated samples used for the construction of $h_0(x)$ and $h_1(x)$ estimators in the $\tau \rightarrow \pi(K)\nu_\tau$ and $\tau \rightarrow \rho\nu_\tau$ decays

better than 1% for 20 bins in the x_π spectrum, $\sim 10^6$ $\tau \rightarrow \pi\nu_\tau$ decays are generated for each sample. After histogramming of the π energy spectrum for each generator sample and their equal normalization, the h_0 and h_1 estimators are obtained by the following operations, written in the symbolic form as:

$$h_0(x_\pi) = \frac{1}{2}(AR + AL) \quad (4.29)$$

$$h_1(x_\pi) = \frac{1}{2}(AR - AL). \quad (4.30)$$

The result of this procedure for the $\tau \rightarrow \pi\nu_\tau$ decay is shown as histograms in Figure 4.4 together with the Born level calculations superimposed.

$\tau \rightarrow \rho\nu_\tau$

The $\tau \rightarrow \rho\nu_\tau$ decay is similar to the previous one, except that ρ helicity may have two possible values: 0 or -1, which could be analyzed through ρ decay distribution itself [53, 54, 55]. Alternatively, a method, originally developed for the τ polarization measurement [65], has been followed, which allows the reduction, without any loss of information, of the multi-dimensional distribution to the one-dimensional distribution

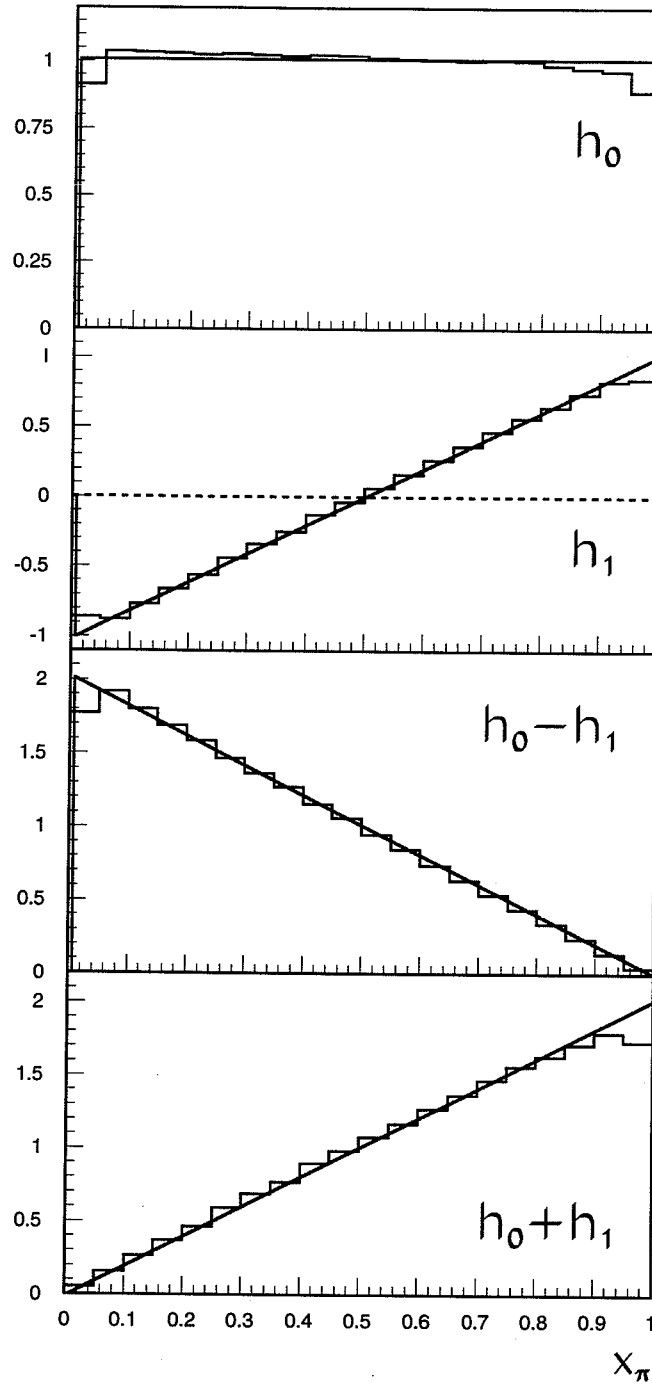


Figure 4.4: Spectral functions h_0 and h_1 of $\tau \rightarrow \pi \nu_\tau$ decay shown as histograms, obtained with the KORALZ generator [62]. Their difference $h_0 - h_1$ and the sum $h_0 + h_1$ give the π spectrum from *left-handed* and *right-handed* τ decays, respectively. Superimposed solid lines represent Born level calculations.

of a variable carrying all the sensitivity to ξ_h and P_τ . First, a general idea of this method is described and then its application to the $\tau \rightarrow \rho\nu_\tau$ channel is given.

For the hadronic τ decay channels the decay distribution can be written

$$\frac{1}{\Gamma} \frac{d\Gamma}{d\alpha} = h_0(\alpha) - P_\tau \xi_h h_1(\alpha), \quad (4.31)$$

where α designates a set of all possible kinematical observables, and the functions h_0 and h_1 satisfy the normalization and positivity conditions:

$$\int h_0(\alpha) d\alpha = 1, \quad \int h_1(\alpha) d\alpha = 0, \quad h_0(\alpha) \geq 0, \quad |h_1(\alpha)| \leq h_0(\alpha). \quad (4.32)$$

It appears that a maximum likelihood fit of the one-dimensional distribution of the variable $\omega = h_1(\alpha)/h_0(\alpha)$ have to the same sensitivity to ξ_h and P_τ as provided by a multi-dimensional analysis.

In the case of the $\tau \rightarrow \rho\nu_\tau$ decay, this definition leads to the decay distribution in the form:

$$\frac{1}{\Gamma} \frac{d\Gamma}{dQ^2 d\cos\beta d\cos\theta} = \hat{h}_0(\omega_\rho)(1 - P_\tau \xi_h \omega_\rho) \quad (4.33)$$

with ω_ρ variable

$$\omega_\rho = \frac{(-2 + \frac{m_\tau^2}{Q^2} + 2(1 + \frac{m_\tau^2}{Q^2}) \frac{3\cos^2\psi - 1}{2} \frac{3\cos^2\beta - 1}{2}) \cos\theta + 3\sqrt{\frac{m_\tau^2}{Q^2}} \frac{3\cos^2\beta - 1}{2} \sin 2\psi \sin\theta}{2 + \frac{m_\tau^2}{Q^2} - 2(1 - \frac{m_\tau^2}{Q^2}) \frac{3\cos^2\psi - 1}{2} \frac{3\cos^2\beta - 1}{2}}, \quad (4.34)$$

where the following variables are used [66]:

$$Q^2 = (E_{\pi^\pm} + E_{\pi^0})^2 - (\vec{p}_{\pi^\pm} + \vec{p}_{\pi^0})^2 \quad (4.35)$$

$$\cos\theta = \frac{2x_\rho - 1 - \frac{Q^2}{m_\tau^2}}{(1 - \frac{Q^2}{m_\tau^2})\beta_\tau} \quad (4.36)$$

$$\cos\psi = \frac{x_\rho(1 + \frac{Q^2}{m_\tau^2}) - 2\frac{Q^2}{m_\tau^2}}{(1 - \frac{Q^2}{m_\tau^2})x_\rho\beta_\rho} \quad (4.37)$$

$$\cos\beta = \frac{2}{|\vec{p}_{\pi^\pm} + \vec{p}_{\pi^0}|} \frac{(E_{\pi^\pm} - E_{\pi^0})(\vec{p}_{\pi^\pm} \vec{p}_{\pi^0}) + E_{\pi^\pm} |\vec{p}_{\pi^0}|^2 - E_{\pi^0} |\vec{p}_{\pi^\pm}|^2}{\sqrt{[Q^2 - (m_{\pi^\pm} + m_{\pi^0})^2][Q^2 - (m_{\pi^\pm} - m_{\pi^0})^2]}}. \quad (4.38)$$

In this case, θ is the angle between the ρ momentum in the τ rest frame and the τ momentum in the laboratory system, and β is the angle between the momentum of ρ in the laboratory system and the momentum of one of the pions from the ρ decay in the ρ rest frame. Notice that $-1 \leq \omega_\rho \leq 1$, i.e. ω_ρ is analogous to the cosine of the decay angle. Rewriting (4.33) as

$$\begin{aligned} \frac{1}{\Gamma} \frac{d\Gamma}{d\omega_\rho} &= H_0(\omega_\rho) - P_\tau H_1(\omega_\rho) \\ &= h_0(\omega_\rho) - P_\tau \xi_h h_1(\omega_\rho), \end{aligned} \quad (4.39)$$

the same procedure as in case of the $\tau \rightarrow \pi\nu_\tau$ decay is followed to construct the h_0 and h_1 estimators from the generated samples, shown in the Table 4.2, including effects of the decay phase-space and the dynamics of the ρ decay. The result is shown as histograms in Figure 4.5.

4.2 Global Fit Procedure

The decay distribution of the leptonic channels contains four Michel parameters ρ , η , ξ and $\xi\delta$. Two of them, ξ and $\xi\delta$, appear in product with P_τ . Hadronic decay distributions contain only the product $P_\tau\xi_h$. It is quite obvious that without making additional assumptions, it is impossible to measure τ decay parameters only from the single side decay distributions.

Using a joint distribution of the decay products from the τ pair allows to disentangle the contributions from the different τ decay parameters. The only remaining ambiguity is a two-fold sign ambiguity between P_τ and ξ , $\xi\delta$, ξ_h , which can be solved by fixing the sign of P_τ from other measurements. In the following, the procedure to obtain the decay parameters together with P_τ from a simultaneous fit to all possible distributions will be developed. First, assuming an ultimate resolution and a perfect acceptance inside a fiducial volume, an estimation is done how sensitive this fit is to the τ decay parameters and if there are any biases due to the method and/or statistics. Then, a method to account for the finite detector resolution and acceptance will be discussed.

Consider that the following exclusive decay channels

$$e^+e^- \rightarrow \gamma, Z \rightarrow \tau^-\tau^+ \rightarrow AB + \dots \quad (4.40)$$

are selected and classified, where A, B are e, μ, π and ρ . In addition, B might not be identified as one of these τ decay products: this case will designate as X . Following the construction of the decay distributions for these τ decay modes, it is straight-forward to use a binned maximum likelihood fit for the estimation of the τ decay parameters and P_τ . Assuming Poisson statistics in every bin, the likelihood function will be given by

$$\mathcal{L} = \prod_i \prod_j \frac{\nu_{ij}^{n_{ij}} e^{-\nu_{ij}}}{n_{ij}!} \quad (4.41)$$

where i denotes the spectra AB used in the fit, such as $ee, e\mu, e\pi, e\rho, eX, \mu\mu, \mu\pi, \mu\rho, \mu X, \pi\pi, \pi\rho, \pi X, \rho\rho$ and ρX , and j runs over the bins included in the fit, whereas n_{ij} and ν_{ij} are, respectively, the number of data events and the expectation value in bin j of spectra i .

The expectation value in a bin is proportional to the cross-section of the particular decay channel, integrated over a bin size. Since the integration of the cross-section is

$\tau \rightarrow \rho \nu$

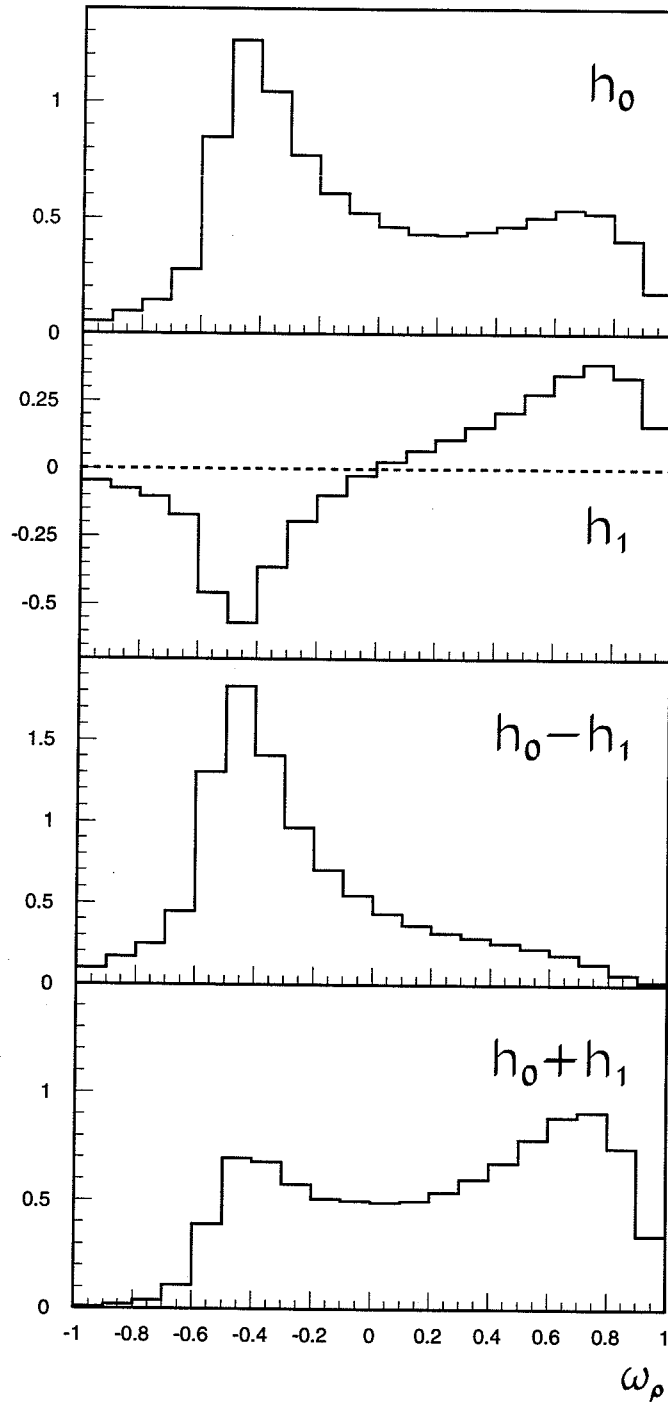


Figure 4.5: Spectral functions h_0 and h_1 of $\tau \rightarrow \rho \nu_\tau$ decay shown as histograms, obtained with the KORALZ generator [62]. Their difference $h_0 - h_1$ and the sum $h_0 + h_1$ give the ρ spectrum from *left-handed* and *right-handed* τ decays, respectively.

explicitly accounted for in the procedure of obtaining the H_0 and H_1 functions in the form of histograms, ν reads as

$$\nu_{Aj} \propto H_0^{(A)}(j) - P_\tau H_1^{(A)}(j) \quad (4.42)$$

in the case of a one-dimensional spectra and

$$\begin{aligned} \nu_{ABjk} \propto & H_0^{(A)}(j) H_0^{(B)}(k) + H_1^{(A)}(j) H_1^{(B)}(k) \\ & - P_\tau [H_1^{(A)}(j) H_0^{(B)}(k) + H_0^{(A)}(j) H_1^{(B)}(k)] \end{aligned} \quad (4.43)$$

for a two-dimensional spectra, where the dependence of the H_0 and H_1 on the τ decay parameters is given by (4.8) for the leptonic channels, (4.26) for $\tau \rightarrow \pi\nu_\tau$, and (4.39) for the $\tau \rightarrow \rho\nu_\tau$ decay. Concerning the normalization of the expectation value, there are several possibilities:

1. fix a normalization for each distribution to the number of events in the "data" N_i :

$$\sum_j \nu_{ij} = N_i; \quad (4.44)$$

2. let a normalization for each distribution be a parameter of the fit;
3. use extended maximum likelihood [67] instead of (4.41), with the likelihood function given by

$$\mathcal{L} = \prod_i e^{-\mathcal{N}_i} \prod_j \frac{\nu_{ij}^{n_{ij}} e^{-\nu_{ij}}}{n_{ij}!} \quad (4.45)$$

where \mathcal{N}_i is the expected total number of events in the spectra i .

This fit procedure has been checked with 10 samples of 150,000 $Z^0 \rightarrow \tau^+\tau^-$ events each, generated by KORALZ 3.8 [62, 64] for several sets of the Michel parameters. After applying "particle identification" inside the fiducial volume $|\cos\theta| < 0.74$ with momentum independent efficiency of 70%, each "data" sample consists of, on average, the following number of events for 14 exclusive channels:

$A \setminus B$	e	μ	π	ρ	X
e	1600	3200	2000	4000	13500
μ		1500	1850	3800	13000
π			600	2400	8000
ρ				2550	16000

The variables ² sensitive to the τ decay parameters and P_τ are calculated for each "identified" τ decay. Then, each event enters into only *one* distribution, according to

² $x_l = E_l/E_{\text{beam}}$ for leptonic τ decays, $x_\pi = E_\pi/E_{\text{beam}}$ for $\tau \rightarrow \pi\nu_\tau$ and ω_ρ for $\tau \rightarrow \rho\nu_\tau$ decay

its channel and the decay variables. One-dimensional spectra, eX , μX , πX and ρX , are binned into 20 equal bins and two-dimensional distributions, ee , $e\mu$, $e\pi$, $e\rho$, $\mu\mu$, $\mu\pi$, $\mu\rho$, $\pi\pi$, $\pi\rho$ and $\rho\rho$, are binned into 20×20 equal bins. Spectra having identical decays of both τ 's, ee , $\mu\mu$, $\pi\pi$ and $\rho\rho$, are folded across the diagonal owing to the symmetry of the cross-sections for these cases. The number of fitted bins totals to 3320. A typical sample has about 3000 bins with at least one "data" event. The expectation value is non zero in every bin. The fitting procedure then consists of varying the τ decay parameters and P_τ until the maximum of \mathcal{L} is found. This is done by minimization of $-\ln \mathcal{L}$ using the MINUIT package [68].

Set	Value	P_τ	ρ_l	η_l	ξ_l	$\xi_l \delta_l$	ξ_h
A	Used in generation	-0.136	0.75	0.	1.	0.75	-1.
	Weighted Mean	-0.136	0.749	0.008	0.955	0.767	-1.037
	Variance of Mean	0.010	0.013	0.074	0.064	0.047	0.019
	Mean Error	0.009	0.022	0.087	0.097	0.069	0.017
B	Used in generation	-0.136	0.75	0.	-1.	-0.75	-1.
	Weighted Mean	-0.145	0.742	-0.066	-1.009	-0.686	-1.000
	Variance of Mean	0.013	0.024	0.105	0.058	0.042	0.021
	Mean Error	0.010	0.023	0.093	0.095	0.070	0.021
C	Used in generation	-0.136	0.05	0.95	0.	0.05	-1.
	Weighted Mean	-0.141	0.039	0.870	-0.041	0.079	-0.988
	Variance of Mean	0.010	0.011	0.186	0.091	0.036	0.030
	Mean Error	0.009	0.012	0.205	0.101	0.036	0.019

Table 4.3: Results of the fit to the generated spectra, produced with different sets of Michel parameters.

The results of the fit with the first method of the normalization are presented in Table 4.3. The fit with two other methods of the normalization gives the same result. This could be explained by the fact that normalization parameters do not correlate during the fit with physical parameters. It is worthwhile to notice that there is no bias in the fit results due to the method itself. The average value for the normalized χ^2 of the fit is 1.015 ± 0.025 for Set A, 0.986 ± 0.028 for Set B and 1.003 ± 0.027 for Set C. The correlation matrix for the fit of the Set A, averaged over 10 samples, are given in Table 4.4. Note that P_τ correlates with ρ_l and anti-correlates with all other physical parameters. Michel parameter η_l highly correlates with ρ , whereas it is only slightly correlated with the others.

As it has been mentioned before, this fit does not determine the sign of P_τ , and, consequently, the signs of ξ , $\xi\delta$ and ξ_h . There are two equal maxima of the likelihood

function, which correspond to the same values of all other parameters, except P_τ , ξ , $\xi\delta$ and ξ_h have opposite signs. It is quite clear from (4.5), (4.8), (4.26) and (4.39), that these cross-sections have equal values for the following two sets of τ decay parameters and P_τ :

$$\rho, \eta, \xi, \xi\delta, \xi_h, P_\tau \quad \text{and} \quad \rho, \eta, -\xi, -\xi\delta, -\xi_h, -P_\tau.$$

One possible way to overcome this two-fold ambiguity is to fix the sign of P_τ using the LEP results on forward-backward polarization asymmetry A_{FB}^P [69, 70] and the SLD measurement of A_{LR} asymmetry [71]. The measurement of A_{FB}^P shows that the ratios of neutral current coupling constants g_V^e/g_A^e and g_V^τ/g_A^τ have the same sign, whereas A_{LR} determines the sign of g_V^e/g_A^e . Thus, the sign of P_τ is considered to be unambiguously defined as minus, $P_\tau < 0$, and the τ decay parameters can be completely determined from the global fit procedure.

The finite detector resolution, distortion of the acceptance and the background can be directly accounted for in the construction of the expectation value. Then, the expected signal distribution is given by the convolution of the theoretical cross-section together with the probabilities describing resolution \mathcal{R} and acceptance \mathcal{A} :

$$\text{Signal} = \mathcal{A}(a) \mathcal{R}(a|\alpha) \frac{d\sigma}{d\alpha}$$

where α and a denote respectively true and reconstructed values of the measured variables. In order to check this procedure, the L3 detector resolution and selection efficiency (see Chapter 6) have been applied on every generated event in the above samples. The same resolution and selection efficiency have been applied to obtain signal distributions. Here are the fit results for Set A, averaged over 10 samples, with the first method of normalization:

$$\begin{aligned} \rho_l &= 0.761 \pm 0.025 \\ \eta_l &= 0.07 \pm 0.11 \\ \xi_l &= 0.99 \pm 0.15 \end{aligned}$$

	ρ_l	η_l	ξ_l	$\xi_l\delta_l$	ξ_h
P_τ	0.326	-0.011	-0.033	-0.046	-0.205
ρ_l		0.566	-0.108	-0.125	-0.152
η_l			0.201	0.079	0.015
ξ_l				0.099	0.124
$\xi_l\delta_l$					0.156

Table 4.4: Averaged correlation matrix for the fit of the Set A.

$$\xi_l \delta_l = 0.72 \pm 0.09$$

$$\xi_h = -1.007 \pm 0.028$$

$$P_s = 0.134 \pm 0.011$$

The fit results from the other two sets show as well no bias within statistical errors. Finally, in the presence of background, the expected spectra are simply given by the sum of signal and background distributions.

Chapter 5

L3 detector at LEP

5.1 LEP

LEP is the CERN Large Electron Positron collider [72] located between the Jura mountains and Lac Lemman in an underground tunnel used to produce e^+e^- collisions at the Z^0 peak. The dimensions of the LEP ring, situated 50 to 170 meters underground with a circumference of 26.659 km, represent a compromise between the available radio-frequency (RF) power of the accelerating system and civil construction cost. The total cost of the LEP project reached a value of five billion French francs.

The LEP tunnel, with a diameter of 3.8 meters, holds a vacuum chamber, the so-called beam-pipe, with diameter of 10 cm, in which both electron and positron beams are accelerated. The chamber is constructed from aluminium covered with a lead cladding. In order to attain a reasonable luminosity and life time of beams, the whole vacuum chamber is pumped down to a pressure of 8×10^{-12} Torr. In the presence of beams the pressure rises to $\sim 10^{-9}$ Torr due to gas desorption from the inner vacuum chamber wall, provoked by the synchrotron radiation.

The LEP storage ring consists of eight 2840 m bending sections connected by eight 490 m long straight sections. Bending sections house beam optics, which comprise a total of 3368 dipoles, 816 quadrupoles, 504 sextupoles and 700 horizontal and vertical orbit correctors. Dipoles with a magnetic field of ~ 0.1 T steer the beams around the ring, quadrupoles produce alternating gradient focusing and sextupoles are used to compensate its energy dependence. The four LEP experiments, L3, ALEPH, OPAL and DELPHI, are located in the middle of alternate straight sections counting clockwise (Figure 5.1). To increase luminosity, beams are vertically squeezed by superconducting *low- β* quadrupoles situated on both sides of an experiment. In addition, a pair of quadrupoles rotated by 45° compensate for the coupling effect between horizontal and vertical betatron oscillations, introduced by each experimental solenoid. The straight sections containing L3 and OPAL have 128 accelerating units with a total maximum

available power of 14.8 MW that ramp the beams up to the nominal energy of 46 GeV and compensate for the energy lost by the beam, mainly due to synchrotron radiation and partially due to parasitic-mode losses coming from the accelerating structures, from the vacuum system, and from the beam separators.

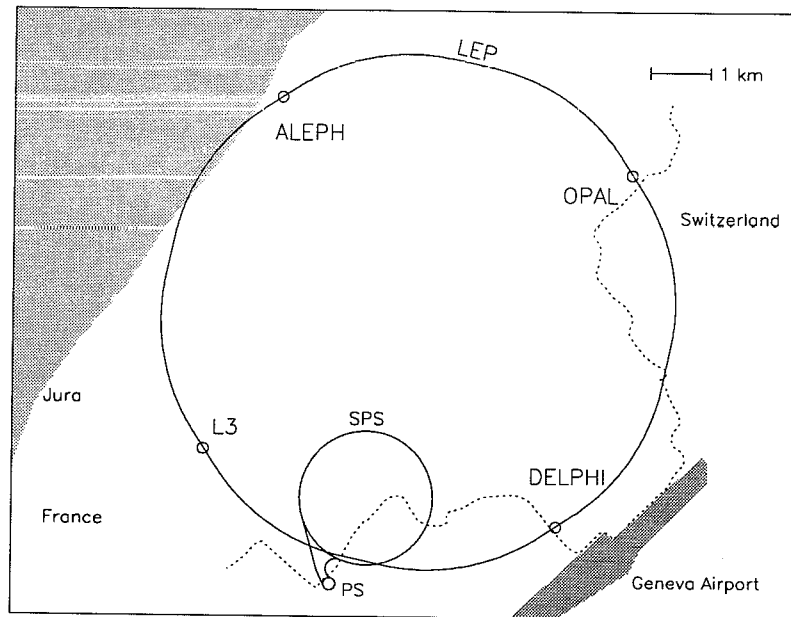


Figure 5.1: The LEP ring with locations of the four detectors.

To limit the total cost of the LEP project and to save time, two already existing CERN accelerators, the Proton Synchrotron (PS) and the Super Proton Synchrotron (SPS), have been used in the LEP injection chain. The LEP injection system is made from two linacs of 200 MeV and 600 MeV followed by a 600 MeV Electron-Positron Accumulator (EPA), which successively brings electrons and positrons into the PS serving as a 3.5 GeV e^+e^- synchrotron. The PS then injects into the SPS, which operates as a 20 GeV injector for the LEP main ring. LEP has a maximum designed beam energy of 55 GeV during the first stage of operation at the Z^0 peak, called LEP I.

Electron-positron interactions are produced by 4 + 4 (or 8 + 8 in “pretzel” scheme [73]) bunches of about 2×10^{11} particles each, circulating with a revolution time of 88.92 μs and colliding at four interaction points with an effective luminous region of $150 \times 30 \times 9000 \mu m^3$. These three numbers refer respectively to the direction along bending radius, perpendicular to the bending plane and along the beams and give a nominal LEP luminosity of $\mathcal{L} = 1.5 \times 10^{31} cm^{-2}s^{-1}$. A typical LEP fill lasts for about 12 hours of data taking giving an average integrated luminosity of 300–500 nb^{-1} .

5.2 The L3 detector

5.2.1 General description

The L3 experiment (Figure 5.2) is designed to study e^+e^- interactions at LEP collider with emphasis on high resolution energy measurements of electrons, photons and muons [74]. The L3 detector itself is installed at point 2 of the LEP storage ring inside a 26.5 m long and 21.4 m diameter experimental hall. In order to instrument the precise momentum measurement of muons, a large volume air magnetic spectrometer has been chosen, determining the overall L3 detector design. All detector components are installed within an 11.9 m long, 11.86 m inner diameter conventional magnet providing a 0.5 T solenoidal field along the beam axis.

The muon spectrometer consists of three layers of drift chambers, arranged in 16 octants around the beam, which is supported by and mounted outside of a 32 m long, 4.45 m outer diameter, 50 mm thick steel tube. The tube is concentric with the LEP beam pipe and symmetric with respect to the interaction point. It houses all other subdetectors, arranged as a "barrel" in the central region and as "endcaps" in the forward and backward directions. From the interaction point outwards the barrel consists of a central tracking system, an electromagnetic calorimeter, scintillator counters, a hadron calorimeter and a muon filter. The hadron calorimeter is built from depleted uranium absorber plates interspersed with proportional wire chambers. The electromagnetic calorimeter is composed of bismuth germanate (BGO) crystals. In the endcaps there are forward-backward tracking chambers, electromagnetic and hadron calorimeters. The luminosity monitors are situated on both sides behind the endcaps and immediately in front of the $low-\beta$ superconducting quadrupoles.

The L3 experiment is an effort involving a worldwide collaboration of 460 physicists from 33 institutions in 13 countries. The preparation of the experiment from its conception to the beginning of data taking in Summer 1989 took eight years at cost of \$200 million and 1100 technical man-years [74]. The detector performance and major results from the first three years of the L3 detector running at LEP are summarized in [75].

Positions and directions in L3 are specified in the right-handed coordinate system with its origin placed at the nominal e^+e^- collision point in the geometrical center of the detector. The positive z -axis points in the direction of the e^- beam, the positive y -axis points vertically upwards, and the positive x -axis points to the center of the LEP ring. The polar coordinates r , φ and θ , standardly defined through the Cartesian x , y , z coordinates, are also used. "Transverse" is used to refer to quantities in the plane perpendicular to the z -axis.

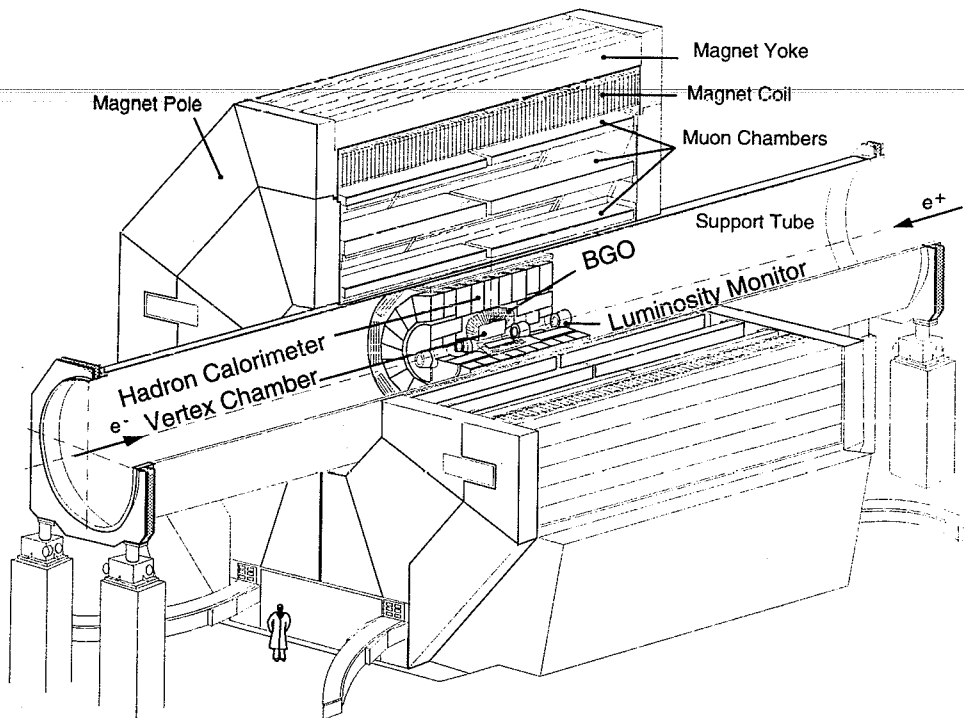


Figure 5.2: Perspective view of the L3 detector.

5.2.2 Magnet

All L3 subdetectors are mounted inside a large octagonal aluminium coil, surrounded by soft iron yoke and closed at both sides by two poles equipped with hinged doors.

The coil is made of industrial aluminium plates welded together on the CERN site into 28 packages, 6 turns each, which are then bolted together. It has a total weight of 1100 t. Water cooling is provided by two independent circuits made of an aluminium alloy with high resistance to corrosion and welded onto the inner and outer edges of the coil. An active thermal shield placed on the inside of the coil protects the detector.

The magnetic structure of the yoke is made of soft iron with 0.5% carbon content. The poles are made of an 1100 t self-supporting steel structure, giving the required rigidity and serving as a support and reference frame to mount the 5600 t of filling material, which provides the mass needed for the magnetic flux return, both in the barrel and in the poles. A pole consists of two parts, the crown and the double doors, to allow installation of the muon spectrometer.

The power supply is a thyristor converter delivering a maximum current of 31.5 kA at 150 V. It consists of two transformers followed by six banks of water cooled thyristor equipped with passive filters and diodes. The power supply is installed in the surface hall and connected to the magnet through the shaft with a set of 82 m long water cooled bus bars made of aluminium tubes. The magnet coil is grounded in the middle

through a resistance of 1Ω . The central field of 0.5 T is provided by rated current of 30 kA with a total stored magnetic energy of 150 MJ.

The magnetic field inside the support tube is mapped with Hall probes. In the remaining volume it is measured by about a thousand magnetoresistors permanently mounted on the muon chambers.

5.2.3 Muon Spectrometer

The L3 muon spectrometer [76] was designed and constructed to measure muon momentum with a resolution of $\sigma_p/p \simeq 2.5\%$ at 45 GeV. To minimize effects of multiple scattering in matter, a large volume air spectrometer is employed with track *sagitta* measurement. When the sagitta $s \ll$ the analyzing lever arm L , $\sigma_p/p = \sigma_s/s \sim \sigma_s p / BL^2$. It was chosen to have a large lever arm ($L = 2.9$ m) combined with a moderate magnetic field ($B = 0.5$ T), giving a sagitta of 3.6 mm for a 45 GeV muon track. To reach the designed momentum resolution, the sagitta has to be measured with a precision approaching $85 \mu\text{m}$.

The muon spectrometer comprises of three equidistant layers of multiwire drift chambers arranged in 16 independent *octants*, mounted outside the support tube around the beam direction. Each octant consists of an aluminium mechanical structure supporting the drift chambers and attached to the torque tube. There are five *P-chambers* in each octant: two outer (MO) and two middle (MM) chambers and one inner (MI) chamber (see Figure 5.3). The inner and the outer chambers are closed on the top and bottom by *Z-chambers*. The middle chambers are closed by honeycomb panels to reduce multiple scattering. P-chambers measure track momentum in the bending $r - \varphi$ plane, whereas Z-chambers measure track slope in non-bending $r - \theta$ plane.

P-chambers are constructed of two cast and machined aluminium end frames and two extruded aluminium side planes. Each MO chamber is divided into 21 identical drift cells with 16 anode wires, each MM chamber has 15 cells with 24 wires, and each MI chamber contains 19 cells with 16 wires. The chamber cell has been designed to have a uniform electric field throughout the drift region. Sense wires with a diameter of $30 \mu\text{m}$ are spaced 9 mm apart and are interspersed with field shaping wires, forming a signal plane in the middle of a drift cell. Beyond the last sense wire, eight additional wires equalize the drift time behavior of all the sense wires within 0.2 ns ($10 \mu\text{m}$). A plane of $75 \mu\text{m}$ diameter cathode wires, spaced 2.25 mm apart, is located 50.75 mm from the sense wire plane.

The accuracy of the wire location within the chamber is achieved by pulling the wires over the corners of optically flat ($\leq 2 \mu\text{m}$) Pyrex glass pieces which are glued on carbon fiber rods. This glass *bridges* are glued on a precision template and have almost

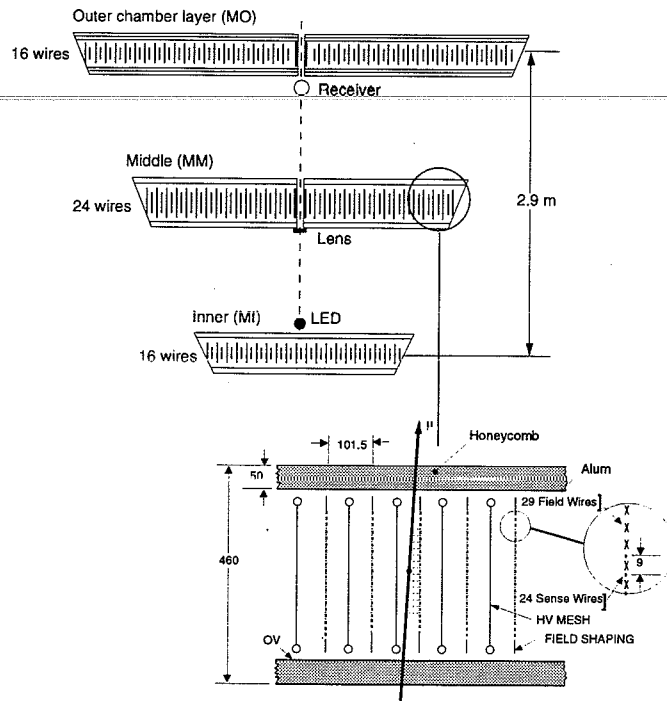


Figure 5.3: Layout of the muon spectrometer octant and the drift cells of the P-chambers.

no thermal expansion. Wires of the cell are planar to $2 \mu\text{m}$ and the cells are located to an accuracy of $4.9 \mu\text{m}$. To reduce the gravitational sag of the 5.6 m long wires from $380 \mu\text{m}$ to $95 \mu\text{m}$ and to avoid wire displacement due to the electrical forces, the wires are supported in the middle by an additional bridge of the same construction. The middle bridge is kept aligned to the rest of the chamber frame by an optical *straightness monitor* [77], which is able to detect movements of less than $5 \mu\text{m}$.

The chamber volume is filled with an $\text{Ar}:\text{C}_2\text{H}_6$ (61.5 : 38.5) gas mixture with ~ 2000 ppm water vapor added to prevent aging. Four different high voltages are applied to the sense, field, cathode and guard wires, allowing to control the drift field, the gas amplification and the zero potential position. The chamber is operated with a drift field of 1100 V/cm . In a magnetic field of 0.5 T , the drift velocity is $4.86 \text{ cm}/\mu\text{s}$ and the Lorentz angle is 18.6° . Signals are amplified with a gain of $24 \text{ mV}/\mu\text{A}$ discriminated on the leading edge with a threshold of $\sim 1/10$ of the averaged pulse height, and then digitized by 500 MHz Fastbus LeCroy TDCs. The T_0 of each wire, defined as the signal timing with zero drift distance, is calibrated by an external pulse generator. The electronic noise is less than 10 mV and allows the chambers to be operated with a relatively low gas amplification of 5×10^4 . Out of the total 250000 wires, the averaged rate of wire breaking over the three years of data taking is one wire every month.

The drift time-distance dependence (*cell map*) has been obtained in test beam

runs under operating conditions similar to those at LEP [78]. During the test beam, the values of cell map variables, such as the slope of a particle track, drift time for the ionization trail, magnetic field, temperature and pressure, have been varied over the full range expected in operation. The single wire resolution has been measured with cosmic ray tracks by the residual of a straight line fit and found to be $220 \mu\text{m}$ averaged over the cell. This provides an intrinsic sagitta resolution due to the chamber of $60 \mu\text{m}$.

There are also six Z-chambers [79] in the octant, which cover the top and the bottom of the MI and MO chambers, to measure z coordinates of the track along the beam. Each Z-chamber consists of two layers of drift cells offset by one half cell with respect to each other to resolve left-right ambiguities. Each cell has two parallel aluminium I-beam profiles connected to -2.4 kV and in the center one gold plated molybdenum anode wire with $50 \mu\text{m}$ diameter at $+2.15 \text{ kV}$. The cell is closed by two aluminium sheets at ground potential and isolated from the I-beam profiles by fiber glass strips. Single wire resolution, measured both in the test beam with a prototype and with cosmic rays in production chambers, is typically $500 \mu\text{m}$.

As a muon from the interaction point with momentum greater than 4 GeV travels through only one octant, precision alignment is necessary only within the octant. The alignment of the chambers is done by the same straightness monitor mentioned previously. Two sets of the monitors, mounted along octant central lines at both sides, measure the position of the MM layer relative to the MO and MI layers. The planarity of the octant central plane is achieved by adjusting the six reference points (three points at each side of the octant where the straightness monitors are located) to the plane defined by a laser beacon [80]. Sensors mounted on the straightness monitors enable to measure and eliminate the torsion to less than $50 \mu\text{rad}$. Being optomechanically aligned as described above, every chamber alignment had been further verified by eight UV laser rays traversing the octant and by cosmic rays measured without a magnetic field before the installation into the detector [81]. Since the tolerance in y positioning is larger, the chamber spacings in the y direction are fixed by the octant structure and are not monitored and are not adjustable once the octants are assembled. Due to multiple scattering in the inner detectors, a 2 mm positioning accuracy of the octants relative to the beam line is sufficient. The optical alignment system has been continuously operational throughout data taking and shows better than $30 \mu\text{m}$ mechanical stability of the octant frames. Muon tracks in every event have been corrected for misalignment according to the most recent straightness monitor and laser beacon data.

The muon spectrometer covers the angular range $|\cos \theta| < 0.8$. For tracks crossing all three layers, the transverse momentum is calculated from the sagitta measurement in the P-chambers and is used together with the θ measurement in the Z-chambers to reconstruct the 3-momentum of the track. Tracks in the angular region $|\cos \theta| > 0.71$ do not cross the outer layer of the spectrometer. For such tracks, transverse momentum

is reconstructed from the difference of the track slopes in the two layers, which are measured to an accuracy of 1 mrad.

5.2.4 Hadron Calorimeter

The hadron calorimeter (HCAL) is designed, together with the BGO crystal calorimeter placed in front of it, to measure the total energy of jets and single hadrons produced in e^+e^- collisions. High longitudinal segmentation of the HCAL is also used to identify penetrating muons by their minimum-ionizing track-like signature. The HCAL serves as well to shield the muon chambers by absorbing showering particles. To extend the total absorption length of the HCAL, a muon filter is mounted just inside the support tube (Figure 5.4).

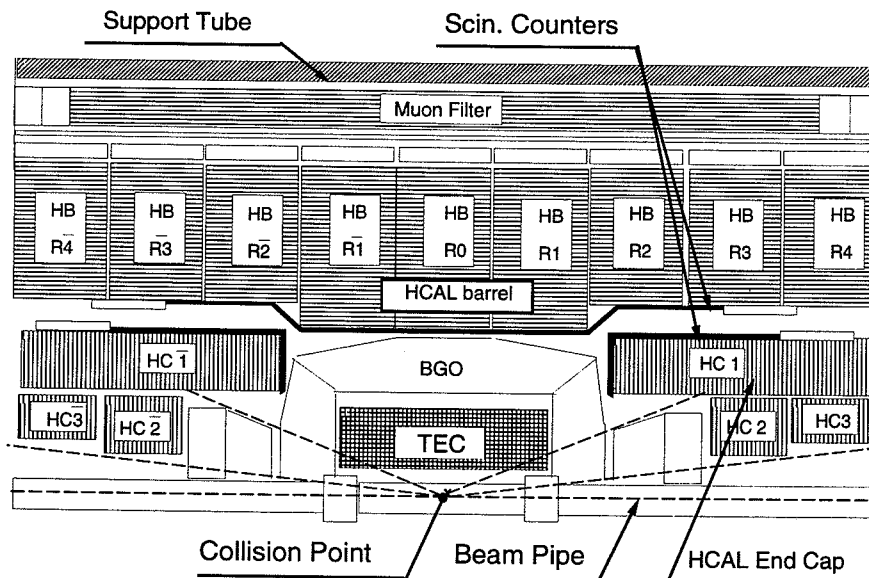


Figure 5.4: Longitudinal cut view of the hadron calorimeter and muon filter.

The HCAL consists of depleted uranium absorber plates interspersed with gas proportional wire chambers (PWC). The use of uranium, with its short absorption length, is motivated by the requirement of a compact calorimeter, allowing the longest possible lever arm for the muon momentum measurement. Gas proportional wire chambers have been chosen as the detecting element for their long time stability and reliable operation in a magnetic field. The HCAL is mechanically divided into a barrel and two endcaps.

The HCAL barrel consists of 144 modules grouped into 9 rings each containing 16

modules and covers the polar angular region $25^\circ < \theta < 155^\circ$ over the full azimuthal range. Three central rings contain *long modules* of 60 chambers interleaved with 58 uranium plates. Six outer rings contain *short modules* with 53 chambers and 51 uranium plates each.

The uranium plates are 5 mm thick and plated with a 20 μm copper-nickel alloy. They are cut to specified sizes and clamped into place in supporting bars which lie along the parallel faces of the modules.

The proportional wire chambers [82] are made up of brass tubes of 5 mm \times 10 mm interior cross section and 0.3 mm wall thickness. These are assembled into planes, cemented together with adhesive-coated mylar insulating sheet, and sandwiched between sheets of 0.7 mm brass for structural strength and radiation (β -ray) shielding. The assembled planes are fitted with plastic end-pieces, which carry gold-plated end-jacks with 50 μm diameter gold-plated tungsten anode wires crimped into them. The chambers have from 33 to 58 tubes per plane, and vary from 35 cm to 61 cm in their maximum dimension. The chambers, filled with 80% argon + 20% carbon dioxide gas mixture at atmospheric pressure, are operated with negative high voltage applied to the cathode (brass tube) and the anode wire at ground potential, permitting direct coupling into the preamplifier.

At the operating high voltage of 1600 V, the gas gain is about 10^4 . An inorganic filling gas and low gas gain were chosen in part to reduce possible aging effects on the chambers in the radiation environment of the uranium.

The chamber planes are oriented with wires in alternating layers at right angle to each other and grouped into readout cells (*towers*). Each tower includes only wires from the alternate layers. The pattern of wire groupings provides 9 towers in z and φ directions in each module, and has in both directions 10 towers in depth (radially from the beam line) for long modules and 8 towers for short modules. In the $r - \varphi$ plane, each tower subtends about 2.5° from the beam axis, whereas in the $r - z$ plane they have a constant width of about 5 cm, also corresponding to about 2.5° in the central region. The integral depth of the calorimeter in nuclear interaction length for 20 GeV pions (λ) varies from 3.52 at $\theta = 90^\circ$ up to 5.22 at $\theta = 39^\circ$. Overall the HCAL barrel is 4725 mm long, 1795 mm outside and 886 mm inner radius, and has a weight of 261240 kg, including 177840 kg of uranium.

The endcaps of the hadron calorimeter subtend a polar angle between 5.5° and 35° , and between 145° and 174.5° , thus partially overlapping with the barrel (Figure 5.4). Each of the two endcaps is constructed of one outer and two inner rings. For mechanical reasons each ring is in turn divided vertically into two half-rings. The forward part of the outer ring ($\approx 1.3\lambda$) has the same sampling as the barrel, while the rest has a sampling twice as coarse. The PWC wires are stretched azimuthally, measuring the polar angle θ directly. Alternate chambers layers are oriented at 22.5° with respect to

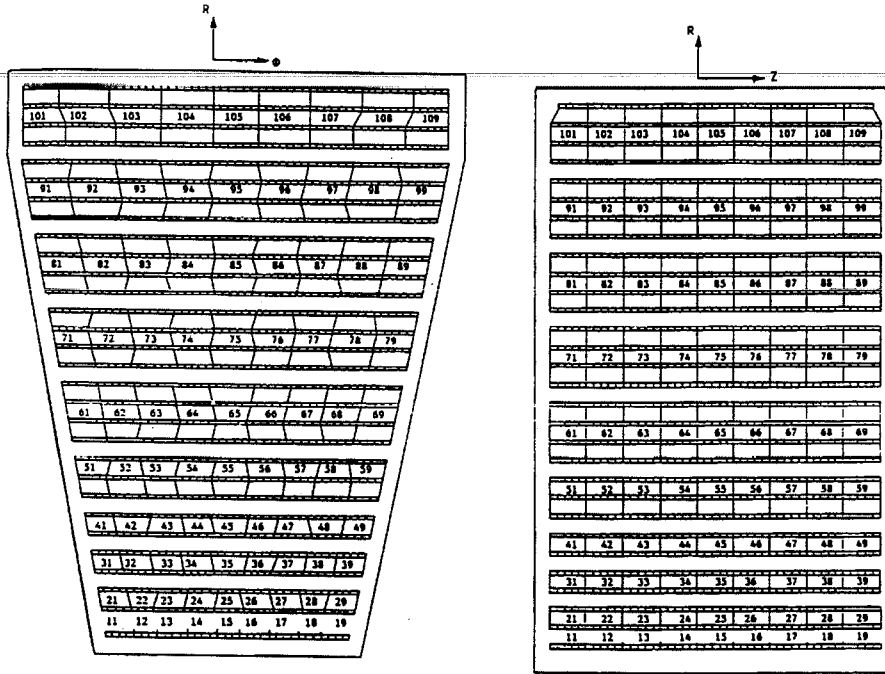


Figure 5.5: $r - \varphi$ and $r - z$ cut view of long module in HCAL barrel with chambers grouped into readout towers.

each other to provide two stereo views. The wire signals are grouped to form in the $r - \varphi$ plane 31 roads with about 1° of θ width pointing to the interaction region. The segmentation in azimuth is 22.5° , defined by the chamber dimensions. The longitudinal segmentation in the z direction is 5 for the inner rings and 7 for the outer rings. In the region not overlapping with the barrel, the depth of the endcap calorimeter is about 6 nuclear interaction lengths.

The towers are read out through LeCroy FASTBUS 1882F ADCs, 12-bit for the barrel and 15-bit for the endcaps. During normal data taking, the channels are readout only if their energy is above threshold, which corresponds to a hadronic energy of 9 MeV. The channel intercalibration is done using ionization signals from the uranium radioactivity detected in the PWC, the so-called *U-noise*. It has been found that the *U-noise* spectrum with random gating has a unique shape which can be fitted to obtain a total gain for each channel with an accuracy of better than 2% [83]. The intercalibration constants are applied during off-line reconstruction to the amplitudes measured in the corresponding readout channels. The high voltage and chamber gas are continuously monitored and held constant to within 0.1%. The long-term stability of the HCAL as a whole is found to be better than 1.3%.

Several test beam studies of the HCAL in beams of hadrons, electrons and muons, with and without BGO crystal calorimeter in front of it, have been performed [82, 83,

84] and an energy resolution of $55\%/\sqrt{E} + 5\%$ for pions have been found. The total energy resolution measured in hadronic Z^0 decays is about 10% in the barrel part, with a single hadron jet angular resolution of 35 mrad. [85].

The muon filter is mounted on the inside wall of the support tube (Figure 5.4) and adds about one absorption length to the HCAL. It consists of eight identical octants, each made of six brass absorber plates, interleaved with five layers of proportional chambers with wires oriented along the z direction. The chambers use the same gas mixture as the HCAL and operate at about 1800 V. The 8064 channels readout system is the same one as used for the HCAL barrel. Angular and coordinate information from the HCAL and the muon filter, which has 2 mm angular resolution in the $r - \varphi$ plane, are used during the off-line reconstruction to resolve ambiguities in the muon drift chambers.

5.2.5 Scintillation Counters

The scintillation system consists of 30 barrel counters, located between the barrel electromagnetic and hadron calorimeters, and 32 counters located in front of the either hadron endcap (Figure 5.4). They are made of 1 cm thick BICRON BC-412 plastic scintillators with a time resolution of 1 ns and are readout by Hamamatsu R2490-01 photomultipliers through UV transparent Plexiglass GS218 light guides. The total 92 signals are digitized by a LeCroy FASTBUS TDC 1875 with 50 ps resolution and a dynamic range of 15 bits, and by a LeCroy 1885 ADC for pulse charge intergration. This allows to improve the time resolution of the counters by a factor of two by applying time slewing corrections.

The barrel counters are from 167 mm to 182 mm wide and are bent to follow the shape of the hadron calorimeter barrel. The projected length of the scintillator is 2900 mm. The endcap counters are 270 mm long and 275 mm wide on one side and 180 mm on the other. The barrel counters have a polar angular range $|\cos \theta| < 0.83$ and the endcap counters extend the coverage down to $|\cos \theta| < 0.9$, and cover 93% of the azimuth.

The time resolution of better than 0.5 ns coupled with the fast readout system provides online rejection of cosmic rays. The time-of-flight difference between opposite counters is about 6 ns for a cosmic muon which passes near the interaction point, whereas for a dimuon pair produced in Z^0 decay the difference is zero.

5.2.6 Electromagnetic calorimeter

The electromagnetic calorimeter comprises 10734 bismuth germanate ($\text{Bi}_4\text{Ge}_3\text{O}_{12}$) crystals, pointing towards the interaction region and arranged in a barrel, which covers the region $|\cos \theta| < 0.72$, and two endcaps, with the forward endcap covering

$0.8 < \cos \theta < 0.98$ and the backward endcap covering $-0.98 < \cos \theta < -0.8$ (Figure 5.6). The barrel part consists of two symmetrical half-barrels and contains 48 rings of 160 crystals, forming a cellular structure in the θ - φ plane. The inner radius of the barrel is 525 mm for $\theta = 90^\circ$. A small (about 10 mrad) angular offset (tilt) of crystals in φ with respect to the interaction region is made to suppress energy leakage. Each endcap contains 17 rows in θ with every row in the crown, formed by three consequent rows starting from the external edge, having the same number of crystals: 128, 112, 96, etc. Both endcaps are situated at about 758 mm in z direction on either side of the interaction region.

Each crystal of the calorimeter is a truncated pyramid about 24 cm long, which corresponds to roughly 22 radiation lengths or 1.1 nuclear interaction lengths [86], with an almost square cross section of $2 \times 2 \text{ cm}^2$ on the front face and $3 \times 3 \text{ cm}^2$ on the back face (Figure 5.7). After production, all crystals were polished and then coated with a 40–50 μm thick layer of high reflectivity paint. The tolerances of crystal dimensions are on the order of 100 μm to minimize dead space between crystals. Each crystal has two photodiodes (Hamamatsu S2662 with 1.5 cm^2 active area) glued on its rear face to collect the BGO scintillation light. A charge sensitive preamplifier (Toshiba 2SK147-FET) with an output pulse rise time of 300 ns (corresponding to the BGO light decay time) is mounted directly a few centimeters behind the crystal. The main amplifier and ADC boards (Level-1), one for each crystal, are located at a distance of about 2 m away. The digitizing range of the ADC is equivalent to a 21 bit ADC, with resolution of 0.1% for a signal greater than 100 MeV. The linearity is better than 1% over the full range. A microcomputer (Level-1 readout), one for each crystal, completes the digitizing and stores the data within 250 μs after the trigger. They are organized in token ring networks by group of 60, each ring being controlled by a single VME board Motorola 68010 (Level-2 readout), located about 100 m away in the counting room. The higher levels of readout (Level-3 and 4) perform tasks of subdetector event builder. Dead and noisy crystals are detected on-line and put into the database.

The negative value of the BGO output light variation with temperature ($-1.55 \text{ \%}/^\circ\text{C}$) requires to maintain the BGO calorimeter at the lowest possible temperature above the dew point. To minimize the temperature gradient along the crystals, the BGO calorimeter is surrounded by very thin active thermal shields and the preamplifier boards are covered with a cooled brass screen. The temperature of BGO crystals is monitored by 1280 sensors, mounted on the front and back faces of the every 12th crystal. The temperature of the crystals is controlled to within $\pm 0.5 \text{ }^\circ\text{C}$.

Using the crystals as both a showering and a detection medium reduces the sampling fluctuations, resulting in excellent energy resolution over a wide range of energies for electromagnetic showers. The measured energy resolution of the BGO calorimeter is better than 2% between 1 GeV and 46 GeV and dominated by noise at low energies

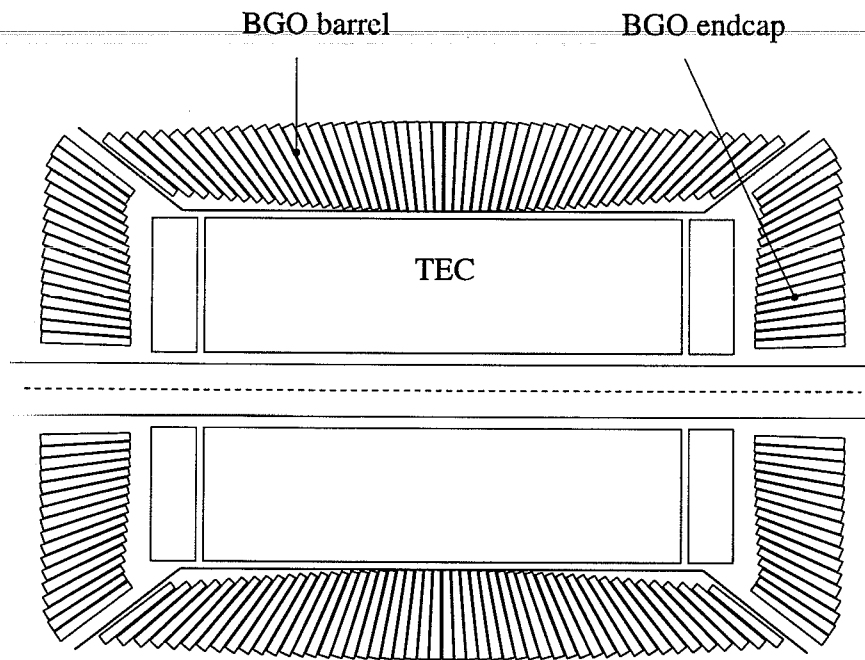


Figure 5.6: Longitudinal cut view of the BGO electromagnetic calorimeter showing the projective geometry of the crystal arrangement.

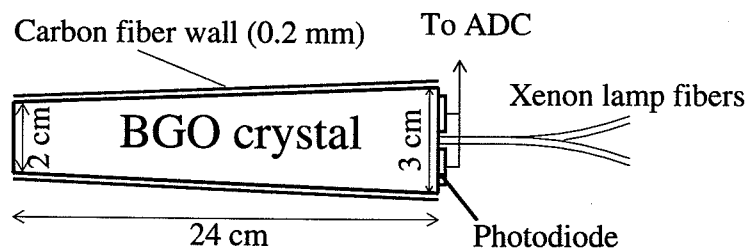


Figure 5.7: A BGO crystal side view. Two photodiodes are used to measure the light output.

and by a constant term above 10 GeV. The resolution of the BGO calorimeter can be parametrized as

$$\frac{\sigma_E}{E} = \sqrt{\left(\frac{a}{\sqrt{E}} + c\right)^2 + \frac{b}{E^2}} \quad (\%) \quad (5.1)$$

where $a = 1.50 \pm 0.05$, $c = 1.02 \pm 0.09$, $b = 1.12 \pm 0.40$ [87] and E is an electron energy in GeV. The term proportional to $1/E^2$ in the above expression measures the contribution from the correlated electronic noise. The absolute *in situ* calibration of the BGO calorimeter and its stability are maintained by a Xenon Light Monitor [88], Bhabha scattering data and cosmic rays runs [89, 90]. For the barrel part, the intercalibration of the crystals is stable to within $\pm 0.2\%$ over a typical period of 45 days or to within $\pm 0.5\%$ during a full year. Calibration constants for each crystal in the barrel were determined from a test beam study in 1988 with 2, 10 and 50 GeV electron beams produced by the CERN SPS. The experimental setup of that test beam and details of its analysis procedure can be found in [91, 92].

Due to the fine segmentation of the crystal array of the calorimeter relative to the BGO Molière radius of 2.4 cm [86], electromagnetic showers in the quoted above energy range typically involve nine or more crystals, allowing precise reconstruction of shower centroids. The impact point of the electron (photon) on the crystal is determined from the center of gravity of the energy deposited in a 3×3 crystal matrix centered on the most energetic crystal with the following empiric formula, deduced from the test beam study

$$X_{IP} = A \cdot \arctan(B \cdot X_{COG}) + C \cdot X_{COG} \quad (\text{mm}) \quad (5.2)$$

where $A = 6.023$, $B = 0.53$ and $C = 0.215$ [91]. Measured position resolution ranges from about 5 mrad at 1 GeV to 1 mrad at 45 GeV and can be parametrized, in the $r - \varphi$ plane, as

$$\sigma_\varphi = \frac{a}{\sqrt{E}} + b \quad (\text{mrad}) \quad (5.3)$$

where $a = 6.0 \pm 0.4$ and $b = 0.3 \pm 0.1$, and E in GeV [92].

The low level of sampling fluctuations and the fine segmentation of the BGO calorimeter also allow precise analysis of the transverse energy deposition profile of a shower, providing discrimination between its electromagnetic and nonelectromagnetic origins. For this purpose the shower shapes, which represent the average fraction of the total energy in each of the nine crystals in the 3×3 matrix centered on the most energetic one as a function of the impact point of the particle, have been determined from the test beams with electrons [91] and pions [84].

5.2.7 Central Tracking System

The L3 central tracking system was designed and constructed

- to measure the transverse momentum and determine the sign of charged particles;

- to measure the polar angle of tracks;
- to determine the charge multiplicity of an event;
- to reconstruct the interaction point and secondary vertices in an event;
- to determine the impact point of charged particles onto the BGO calorimeter.

Due to the low magnetic field and the short lever arm available inside the BGO electromagnetic calorimeter, an excellent coordinate resolution is mandatory to achieve the outlined above tasks. The central tracking consists of a Time Expansion Chamber (TEC), a layer of Plastic Scintillating Fibers (PSF) and two thin wire chambers with cathode readout (Z-Detector) [93, 94, 95] (Figure 5.8).

TEC is a cylindrical chamber with a detection volume of 0.61 m^3 formed by a 1.5 mm thick, 170 mm diameter beryllium inner tube just outside the beam pipe, a 4 mm thick aluminium outer cylinder with diameter of 937 mm and two 45 mm thick aluminium end-plates. Total sensitive length of the detection volume is 980 mm. TEC is filled with a gas mixture of 80% carbon dioxide and 20% isobutane at an absolute pressure of 1.2 bar. Presence of the electronegative oxygen contamination is maintained at a maximum limit of 1.7 ppm. The temperature control system stabilizes the TEC temperature at $18 \text{ }^\circ\text{C}$ with a maximum variation of $\pm 0.3 \text{ }^\circ\text{C}$.

The chamber is divided into two concentric cylinders, the inner and outer chambers with 12 and 24 sectors respectively. The configuration of the TEC sector geometry is shown in Figure 5.9. The electron drift volume is divided into a region with a low, homogeneous electric field and an amplification region with a high electric field on either side of the sense wire plane. The two regions are separated by a plane of grid wires at zero potential. The grid plane is made of $100 \text{ }\mu\text{m}$ gold plated copper-beryllium wires with a 0.6 mm spacing. The distance between two consecutive anodes, made of $20 \text{ }\mu\text{m}$ gold plated tungsten wires, is 4.8 mm. The anodes are alternated with focus wires, which allow for the adjustment of the track length sampled by the anodes. The wires are supported by the end-plates, which bend less than $100 \text{ }\mu\text{m}$ under the full load of the 30000 wires. Single wires are kept in position by feed-throughs sitting in the precision holes of the end-plates. The precision of wire positions in the anode planes is $\pm 50 \text{ }\mu\text{m}$. The grid wires are stamped onto two holders, which are then fitted into the high precision grooves on the end-plates. The precision of wire positions in the grid planes is $\pm 5 \text{ }\mu\text{m}$. The torsion between two end-plates is at most $\pm 0.08 \text{ mrad}$, which corresponds to $\pm 36 \text{ }\mu\text{m}$ at the outer diameter of the plates. The end-plates are parallel within $\pm 50 \text{ }\mu\text{m}$.

The high voltage system supplies negative voltage to the cathodes and four different positive voltages for the anodes, the innermost, normal and the outermost focus wires. Since TEC is operated with a low drift velocity, linearly dependent on the value of the

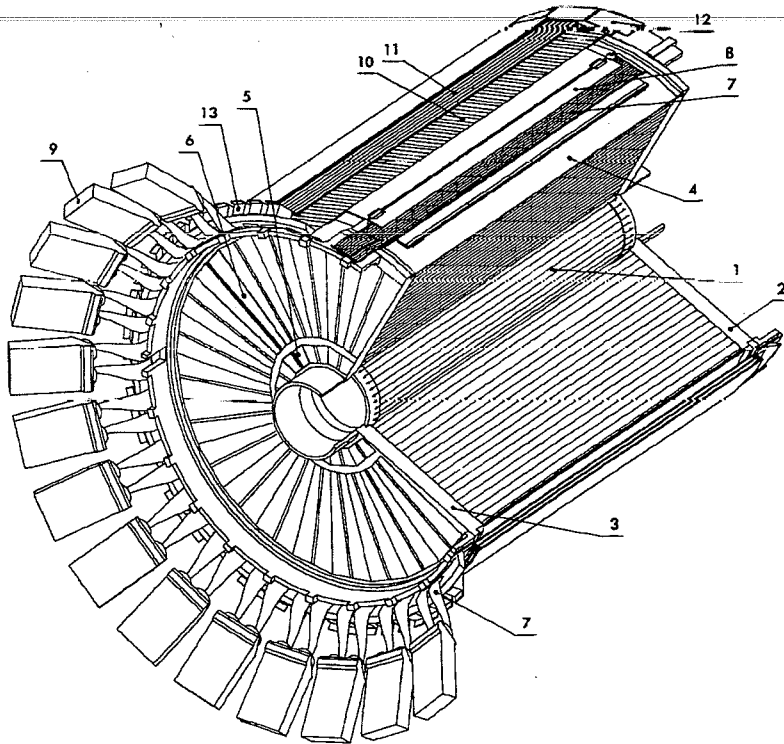


Figure 5.8: The central tracking system, consisting of TEC (1-6), PSF (7-9) and Z-Detector (10-13) [94].

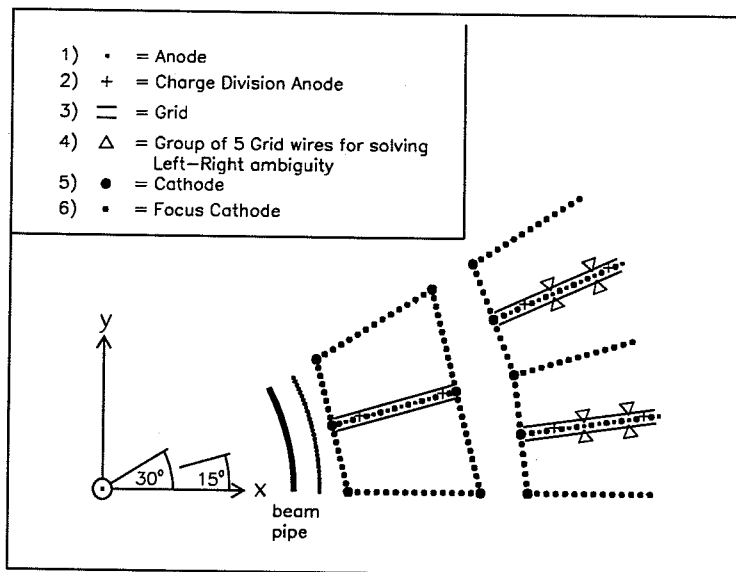


Figure 5.9: The wire configuration in one inner and in part of two outer TEC sectors.

electric field, a stability better than 0.5 V/cm is maintained. All HV units are operated in the trip mode.

In the $r-\varphi$ plane the track coordinates are measured with a maximum of 62 anodes, 8 in the inner chamber and 54 in the outer. The first spatial coordinate is measured at a distance of 110 mm from the beam line and the last one at a distance of 427 mm. The anodes are divided into three groups:

Standard anodes are read out only at one end and optimized for a high precision $r-\varphi$ measurement.

Charge division anodes are read out at both ends, measuring the charge of the signals and thus determining the track coordinate along the wire in addition to the $r-\varphi$ measurement. Two out of eight anodes in an inner sector and 9 out of 54 in an outer sector are equipped with a charge division readout.

Left-Right ambiguity anodes perform an $r-\varphi$ measurement with left-right ambiguity resolved. On each side of such an anode, a group of five grid wires is isolated from the rest of the grid and connected to preamplifiers via capacitors. The signals are then fed into a differential amplifier, with an output signal, corresponding to the space asymmetry of the avalanche at the anode, used to determine the side of the incoming drift electrons. In each outer TEC sector 14 out of 54 anodes are equipped with this type of readout.

The pulses induced on the anodes are digitized by 100 MHz flash analog-to-digital converters (FADCs). The FADC allows the determination of the center-of-gravity of the pulse, which results in the very precise drift-time measurement. Furthermore, a good multihit resolution is obtained by appropriate pulse shaping and applying a cluster finding algorithm to the FADC data. The 1968 readout channels of TEC produce about 2 Mbytes of raw data per event. This large amount of information must be significantly reduced before transferring it to the L3 DAQ. Therefore a fast data reduction processor (DRP) is attached to the output of each pair of FADCs.

The combined value for the single wire intrinsic efficiency and the probability to be used in the track reconstruction is found to be 93% for the $r-\varphi$ measurement and 78% for the z -measurement (using charge division wires). The single wire resolution is obtained from the width of the residuals distribution of the hits used to fit a track. In the detection region between the anode and grid planes, where TEC behaves like a conventional drift chamber, the resolution is of the order of 250 μm . For the tracks in the drift region, the averaged over the sector resolution is approximately 50 μm for the outer TEC and 60 μm for the inner TEC. The difference between the two chambers is due to the larger ratio of drift to amplification region in the inner compare to the outer chamber. For the double track resolution, the value of 650 μm is obtained. The

average resolution of the transverse momentum, $\sigma(1/p_t)$, has been found to be 0.018 GeV^{-1} . The resolution of the misdistance of two TEC tracks in the $r - \varphi$ plane is measured using Bhabha and dimuon events and is $120 \mu\text{m}$.

The PSF system is designed to calibrate offline the drift velocity of the TEC and consists of 24 plastic scintillating fiber ribbons placed just outside and in correspondence with the outer sectors of the TEC. Each ribbon is made of 143 optically isolated fibers with a cross section of $0.7 \times 1.0 \text{ mm}^2$ and 1.3 m long. A detailed description of the PSF readout system can be found in [96]. A complete study of the PSF performance is presented in [97].

The Z-detector [95] supplements the precise $r - \varphi$ measurement from the TEC with a z -coordinate for charged particles in the angular range $42^\circ < \theta < 138^\circ$. It consists of two concentric cylindrical proportional wire chambers with cathode strip readout. The wires are strung in axial direction. The cathodes are made out of a $35 \mu\text{m}$ thin copper layer glued onto the Kapton foil with the strips in the forms of a helix and ring. This configuration provides a precise measurement of the coordinate along the wire by measuring the induced charges on the strips. The strips are readout by an electronics chain consisting of preamplifiers, line-drivers and charge-to-digital converters (QTC). Both chambers are operated at 1600 V. With a gas mixture of 80% argon and 20% carbon dioxide, a gas amplification of 5×10^4 is obtained. The long term stability of the gas gain is monitored by a built-in Fe^{55} source. Measured from the data, the intrinsic resolution of the chamber equals $320 \mu\text{m}$ at $\theta=90^\circ$. A single chamber efficiency is above 96%.

5.2.8 Luminosity Monitor

The luminosity monitor consists of two finely segmented BGO electromagnetic calorimeters with two sets of proportional wire chambers in front of them, situated symmetrically on either side of the interaction point and covering $25 \text{ mrad} < \theta(\pi - \theta) < 70 \text{ mrad}$ polar angle range. Each calorimeter is an azimuthally symmetric array of 304 BGO crystals of the same shape and dimensions, used in the barrel electromagnetic calorimeter. Every crystal is readout by a photodiode and has a LED to monitor its stability.

The luminosity monitor is used to select low angle Bhabha events and to measure the angles of the scattered electrons and positrons. At low angles the cross section for this process is large and is dominated by t -channel photon exchange. Comparison of the measured rate to the theoretical calculation of the cross section provides a measurement of the luminosity.

5.2.9 Data Acquisition System and Trigger

The data acquisition system (DAQ) of the L3 experiment [98] is designed to combine the digitized data of all subdetectors into one single event record for the subsequent online monitoring and offline physics analysis and it is built on the FASTBUS standard [99]. The DAQ consists of four parallel data streams from TEC, BGO, HCAL and the Muon Chambers and a separate stream of trigger data.

On a positive level-1 trigger decision each subdetector data are combined into a single output memory by a subdetector Event Builder. In case of a positive level-2 trigger decision the central *Event Builder* combines all subdetectors and trigger data into a single event which is dispatched to the memory of one of the level-3 trigger processors. On a positive result of level-3 trigger analysis, the event is acquired by the main online computer and stored on tape.

Repetitive tasks at each horizontal layer lead to a modular structure, which is implemented with a few identical hardware elements, such as source and destination memories, a data moving device and an intelligent controller to steer the data flow. To buffer the data coming from the subdetector readout electronics LeCroy 1892 memory modules are used. Data are fed into the memory via differential ECL-lines at a speed of 16 Mbytes/s and can be simultaneously read out via the FASTBUS backplane. Data assembled from several of these memories are moved to a destination buffer, which, in turn, becomes the data source for the next step of event building. A Dual Slave Memory (DSM) [100] is used as the buffer. It can be addressed both on the FASTBUS cable (destination) and the backplane (source) segments. The transfer rate between the LeCroy 1892 memory and the DSM is 11.4 Mbytes/s in the block transfer mode. Data moving is performed by a dual ported device called the Block Mover (BM) [101]. The BM reads the data on one segment and writes them on another segment adding only 50 ns to the access time of the slowest memory. The controlling device is a General Purpose Master (GPM) [102], which has full FASTBUS master capabilities and based on the Motorola 68000. The GPM requires about 1.25 ms to extract information from each source memory. The BM and GPM form an Event Builder at subdetector level. For the Central Event Builder and as active element for the interfacing between the FASTBUS system and the online computer a CHI processor (CERN Host Interface) [103] is used. The data can be transferred over this interface at a maximum speed of up to 3 Mbytes/s.

The average event size is about 40 kbytes and the DAQ system is capable of handling a total level-1 trigger rate of 100 Hz with a dead time of 5%.

The L3 trigger system consists of three sequential levels and is designed to select with high efficiency and redundancy events occurred in genuine e^+e^- interactions and to reject all possible backgrounds such as beam-gas and beam-wall interactions, cosmic ray muons, uranium noise in the HCAL, coherent electronic noise in the BGO, etc.

Level-1 Trigger

After each beam crossing, every $22.2 \mu\text{s}$ in four-bunch and every $11.1 \mu\text{s}$ in eight-bunch mode of LEP operation, all L3 detector components are read out by the front-end electronics. In a few μs after that each L3 subdetector provides the Level-1 trigger with analog or fast digitized trigger data to make a decision either to initiate the digitization or clear the front-end electronics before the next beam crossing. The Level-1 trigger consists of four independent triggers generated by *Muon Chambers*, *Scintillator*, *TEC* and *Energy* triggers. If any of them gives a positive decision the data are digitized and stored within $500 \mu\text{s}$ in a multievent buffer. The Level-1 trigger typically reduces 45 kHz (90 kHz) beam crossing rate to 10 Hz.

The *energy trigger* [104] is a large processor farm, consisting of 350 specialized CAMAC modules which digitizes the analog signals, performs necessary computations and makes decision based on the value and the topology of the energy deposition in the BGO, HCAL and Luminosity monitors (Figure 5.10).

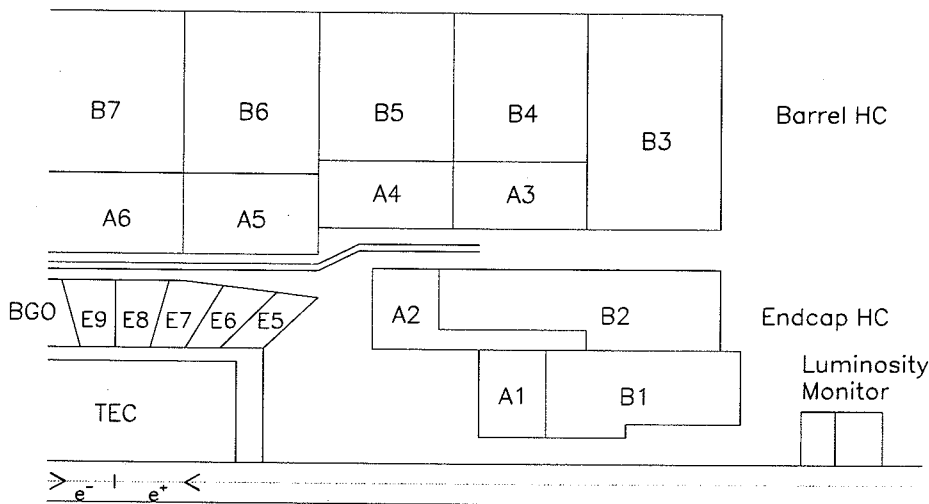


Figure 5.10: Energy trigger segmentation in the $r - \theta$ plane. Elements of the BGO endcaps are not shown.

For that purpose, the BGO barrel supplies 256 analog signals, each corresponding to 30 crystals grouped together, with 32 azimuthal and 8 polar segments. Each BGO endcap provides 128 trigger signals with 32 azimuthal and 4 polar segments. The azimuthal segmentation has been kept constant, resulting for the endcaps in nonuniform

grouping in θ and φ . For trigger purposes each HCAL barrel module is subdivided into an inner layer, called part A, one interaction length thick, and the remaining part, called part B, resulting in a uniform trigger segmentation in φ with a range of 22.5° . Each HCAL endcap ring is subdivided into 16 azimuthal segments and two layers. In total, part A has 16 " φ " and 11 " θ " segments, part B has 16 " φ " and 13 " θ " segments. Each calorimeter of the luminosity monitor provides 16 signals to the energy trigger, corresponding to a uniform φ segmentation of 22.5° . In total, the energy trigger processes 928 signals and has several different trigger conditions:

- A *total energy* subtrigger accepts events with the sum of the electromagnetic energy above 8 GeV, or the total calorimetric energy in excess of 15 GeV summed over segments, which are farther than 18° from the beam pipe. For the region below 18° , which is subject to LEP background, the threshold value is 25 GeV.
- A *cluster* is defined as localized energy deposit in the BGO and HCAL layer(s) at the same θ and φ coordinates with a threshold of 6 GeV for the BGO and 7 GeV for the HCAL. With an additional requirement of coincidence of the TEC trigger at the same azimuth, thresholds are reduced to 2.5 and 3 GeV.
- A *single photon* subtrigger requires a *cluster* of at least 0.9 GeV in the BGO barrel which must account for at least 80% of the total electromagnetic energy.
- *Multiplicity* is the number of any trigger elements with an energy above a threshold, which depends on the calorimeter type and the polar angle.
- A *luminosity trigger* requires energy deposition in the luminosity monitor which has *back to back* segments each above 15 GeV on both sides, or one segment is greater than 25 GeV and the other is greater than 15 GeV (*double tag*), or either side has greater than 30 GeV (*single tag*).

The *TEC trigger* [105] processes analog signals from 14 left-right ambiguity anode wires in each of the 24 outer TEC sectors and searches for tracks in the plane transverse to the beam axis. It assigns the signals in a given sector to one or more of four φ subsectors, depending on the drift time and information from the grid wires, and performs pattern search for tracks originating from the beam line. The trigger decision is based on the total number of tracks, the number of coplanar pairs of tracks with maximum acoplanarity of 105° , or the number of track clusters with back to back topology. The data from all sectors are processed in parallel and to make the trigger decision takes less than $1 \mu\text{s}$. The θ acceptance of this trigger is limited by $28^\circ \leq \theta \leq 162^\circ$. The threshold of p_t value of tracks varies from 100 MeV to 600 MeV.

For the *muon trigger* [106], all signal wires of the muon spectrometer are grouped into "trigger cells" which, for the P-chambers, coincide with the physical chambers and

consist of pairs of radially adjacent wires while, for the Z-chambers, are formed from two adjacent wires of each double plane. To trigger an event, at least two “trigger cells” should lie on one of the predefined “roads”. Each such road is parameterized by a central cell and half width in each of three layers of the muon spectrometer, and corresponds to a certain region in φ , transverse momentum and charge of a track, originated from the interaction point. All possible tracks with $p_t > 1$ GeV are predefined. The level-1 muon trigger rate is dominated by cosmic rays background, which is ~ 10 Hz, and reduced down to ~ 1 Hz by requiring any scintillator hit be within 30 ns of the beam crossing.

The *scintillator trigger* [107] is based on the signals from 30 barrel counters and makes its decision mainly on multiplicity. Its information is also used by the muon trigger to reject cosmic rays.

The redundancy of the level-1 trigger makes it possible to study offline single sub-trigger efficiencies for the different Z^0 decays. In particular, $Z^0 \rightarrow \tau^+\tau^-$ decays are triggered by the *Energy*, *TEC*, *Muon* or *Scintillator multiplicity* triggers. Detailed studies have shown that the combined trigger inefficiency for these events is $(1.0 \pm 0.5) \times 10^{-3}$ [108].

Level-2 Trigger

The second level trigger [109], based on a farm of microprogrammable fast XOP processors [110], makes use of the level-1 trigger data and second level TEC trigger data. In particular, it receives charge and drift time information from the charge division wires of the TEC, which allows to reconstruct track coordinates in three dimensions [111]. The main purpose of the second level trigger is to reduce the level-1 trigger rate by

- the detection of clustered energy in the BGO and two lateral layers of HCAL in the full $\theta - \varphi$ plane;
- the longitudinal and transverse calorimetric energy imbalance of the event;
- the reconstruction of an event vertex along the beam axis using the charge division wires of the TEC.

Level-3 Trigger

The third level trigger [112] is embedded in the main data flow of the DAQ and consists of three 3081/E emulators [113] equipped with a FASTBUS interface. Unlike the first two levels, the level-3 trigger has access to the complete digitized data with finer granularity and higher resolution. It performs data validation first, then reconstruction of the calorimetric energy, time-of-flight measured by the scintillators, partial pattern

recognition of tracks in the TEC and search for correlations between TEC tracks and calorimetrical clusters. The level-3 trigger further reduces level-1 muon trigger rate by requiring at least one scintillator hit in front of a triggered muon chamber octant to be within 10 ns of the beam crossing. Luminosity events are excluded from the reconstruction and always accepted. The final trigger decision is based on the overall event characteristic, taking first level trigger information into account as well. The level-3 trigger does not introduce any additional dead time and allows an overall event writing rate of 2 Hz.

5.2.10 Event Reconstruction

Event reconstruction in the L3 detector involves several levels. First, the digitized information from the DAQ system is read and decoded. Next, initial reconstruction is performed separately for every subdetector. Finally, associations are made between the reconstructed objects in different subdetectors to produce the kinematic variables that characterize an event. Reconstructed events are stored in several formats for the subsequent analysis. The Master Data Reconstructed Stream (MDRE) contains all the information necessary to repeat the full detector re-reconstruction in case of the availability of better calibrations. The typical size of an event in MDRE format is about 150 kbytes, compared to about 370 kbytes required for the raw data. Compressed data format, so called Data Summary Unit (DSU), contains all the essential information of an event, such as reconstructed track momenta, energies of BGO crystals and HCAL towers and scintillator timing, and is designed to be used in the physical analysis. A typical DSU event occupies about 20 kbytes.

Central tracking system

For every hit in the TEC, the raw time value given by the FADC is converted into the drift time applying anode dependent corrections. The drift distance is reconstructed from the drift time using a drift-distance-time relation, obtained from the TEC calibration. A pattern recognition algorithm is then applied to the hits, to find the tracks of charged particles. For every found track, the fit is performed to determine the curvature, the distance of the closest approach (DCA) and the azimuthal angle at a given reference point. At this stage of reconstruction each track has a mirror track. Information from left-right ambiguity anodes and the continuity between inner and outer TEC chambers allow to resolve the "true" tracks. Finally, charge division wires and matched Z-detector hits are used to refit each track to a helix in three dimensions.

BGO electromagnetic calorimeter

Energies of fired crystals in the BGO electromagnetic calorimeter are determined from the ADC counts by subtracting the pedestals and applying calibration constants. Energy is corrected for temperature variations and Xenon lamp monitor data. Then, a group of neighboring crystals with a local maxima of energy deposition and with total energy greater than 40 MeV form a bump. The neighbors are defined as crystals having a common corner or edge. Crystals that are equally close to more than one bump get assigned to the most energetic one. The energy of the bump is determined from the energies of crystals in a 3×3 matrix, centered on the most energetic one (local maxima), applying leakage and impact point dependent corrections and assuming electromagnetic origin of the bump. The impact point of the particle is calculated from the energy weighted center of gravity of the 3×3 matrix, again assuming electromagnetic origin of the particle. The electromagnetic quality of the bump is defined by χ_{BGO}^2 , which compares the fraction of total energy deposited in the crystals in a 3×3 matrix with the expectation from the test beam results.

Hadron calorimeter

Readout towers in the HCAL with energy over 9 MeV represent "hits". Two or more adjacent or contiguous hits form a cluster. Two hits touching at their corners or being separated by a tower, but lying on the same radial vector from the interaction point may form or be a part of a cluster. This definition of a cluster strongly discriminates between particle tracks or cascades and random background, while accommodating fluctuations in the cascade process as well as possible inefficiencies in the detector coverage. Each cluster is characterized by its total energy and geometric position. A cluster's transverse and longitudinal profiles allow to discriminate between muon clusters, which essentially define a minimum ionizing "track" through the calorimeter, and hadrons. Clusters due to electrons have a high ionization density because of the short radiation length of uranium.

Muon spectrometer

Reconstructed space points from ionizing particles traversing the muon chambers are grouped into segments in each layer of the muon spectrometer. A track is formed if at least two segments in P-chambers can be associated with common origin. Every found track is fitted to a helix, providing the momentum and the charge of the particle. An average energy loss of the track in the material is then calculated via backtracking to the interaction region, assuming that it is a minimum ionizing particle (mip). The momentum at the interaction region is determined from the estimated energy loss and the momentum measured in the spectrometer.

Reconstruction across L3

The reconstructed objects in the different subdetectors, such as tracks in the TEC and the muon spectrometer, bumps in the BGO calorimeter, clusters in the HCAL and hits in the scintillator counters and the muon filter, are grouped together to form jets and to reconstruct separate particles. Thus, a track in the muon spectrometer is associated with clusters in the HCAL, a bump in the BGO electromagnetic calorimeter and a track in the TEC, and identified as “muon” candidate, called AMUI. From the remaining bumps in the BGO calorimeter and clusters in the HCAL “smallest resolvable clusters”, called SRC’s, are then constructed, each of which roughly corresponds to one final state particle. A rough energy calibration is then applied to determine a 3-momentum vector for each resolved SRC, with the magnitude given by the total energy and the direction determined by an energy-weighted average of the positions of its components. An iterative procedure is then applied to the SRC’s and AMUI’s to combine them into the jets, which are contained in a cone of typical half-angle size 30° .

An event thrust axis is then calculated from the AMUI’s and SRC’s as the unit vector \vec{n}_T maximizing the following sum

$$\sum_i |\vec{p}_i \cdot \vec{n}_T|$$

where \vec{p}_i is the 3-momentum of the i -th AMUI or SRC in the event. The total visible energy in the event is given by the sum of all SRC’s energies and AMUI’s momenta.

5.2.11 Detector Simulation

Any precision measurement requires detailed understanding of the detector response to the processes under study. Detector simulation plays an important role in analyzing the detector resolution, calculating efficiency and background rates, and estimating systematic effects.

The Monte Carlo event simulation proceeds in three steps. First, an event generator is used to generate a physical process of interest with all final state particles, described by their four-momenta. The generated events are then propagated through a detailed representation of the L3 detector, which includes the effects of experimental resolution, energy losses, multiple scattering, physical interactions and decays in the detector materials [114]. The result of this simulation is the digitized response of active elements of the detector, which is then fed to the same off-line reconstruction program used for the reconstruction of the real data. Possible discrepancies between data and Monte Carlo for well understood physics processes can reveal deficiencies in the modeling of the detector response, which usually are the result of the underestimation of resolution and detector inefficiency. Such discrepancies could be corrected afterwards, comparing relevant distributions for the Monte Carlo and data.

Chapter 6

Data Analysis

The selection of $Z^0 \rightarrow \tau^+\tau^- \rightarrow AB$ decay candidates proceeds in three steps. Firstly, a sample of dilepton events, which includes $Z^0 \rightarrow e^+e^-$, $Z^0 \rightarrow \mu^+\mu^-$ and $Z^0 \rightarrow \tau^+\tau^-$ decays is preselected. The preselection removes most of the background from the cosmic ray, beam-gas interactions, hadronic Z^0 decays and two-photon processes [115]. Every remaining event is then divided into two hemispheres by a plane perpendicular to the event thrust axis, and the particle identification algorithm is applied independently in each hemisphere in order to classify the τ decay mode. The particle identification of one-prong τ decays is based on the topological properties of the energy deposition in the electromagnetic and hadron calorimeters with respect to the charged particle track and is found to be relatively independent of the energy of the τ decay products [115, 116]. At this stage, a sample consists of events for which at least one of the hemispheres is identified as one the following τ decay channels: $\tau \rightarrow e\bar{\nu}\nu$, $\tau \rightarrow \mu\bar{\nu}\nu$, $\tau \rightarrow \pi\nu$ and $\tau \rightarrow \rho\nu$. Finally, in order to suppress remaining non- τ background, if both hemispheres are identified as any of these four channels, correlated cuts are applied on both sides of the event, otherwise requirements are placed only on the hemisphere opposite to the τ decay candidate.

This chapter contains descriptions of the dilepton sample preselection, the particle identification algorithm and the final selection of the following exclusive channels $Z^0 \rightarrow \tau^+\tau^- \rightarrow ee$, $e\mu$, $e\pi$, $e\rho$, eX , $\mu\mu$, $\mu\pi$, $\mu\rho$, μX , $\pi\pi$, $\pi\rho$, πX , $\rho\rho$, ρX , where X designates τ decay not identified as e , μ , π and ρ . The energy measurement and resolution for muons, electrons (photons) and charged pions are described at the end of the chapter.

6.1 Dilepton Preselection

The $Z^0 \rightarrow l^+l^-$ decays are characterized by low particle multiplicity and back-to-back topology. In the $Z^0 \rightarrow \tau^+\tau^-$ decay, in particular, the τ decay products are highly

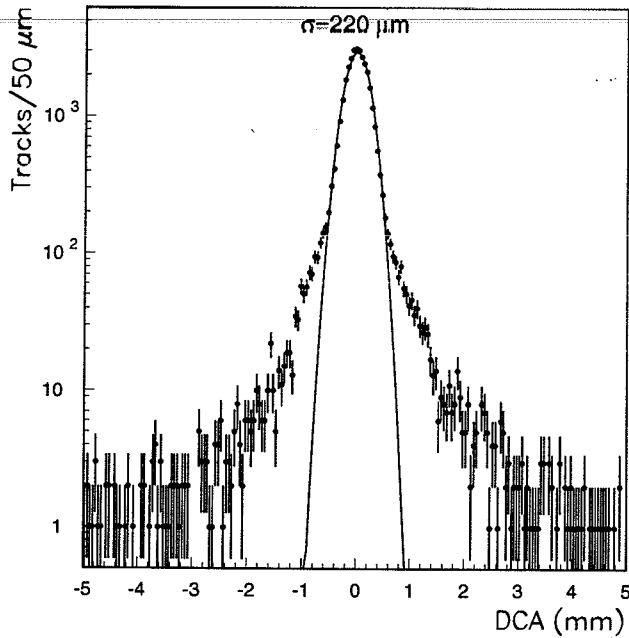


Figure 6.1: The distance of closest approach (DCA) of tracks to the nominal beam axis as measured by the TEC. The tracks are from $Z^0 \rightarrow \mu^+\mu^-(\gamma)$ events with two entries per event. The solid line is the result of a gaussian fit to the central part of this distribution.

collimated as a result of the large boost of the τ itself. Hadronic Z^0 decays, on the other hand, produce large charged track multiplicity and are removed by requiring:

- the total number of tracks in the TEC to be less than 9;
- the number of TEC tracks in any hemisphere to be less than 6;
- in each hemisphere, the difference in φ angle between any TEC track and the thrust axis to be less than 30° ;
- the total number of clusters reconstructed in the electromagnetic BGO calorimeter to be less than 20.

It is estimated from the Monte Carlo study that these cuts reject 99.9% of hadronic Z^0 decays and less than 2% of the $Z^0 \rightarrow l^+l^-$ decays.

Beam-gas interaction and cosmic ray events are reduced by requiring:

- at least two tracks to be reconstructed in the TEC;
- at least one TEC track to pass within 5 mm of the interaction region in the plane perpendicular to the beam axis;

- muon chamber tracks to have a matched scintillator hit within 5 ns of the beam crossing time.

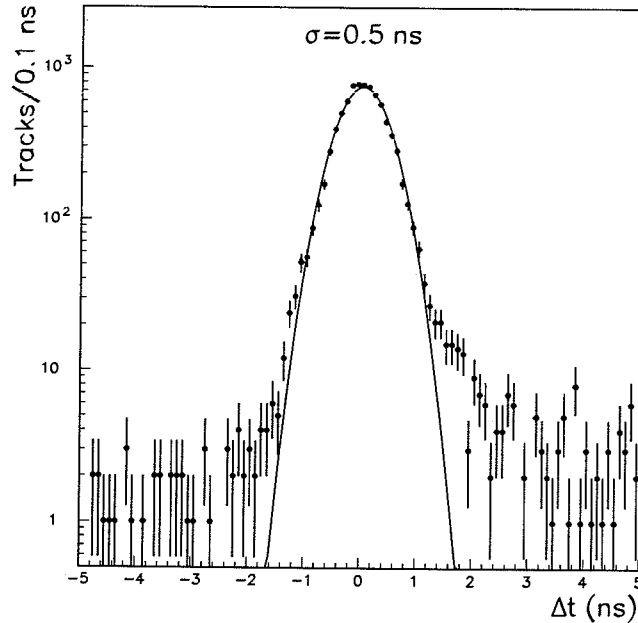


Figure 6.2: Scintillator time-of-flight distribution for the same sample used for Figure 6.1. The solid line is the result of a gaussian fit to the central part of this distribution.

Two-photon interactions $e^+e^- \rightarrow e^+e^-f\bar{f}$ are characterized by a low scattering angle of the incoming electron and positron, which remain undetected and carry out a large fraction of the incident energy. The center-of-mass of the produced $f\bar{f}$ pair tends to be boosted along the beam axis with respect to the laboratory frame, and so has low momentum transverse to the beam axis. Thus, two-photon background is suppressed by demanding:

- at least one TEC track to have a transverse momentum greater than 0.5 GeV;
- total energy to be greater than 2 GeV.

After the preselection, the data sample contains more than 98% of each of the Z^0 decays channels into charged leptons in the fiducial volume of $|\cos\theta| < 0.8$. The remaining background from cosmics and two-photon interactions is estimated to be 5%.

6.2 Particle Identification

Particle identification is carried out independently in each of the hemispheres for every event passed the preselection. It is highly desirable to minimize the use of energy dependent cuts in all phases of the particle identification, in order to avoid possible distortion of the energy spectra which are sensitive to the τ decay parameters and the τ polarization. Therefore, particle identification is based on the spatial relationship between the particle track in the TEC and characteristic profiles of the energy deposition in the electromagnetic and hadron calorimeters, expected for electrons, muons and pions. The information from the muon spectrometer is used as well.

The following signatures distinguish each of the one-prong τ decay modes considered in this analysis and form the basis for their selection:

- A $\tau \rightarrow e\bar{\nu}\nu$ decay is characterized by a track in the TEC matched to a narrow, electromagnetic shower in the BGO with little or no activity in the HCAL behind and no track in the muon chambers.
- A $\tau \rightarrow \mu\bar{\nu}\nu$ decay is identified by a track in the TEC as well as in the muon spectrometer, and a minimum ionizing trace in the BGO and HCAL. The track in the muon spectrometer should extrapolate well back to the interaction vertex.
- A $\tau \rightarrow \pi\nu$ decay has a TEC track pointing to a non-electromagnetic shower in the BGO with several clusters of energy deposition in the HCAL behind. There are no reconstructed π^0 's in the BGO. A possible track in the muon spectrometer must be consistent with punch-through.
- A $\tau \rightarrow \rho\nu$ decay is distinguished by a single charged track in the TEC, which is displaced from one or few electromagnetic showers in the BGO due to one π^0 .

Identification of the τ decays into e , π and ρ requires a TEC track to be associated with it at least three hits in the Z-Detector, providing a precise measurement of the polar angle θ of the track and a knowledge of its impact point on the BGO electromagnetic calorimeter. This confines identification of these τ decay modes to the fiducial volume $42^\circ < \theta < 138^\circ$.

6.2.1 Electromagnetic and hadronic shower profiles in the BGO

The transverse profile of the energy deposition in the BGO appears to have a characteristic form, as it is known from the test beam study, which depends only on the kind of the showering particle. This feature is due to the regular and homogeneous structure of the BGO electromagnetic calorimeter. The particle identification relies on the precise knowledge of these shower profiles in the BGO for electrons and charged pions, obtained from the Bhabha sample and the test beam data.

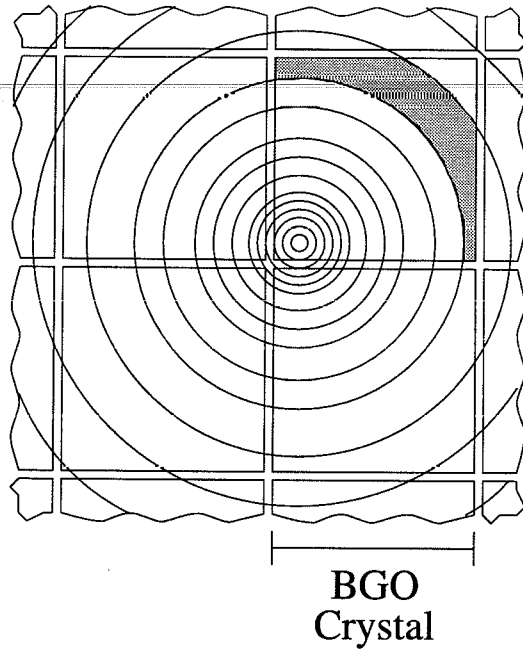


Figure 6.3: Concentric rings used for estimate of expected energy in a BGO crystal from an electromagnetic shower at the depth of one radiation length.

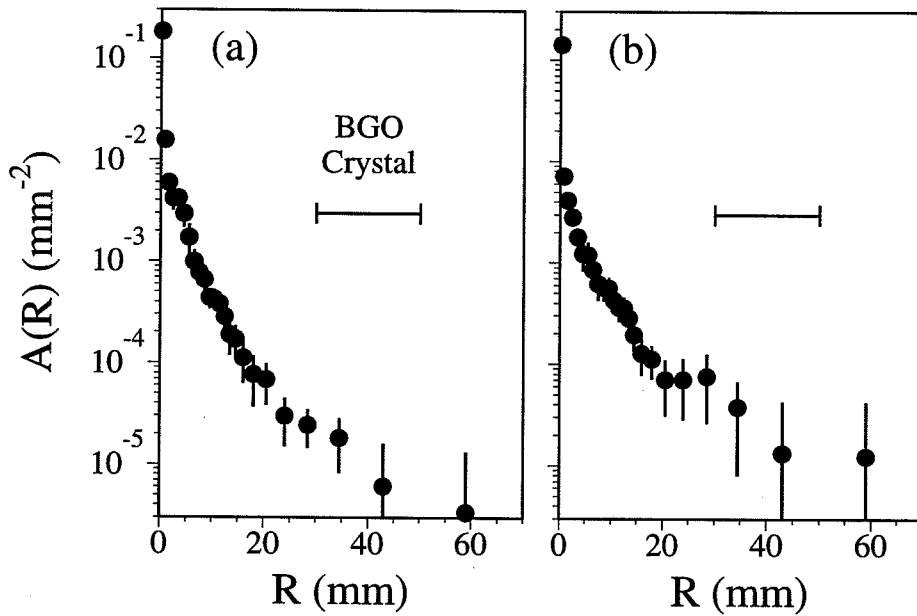


Figure 6.4: Electromagnetic (a) and hadronic (b) shower profiles in the BGO. $A(R)$ is the normalized energy density.

The transverse shower profile produced by an electron (a charged pion) is evaluated in the plane perpendicular to the track trajectory, one radiation length inside the BGO. The expected energy deposition in every crystal from a 3×3 matrix surrounding the shower maximum is computed by summing the energies in concentric annular regions contained in the crystal and centered at the impact point (see Figure 6.3):

$$Q_i = \sum_j S_j A(R_j), \quad (6.1)$$

where Q_i is the expected fractional energy in the i 'th crystal, S_j is the area of the j 'th annular region in the crystal (e.g. the shaded region on Figure 6.3), R_j is the distance from the impact point, and $A(R_j) = \frac{1}{E} \frac{dE}{dS}$ is the fractional energy density for that region, which is characteristic of the shower. The form of the energy density $A(R_j)$ gives the transverse shower profile and was found to be relatively independent of the particle energy.

An electromagnetic shower profile was obtained from a sample of Bhabha events by minimization of the following quantity

$$\chi^2 = \sum_i \sum_{j=1}^9 (E_{ij} - E_{\text{beam}} Q_{ij})^2 \quad \text{where} \quad Q_{ij} = \sum_k^{N_A} S_k A_k \quad (6.2)$$

with respect to the N_A free parameters A_k . The index i in (6.2) runs over all the electrons in the sample, E_{ij} is the measured energy in the j 'th crystal from the 3×3 matrix, and Q_{ij} is the expected normalized energy fraction.

An average hadronic shower profile was obtained from the pion test beam study using the same technique outlined above [118].

Figure 6.4 shows the resulting transverse profiles of the electromagnetic and hadronic (charged pion) showers in the BGO, used in the particle identification algorithm.

6.2.2 Electron Identification

A characteristic of the electron is a TEC track matched in both bending and non-bending directions to a narrow, electromagnetic shower in the BGO. The degree of matching is measured by comparing the φ and θ polar coordinates of the impact point given by the TEC track to the reconstructed shower maximum in the BGO: $\Delta\varphi = \varphi_{TEC} - \varphi_{BGO}$ and $\Delta\theta = \theta_{TEC} - \theta_{BGO}$. The position of the shower maximum is determined, assuming electromagnetic origin of the shower, from the center of gravity of the energy deposited in the 3×3 crystal matrix centered on the most energetic one

$$X_{\text{COG}} = \frac{\sum_{i=1}^9 E_i X_i}{\sum_{i=1}^9 E_i}, \quad (6.3)$$

where E_i and X_i are energy deposition and coordinates of the crystals, and corrected by the empiric formula (5.2), which is deduced from the test beam study [91]. The

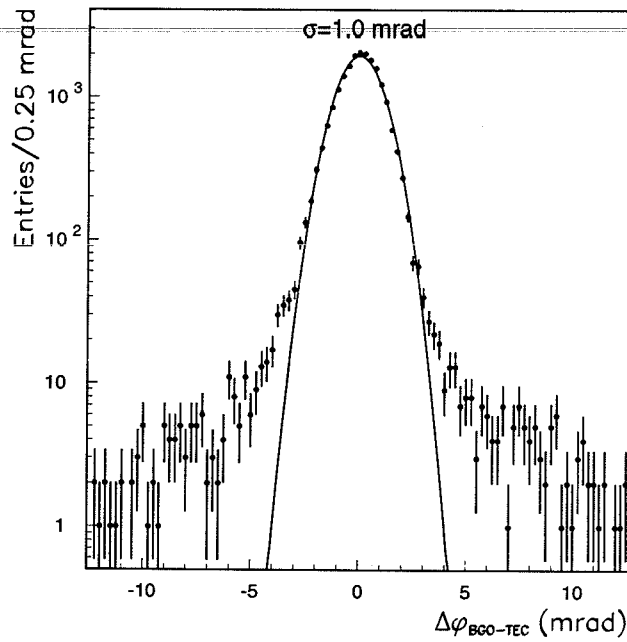


Figure 6.5: Displacement in φ between the extrapolation of the TEC track to the BGO surface and the shower maximum in the BGO for golden Bhabha events. The solid line is the result of a gaussian fit to the central part of this distribution.

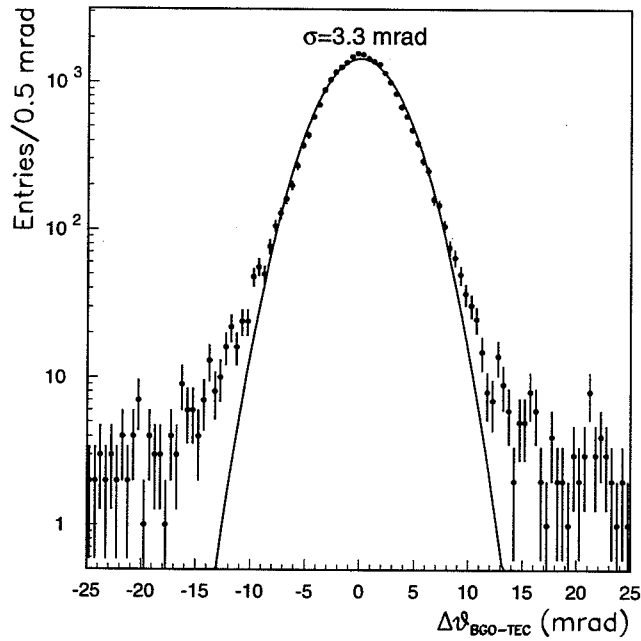


Figure 6.6: Displacement in θ between the extrapolation of the TEC track to the BGO surface and the shower maximum in the BGO for golden Bhabha events. The solid line is the result of a gaussian fit to the central part of this distribution.

$\Delta\varphi$ and $\Delta\theta$ distributions for golden Bhabha events are shown in Figures 6.5 and 6.6, where a gaussian fit gives a resolution of the detector for these quantities.

The variable χ_{em}^2 is constructed to quantify the compatibility of the observed shower profile with that expected from an electromagnetic one:

$$\chi_{em}^2 = \sum_{i=1}^9 \sum_{j=1}^9 \frac{(F_i - Q_i)(F_j - Q_j)}{V_{ij}^{-1}}, \quad (6.4)$$

where F_i is the energy fraction measured in the i 'th crystal, Q_i is the expected energy fraction there as defined in (6.1), and V_{ij}^{-1} are elements of the inverse covariance matrix, obtained from the minimization procedure described in the previous section. The sums are taken over the 3×3 crystal matrix surrounding the shower maximum.

A one-prong hemisphere is identified as an electron candidate, if the following criteria are satisfied:

1. A BGO shower, matched by a TEC track, contains at least 4 fired crystals.
2. A good space matching exists between a TEC track and a BGO shower: $|\Delta\varphi| < 11$ mrad and $|\Delta\theta| < 12$ mrad. The actual value of the cut on $|\Delta\varphi|$ depends on shower energy, varying from 11 mrad at 1 GeV to about 3 mrad at 45 GeV, reflecting the behavior of the BGO position resolution (5.3). The resolution of $\Delta\theta$ is dominated by the uncertainty of the interaction vertex position along the z -axis.
3. A BGO shower has an electromagnetic origin with $\chi_{em}^2 < 30$.
4. The probability that a track momentum measured by the TEC and a shower energy observed in the BGO arise from a single particle exceeds 0.5×10^{-4} .
5. The energy deposition in the HCAL behind the BGO shower is consistent with the tail of an electromagnetic shower and is less than 3 GeV.
6. The hemisphere does not contain a track in the muon chambers and there are not more than three additional photons in the BGO.

The identification efficiency has been found to be 83.5% in the barrel region, confined by the Z-Detector coverage. The background rate is estimated by the Monte Carlo to be less than 2% due to other τ decays.

6.2.3 Muon Identification

Muons with momenta larger than 2.5 GeV result in reconstructed tracks in the muon spectrometer. Since hadrons can also produce tracks in the spectrometer, further requirements are necessary for muon identification. The punch-through rejection can be

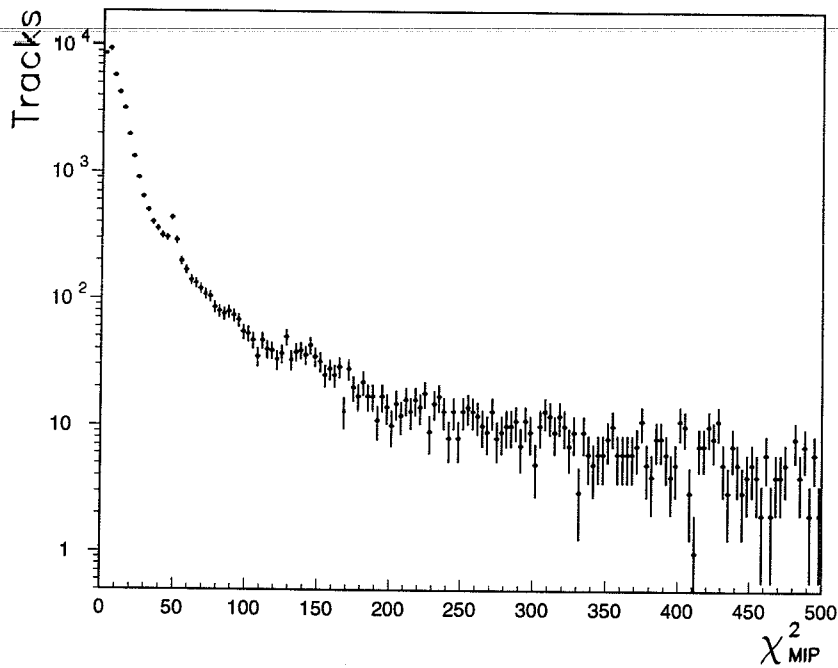


Figure 6.7: χ_{mip}^2 for muons from $Z^0 \rightarrow \mu^+ \mu^-$ decays in data. All other cuts for muon identification have been applied.

achieved by requiring that the track in the spectrometer extrapolate to the interaction region in both, bending and non-bending planes.

Also characteristic of muons is a minimum-ionizing signature in the hadron calorimeter. The compatibility of the energy deposition in the hadron calorimeter with that expected from a muon is quantified in the following way. A straight line is fit to the pattern of fired towers in the HCAL weighted by their energy. A list of proportional chambers in the calorimeter intercepted by the line is made, and the average expected energy depositions for a minimum ionizing particle (mip) are calculated for each chamber. Elements of the list are then combined to form readout towers, so that they can be compared to the pattern of measured hits. Three quantities are calculated at this comparison:

- the number of predicted hits along the line, N_{pred} ;
- the number of measured hits along the line, N_{meas} ;
- the χ_{mip}^2 of the energy depositions along the line to be due to a mip:

$$\chi_{mip}^2 = \sum_{i=1}^{N_{meas}} \left(\frac{E_i^{meas} - E_i^{mip}}{E_i^{mip}} \right)^2 \quad (6.5)$$

where E_i^{mip} are the estimated hit energies for a mip and E_i^{meas} are the measured hit energies.

Particles which are mip's tend to have a high fraction of measured hits, since they tend to follow a straight line through the calorimeters, losing their energies mostly due to ionization. It should be noted that a mip produces in each calorimeter plane a signal corresponding to about 23 MeV, which results in an average total energy loss of about 2.5 GeV. A mip also tends to have $\chi_{mip}^2 \sim 1$. In contrast, particles showering in the HCAL tend to have a lower fraction of measured hits along the straight line and values of $\chi_{mip}^2 \gg 1$.

A one-prong hemisphere is then identified as a muon, if it satisfies the following criteria:

1. There is a reconstructed track in the muon spectrometer, with at least two P-segments and one Z-segment.
2. The distance of closest approach of the extrapolated muon track to the interaction vertex is less than 500 mm in the $r - \varphi$ and $r - z$ planes for low energy muons, and less than 70 mm in the $r - \varphi$ and 200 mm in the $r - z$ plane for $p_\mu > 20$ GeV. The actual cut values depend on track momentum, following the spectrometer resolution, and vary within those limits.
3. There is only mip activity in the HCAL and:
 - a) total HCAL energy in a hemisphere is less than 10 GeV;
 - b) $\frac{N_{meas}}{N_{pred}} > 0.45$;
 - c) $\chi_{mip}^2 < 500$.
4. The energy of a BGO shower matched by a TEC track is not greater than 3 GeV. Note that the average energy loss of a mip in the BGO electromagnetic calorimeter is about 250 MeV.
5. The number of additional photons in the BGO is less than two.
6. A TEC track matches a track in the muon spectrometer within 30° in $r - \varphi$ plane at the interaction vertex.

The muon identification efficiency has been estimated from the Monte Carlo to be 95.0% in the fiducial volume of the muon spectrometer. The background rate is 1.0% due to other τ decays.

6.2.4 Photon reconstruction and π^0 identification

An algorithm for reconstructing overlapping energy clusters in the BGO, originating from one charged track and possibly several photons, has been developed to determine the number of photons and their energies [115, 116]. It incorporates information from the impact point of the charged track on the BGO and the energies of BGO crystals within the 30° half-angle cone around the track and consists from the following steps:

- 1) The TEC track is extrapolated to the BGO in order to determine the impact point on the BGO crystal, which is further called central crystal (Figure 6.8(a)).
- 2) The energy profile of the charged particle shower in the BGO is estimated by normalizing an average hadronic shower profile to the energy deposition in the central crystal. The estimated energy deposition due to the charged hadron is subtracted from the observed raw energy of each crystal in the 30° half-angle cone around the central crystal (Figure 6.8(b)).
- 3) All local maxima in the remaining BGO energy deposit become photon candidates, called neutral clusters. (Figure 6.8(c)). The energies and positions of these candidates are defined by fitting the crystal energies with electromagnetic shower profiles. Neutral clusters which fit better with the sum of two electromagnetic showers are split.
- 4) The fitted electromagnetic shower profiles from the step 3 are used to subtract the estimated energy contribution due to the photons from the observed raw crystal energies, thus obtaining a new estimate of the energy deposited in the central crystal by the charged hadron (Figure 6.8(d)).

Steps 2-4 are iterated, typically three-four times, until all reconstructed particle energies are stable to 1%. Finally, the invariant mass of each neutral cluster is calculated by fitting its transverse energy profile with the sum of two electromagnetic shower shapes, under the assumption that it may originate from the two merged photons of a π^0 decay.

After all neutral clusters in the BGO are reconstructed, π^0 candidates are identified as follows:

- a single neutral cluster forms a π^0 if the cluster energy exceeds 1 GeV, its χ_{em}^2 is less than 30 or its invariant mass is within, on average, 50 MeV of the π^0 mass, and the cluster is not closer than 9 mm to a track impact point on the BGO crystal surface;
- two separate neutral clusters form a π^0 if their invariant mass is within 30 MeV to 60 MeV of the π^0 mass, depending on the reconstructed π^0 energy.

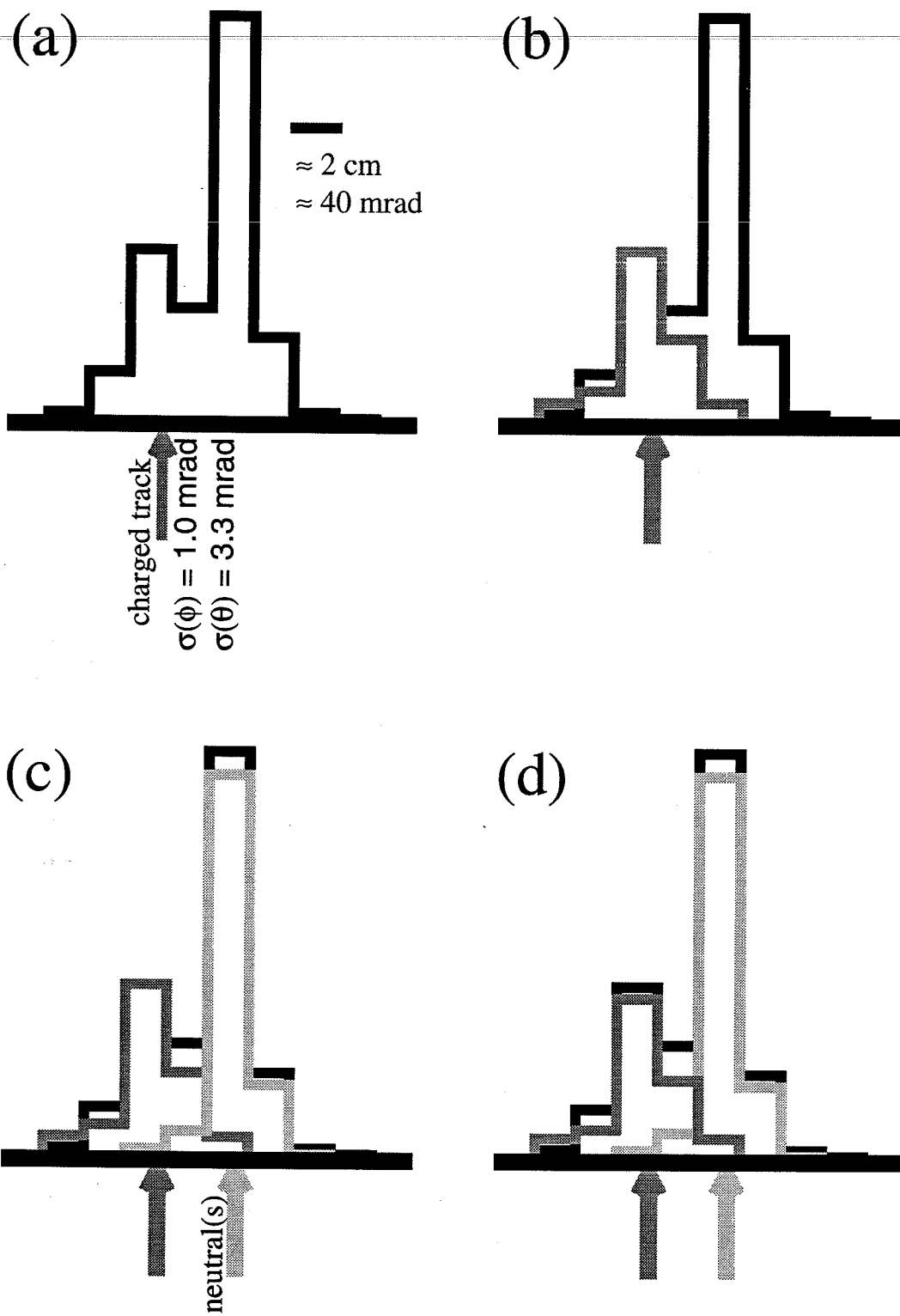


Figure 6.8: Illustration of the procedure used for neutral cluster reconstruction in the BGO.

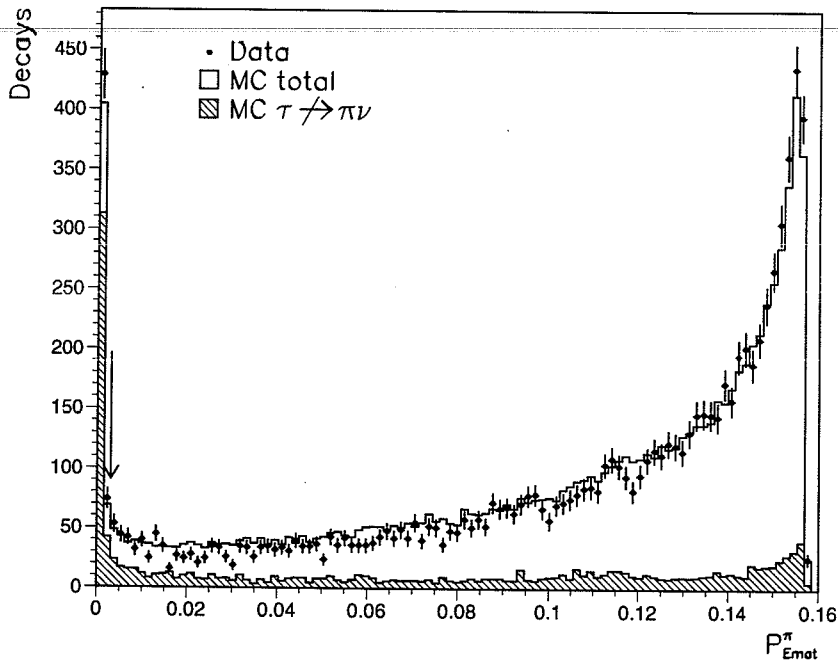


Figure 6.9: The compatibility of the TEC momentum and calorimetric energy measurements for $\tau \rightarrow \pi(K)\nu$ candidate decays after all other cuts have been applied. The arrow indicates the final cut value.

The ability to reconstruct π^0 's allows one to calculate the calorimetric energy of the charged pion. Thus, energy due to π^0 's is subtracted from the raw BGO energy in a 30° half-angle cone around the track, and the remainder along with an energy deposition in the HCAL is used to measure the calorimetric energy of a charged hadron (pion). This measurement is then combined with the independent measurement of momentum in the TEC by maximizing the likelihood for these two measurements to originate from a single hadron. This procedure improves the energy resolution for charged hadrons and determines the compatibility of these two measurements ¹.

6.2.5 Identification of $\tau \rightarrow \pi(K)\nu$ decay

A single TEC track in a hemisphere is considered as a $\tau \rightarrow \pi(K)\nu$ decay, if there is in the 30° half-angle cone around the track an energy deposition of at least 200 MeV in the BGO or 600 MeV in the HCAL. First, loose cuts are applied on the electromagnetic quality of a BGO shower, on the mip signature in the calorimeters and on the back-tracking of a track in the muon spectrometer in order to attain high efficiency for

¹This procedure is described in Section 6.4.3

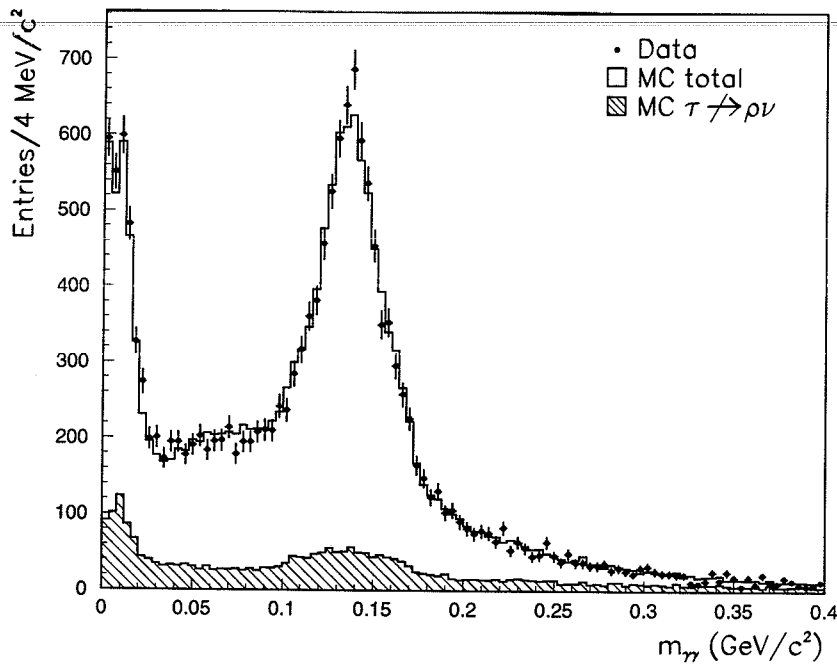


Figure 6.10: The invariant mass spectrum of two photons for selected $\tau \rightarrow \rho\nu$ decays. It comprises two cases: when both photons are reconstructed as separate neutral clusters in the BGO and when a single neutral cluster is identified as a π^0 .

electron and muon rejection.

Decays which pass these cuts are then considered to be identified as $\tau \rightarrow \pi(K)\nu$ candidates, if they satisfy the following additional criteria:

1. there is no reconstructed π^0 or photon candidate with energy greater than 0.5 GeV in the same hemisphere;
2. the probability that the momentum measured by the TEC and the calorimetric energy arise from the same charged hadron exceeds 0.3×10^{-2} (Figure 6.9);
3. there is no track in the muon chambers with momentum higher than 30 GeV;
4. the total BGO energy in the 30° half-angle cone around the track is less than 35 GeV.

Cuts 3 and 4 serve to avoid a background due to the high energy muons (dimuons) and electrons (Bhabha). No separation between charged pions and charged kaons is made. The efficiency of $\tau \rightarrow \pi(K)\nu$ identification has been estimated from the Monte Carlo to be 67.5% in the barrel. The background rate is 11.0% due to other τ decays.

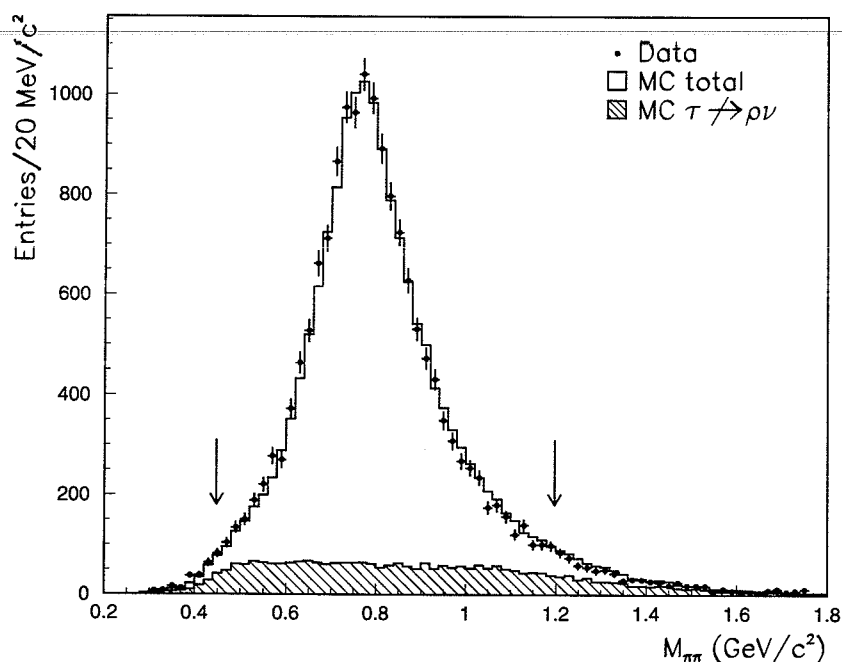


Figure 6.11: The $\pi^\pm\pi^0$ invariant mass distribution. The arrows indicate the range of $M_{\pi^\pm\pi^0}$ accepted for the $\tau \rightarrow \rho\nu$ identification.

6.2.6 Identification of $\tau \rightarrow \rho\nu$ decay

A single TEC track in a hemisphere is identified as a $\tau \rightarrow \rho\nu$ candidate, if the following criteria are satisfied:

1. there is exactly one π^0 candidate in the same hemisphere (Figure 6.10);
2. the probability that the calorimetric energy assigned to the charged hadron and the momentum measured by the TEC originates from the same particle exceeds 1.0×10^{-3} ;
3. the π^0 and the charged hadron have an invariant mass between 0.45 and 1.2 GeV (Figure 6.11);
4. the reconstructed ρ energy is greater than 5 GeV;
5. there is no track in the muon spectrometer with momentum higher than 30 GeV;
6. the total BGO energy in the 30° half-angle cone around the track is less than 44 GeV.

Cut 4 uses an advantage of the high Lorentz boost of the ρ 's in the laboratory system, see (4.19). Cuts 5 and 6 serve to avoid a background due to the high energy muons (dimuons) and electrons (Bhabha). The efficiency of the $\tau \rightarrow \rho\nu$ identification has been estimated from the Monte Carlo to be 61.5% in the barrel. The background rate is 13.0% due to other τ decays.

The fraction of identified $\tau \rightarrow \rho\nu$ decays in which both photons from π^0 decay are reconstructed as one neutral cluster (two separate neutral clusters) in the BGO is 77.9% (22.1%) in the data. These fractions in the Monte Carlo are 76.5% and 23.5%, respectively. Due to the different energy resolution and acceptance for charged pion and π^0 in these two cases, the Monte Carlo distributions are reweighted in order to reproduce their fractions as in the data.

6.3 Event Selection

The final event selection starts after the particle identification is done independently in both hemispheres of the event. The aim is to suppress remaining non- τ background, such as dimuon and Bhabha events, residual two-photon and cosmic ray events. If both hemispheres of the event are identified as one of the following one-prong τ decay channels: $\tau \rightarrow e\bar{\nu}\nu$, $\tau \rightarrow \mu\bar{\nu}\nu$, $\tau \rightarrow \pi\nu$ and $\tau \rightarrow \rho\nu$, then correlated cuts are applied on both sides of the event. If only one hemisphere of the event is identified, additional requirements are placed only on the hemisphere opposite to the τ decay candidate. Events with no identified hemispheres are rejected.

This section describes a selection of the following exclusive channels $Z^0 \rightarrow \tau^+\tau^- \rightarrow ee, e\mu, e\pi, e\rho, eX, \mu\mu, \mu\pi, \mu\rho, \mu X, \pi\pi, \pi\rho, \pi X, \rho\rho, \rho X$, where X designates a τ decay not identified as e, μ , π or ρ . Due to the quite different resolution of the muon momentum measurement, the selection procedure distinguishes between identified $\tau \rightarrow \mu\bar{\nu}\nu$ decays, where muons traverse at least three layers of the muon spectrometer ("triplets") and only two layers of the muon spectrometer ("doublets"). Identified $\tau \rightarrow \mu\bar{\nu}\nu$ decays with "doublets" are not considered explicitly and counted as X.

$$Z^0 \rightarrow \tau^+\tau^- \rightarrow (e\nu\nu)(e\nu\nu)$$

In order to insure good containment of the electromagnetic energy in an event, both identified electrons are required to have their reconstructed shower maxima in the BGO to be one crystal away from the gap, i.e. $|\cos\theta| < 0.71$. Radiative Bhabha events and two-photon processes are rejected by cutting on the acollinearity, which should be less than 20° . In addition, the total electromagnetic energy should be less than $0.8\sqrt{s}$. Events with total electromagnetic energy less than $0.15\sqrt{s}$ are required to have the difference in the transverse energies of the electrons to be greater than 1 GeV.

$$Z^0 \rightarrow \tau^+\tau^- \rightarrow (e\nu\nu)(\mu\nu\nu)$$

Remaining background due to the two-photon processes is suppressed by cutting on the acollinearity, which should be less than 20° , and requiring at least one TEC track with $p_t > 3$ GeV. A scintillator hit, associated with a muon, should be within 2 ns of the beam crossing time. Both tracks in the TEC have $|DCA| < 3$ mm. An event selected for this channel is shown on Figure 6.12.

$$Z^0 \rightarrow \tau^+\tau^- \rightarrow (e\nu\nu)(\pi\nu)$$

Both particles are confined to the fiducial volume $|\cos\theta| < 0.71$. The number of dead BGO crystals in the vicinity of the impact point of any TEC track should not exceed one. For events with the electron having energy greater than $0.85 E_{\text{beam}}$, the charged pion should have at least 5 GeV of energy deposition further than the first three HCAL layers (18 X_0). At least one TEC track must have $p_t > 3$ GeV.

$$Z^0 \rightarrow \tau^+\tau^- \rightarrow (e\nu\nu)(\rho\nu)$$

Both particles are confined to the fiducial volume $|\cos\theta| < 0.71$. The number of dead BGO crystals in the vicinity of the impact point of any TEC track should not exceed one. For events with the electron having energy greater than $0.85 E_{\text{beam}}$, the charged pion from $\tau \rightarrow \rho\nu$ decay should have at least 1.5 GeV of energy deposition further than the first three HCAL layers.

$$Z^0 \rightarrow \tau^+\tau^- \rightarrow (e\nu\nu)X$$

The event hemisphere, opposite to the identified electron candidate, should be inconsistent with an electron signature, in order to suppress the predominant Bhabha background. Therefore, in the case of only one TEC track in the recoil hemisphere, there is a reconstructed track in the muon chambers, or a shower development in the HCAL, which is due to a mip or a hadron, and a matched bump in the BGO inconsistent of being electromagnetic. The electromagnetic energy in the recoil hemisphere should be less than $0.8 E_{\text{beam}}$. The event is rejected if the electromagnetic energy in the recoil hemisphere cannot be reliably measured due to dead crystals or cracks in the vicinity of the impact point of the TEC track. Two-photon background is rejected by the requirement that the total electromagnetic energy be greater than $0.1\sqrt{s}$ or at least one TEC track have $p_t > 4$ GeV.

$$Z^0 \rightarrow \tau^+\tau^- \rightarrow (\mu\nu\nu)(\mu\nu\nu)$$

Radiative dimuon and $\gamma\gamma$ events are rejected by cutting on the acollinearity, which should be less than 15° . Events containing a photon with energy greater than 3 GeV

are rejected. In order to suppress cosmic rays, TEC tracks are required to satisfy the following cut on their DCA's: $|DCA_1| + |DCA_2| < 3$ mm. Scintillator hits, associated with muons, should be within 2 ns of the beam crossing time. In this case, $p_{\mu 1} + p_{\mu 2} < 0.8 \sqrt{s}$ and $\max(p_{\mu 1}, p_{\mu 2}) < 0.9 E_{\text{beam}}$. Events with $p_{\mu 1} + p_{\mu 2} < 0.15 \sqrt{s}$ are required to have the difference in their p_t , as measured by the TEC, to be greater than 1 GeV, in order to reject any remaining two-photon events.

$$Z^0 \rightarrow \tau^+ \tau^- \rightarrow (\mu\nu\nu)(\pi\nu)$$

A scintillator hit, associated with a muon, should be within 2 ns of the beam crossing time. TEC tracks are required to satisfy the following cut on their DCA's: $|DCA_1| + |DCA_2| < 3$ mm. A pion candidate should not point into the cracks between the HCAL modules. At least one TEC track must have $p_t > 3$ GeV.

$$Z^0 \rightarrow \tau^+ \tau^- \rightarrow (\mu\nu\nu)(\rho\nu)$$

A scintillator hit, associated with a muon, should be within 2 ns of the beam crossing time. TEC tracks are required to satisfy the following cut on their DCA's: $|DCA_1| + |DCA_2| < 3$ mm. Events containing a muon candidate with a momentum greater than $0.85 E_{\text{beam}}$ and a mip signature in the HCAL in the opposite hemisphere are rejected.

$$Z^0 \rightarrow \tau^+ \tau^- \rightarrow (\mu\nu\nu)X$$

The event hemisphere opposite to the identified muon candidate should be inconsistent with a muon signature, in order to suppress the predominant dimuon background. Therefore, in the case of only one TEC track in the recoil hemisphere, an energy deposition in the BGO and HCAL should differ from the typical mip trace. If there is a track in the muon spectrometer on the recoil side, its momentum must be less than $0.8 E_{\text{beam}}$. Two-photon background is rejected by the requirement that at least one TEC track has $p_t > 3$ GeV or, in the case of two tracks in the TEC, the difference in their p_t must be greater than 1 GeV. A scintillator hit, associated with an identified muon, should be within 2 ns of the beam crossing time. A TEC track, which is due to an identified muon, must have $|DCA| < 2$ mm.

$$Z^0 \rightarrow \tau^+ \tau^- \rightarrow (\pi\nu)(\pi\nu)$$

The number of dead BGO crystals in the vicinity of the impact point of any TEC track should not exceed one. In order to reject residual two-photon background, it is required that at least one TEC track have $p_t > 4$ GeV.

$$Z^0 \rightarrow \tau^+ \tau^- \rightarrow (\pi\nu)(\rho\nu)$$

Residual two-photon background is rejected by cutting on the acollinearity, which should be less than 20° . An event selected for this channel is shown on Figure 6.13.

Run # 450102 Event # 867

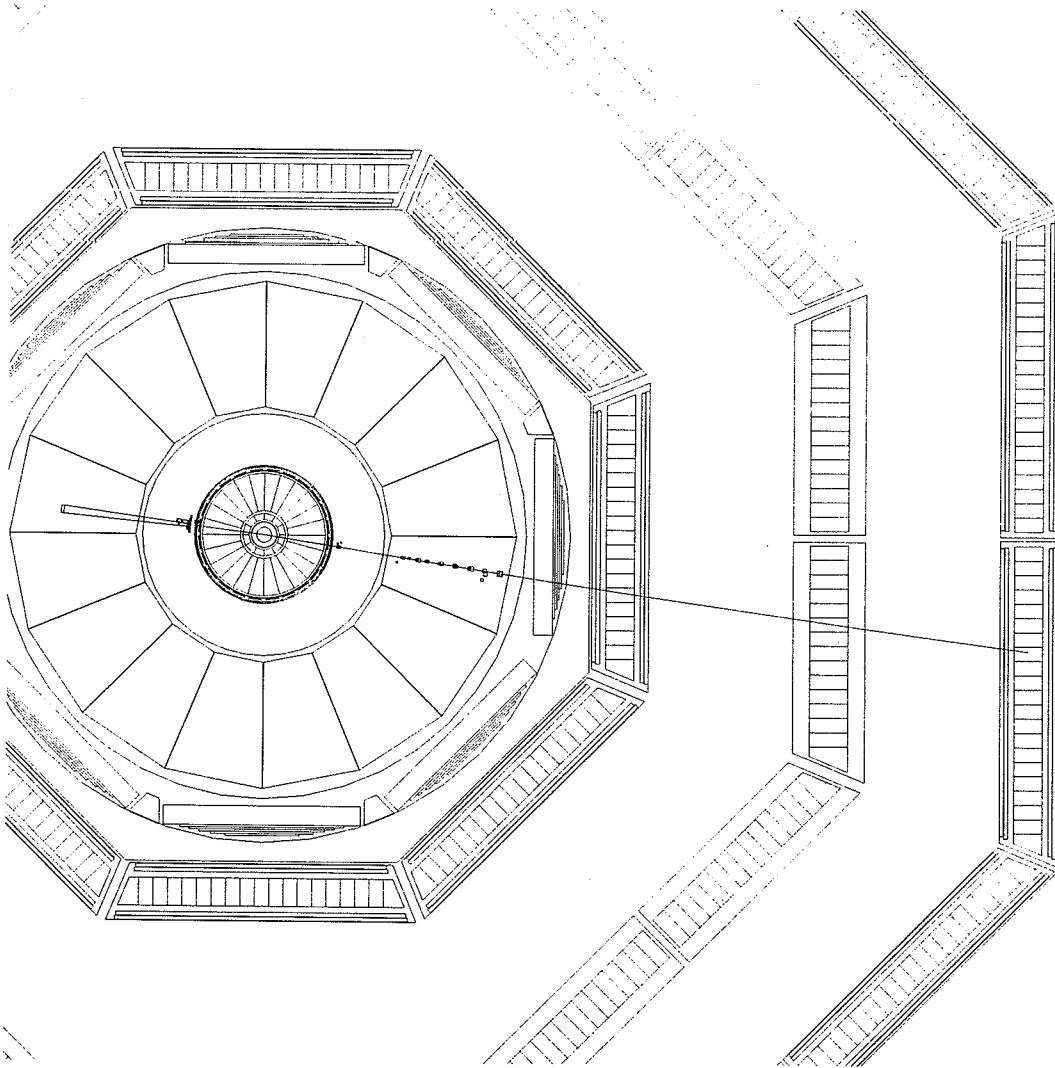


Figure 6.12: An event selected for the $e\mu$ channel.

$$Z^0 \rightarrow \tau^+ \tau^- \rightarrow (\pi\nu)X$$

Dimuon and Bhabha background is rejected by cuts on the hemisphere opposite to the identified $\tau \rightarrow \pi\nu$ decay. Thus, if there is a track in the muon spectrometer, its momentum is required to be less than $0.8 E_{\text{beam}}$ for a "triplet" or $0.6 E_{\text{beam}}$ for a "doublet". Events with one TEC track on the recoil side, which match in space a mip trace both in the BGO and in the HCAL, are rejected. The electromagnetic energy in

Run # 451301 Event # 4444

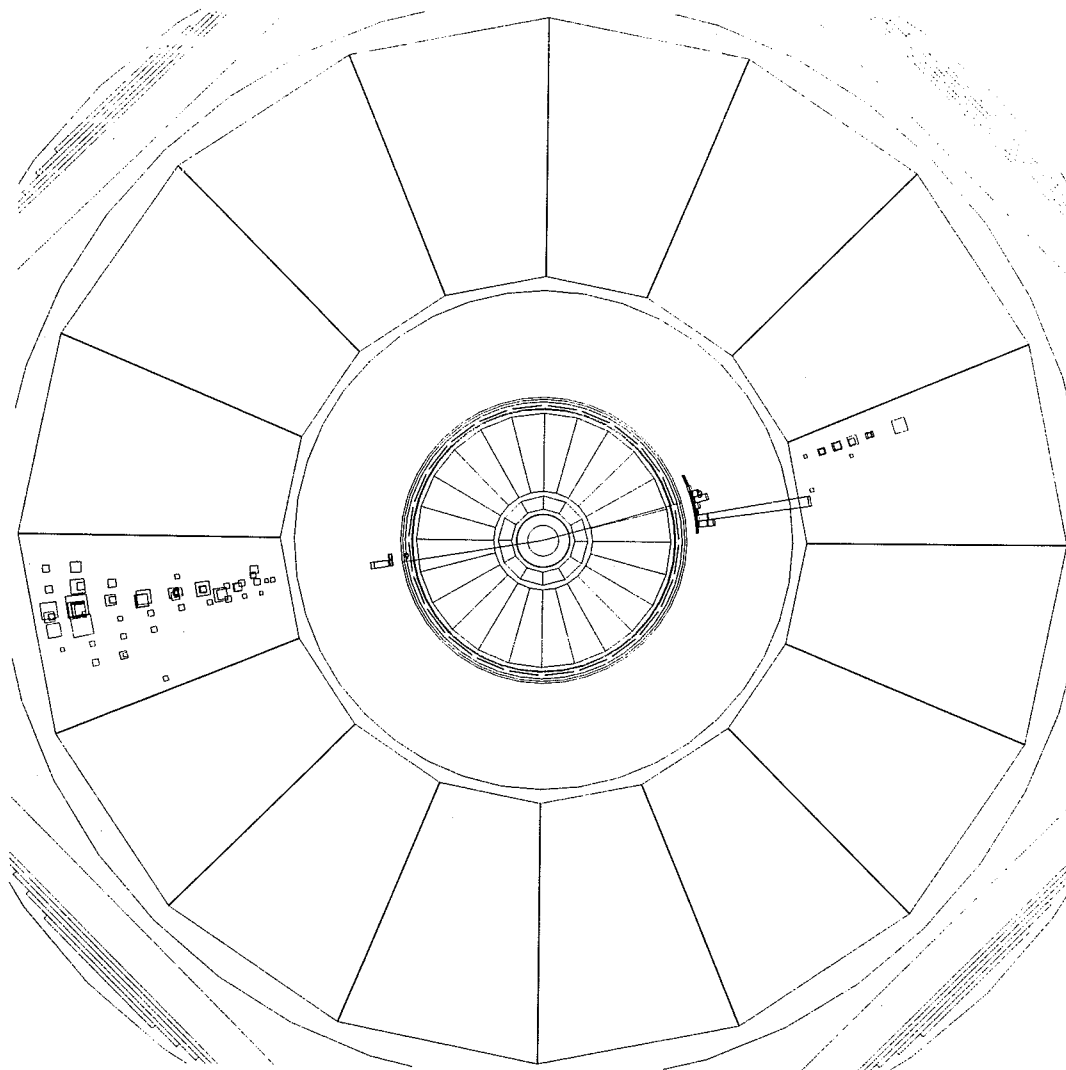


Figure 6.13: An event consisting of a pion candidate in the left hemisphere and a candidate for the $\tau \rightarrow \rho\nu$ decay in the right hemisphere.

Channel $Z \rightarrow \tau\tau \rightarrow$	Selected events				ε (%) in 4π	Background (%)	
	1991	1992	1993	Total		$\tau\tau \not\rightarrow$	$Z \not\rightarrow \tau\tau$
e e	210	440	474	1124	39.8	3.4	2.0
e μ	280	530	586	1396	28.2	2.7	0.5
e π	206	515	523	1244	34.3	10.7	0.2
e ρ	430	960	1011	2401	32.2	14.3	0.2
e X	1101	2501	2693	6295	66.5	1.9	4.5
$\mu\mu$	139	211	231	581	22.7	1.0	3.0
$\mu\pi$	167	371	361	899	26.6	10.2	4.5
$\mu\rho$	309	721	723	1753	24.6	13.7	2.8
μX	749	1511	1625	3885	42.7	1.0	5.5
$\pi\pi$	68	177	186	431	29.3	17.0	0.5
$\pi\rho$	283	619	658	1560	27.4	21.1	0.2
πX	687	1417	1636	3740	57.0	11.0	1.8
$\rho\rho$	352	633	639	1624	25.7	24.0	0.2
ρX	1312	2681	2837	6830	52.5	13.2	0.2
<i>Total</i>	6293	13287	14183	33763			

Table 6.1: Number of selected events for the considered $Z^0 \rightarrow \tau^+\tau^- \rightarrow AB$ decay channels together with the average acceptance ε and the background from $Z^0 \rightarrow \tau\tau \not\rightarrow AB$ and $Z^0 \not\rightarrow \tau\tau$ sources.

the recoil hemisphere should be less than $0.9 E_{\text{beam}}$. In order to reject $\gamma\gamma$ background, the total calorimetric energy should be greater than $0.15\sqrt{s}$ or at least one TEC track should have $p_t > 5$ GeV.

$$Z^0 \rightarrow \tau^+\tau^- \rightarrow (\rho\nu)(\rho\nu)$$

Residual two-photon background is rejected by cutting on the acollinearity, which should be less than 30° .

$$Z^0 \rightarrow \tau^+\tau^- \rightarrow (\rho\nu)X$$

Dimuon and Bhabha background is suppressed by cuts on the hemisphere opposite to the identified $\tau \rightarrow \rho\nu$ decay. Thus, if there is a track in the muon spectrometer, its momentum is required to be less than $0.8 E_{\text{beam}}$ for a ‘‘triplet’’ or $0.6 E_{\text{beam}}$ for a ‘‘doublet’’. Events with one TEC track on the recoil side, which match in space a mip trace both in the BGO and in the HCAL, are rejected. The electromagnetic energy in the recoil hemisphere should be less than $0.9 E_{\text{beam}}$.

The absolute (in 4π) acceptance and the background fractions due to misidentified τ decays are extracted from the Monte Carlo sample of $Z^0 \rightarrow \tau^+\tau^-$ events, which corresponds to an integrated luminosity nine times more than in the data. The non- τ background for every decay mode was estimated from the data and verified with Monte Carlo samples of Bhabha, dimuon, and two-photon events. For eX , μX , πX , and ρX channels, non- τ background was estimated using characteristics of the hemisphere opposite to the identified τ decay. For other channels, whole event characteristics, such as acollinearity, total energy, transverse momentum imbalance, have been employed. Cosmic ray contamination was estimated from the data, using distributions of the scintillator time-of-flight and DCA of the TEC tracks. The numbers of selected events, acceptance and the background fractions for the fourteen exclusive decay channels $Z^0 \rightarrow \tau^+\tau^- \rightarrow ee, e\mu, e\pi, e\rho, eX, \mu\mu, \mu\pi, \mu\rho, \mu X, \pi\pi, \pi\rho, \pi X, \rho\rho, \rho X$, considered in the analysis, are summarized in Table 6.1. The identification efficiencies for the selected $\tau \rightarrow e\bar{\nu}\nu, \tau \rightarrow \mu\bar{\nu}\nu, \tau \rightarrow \pi\nu$ and $\tau \rightarrow \rho\nu$ decays are shown in Figure 6.14 as functions of their decay variables.

6.4 Energy Resolution and Calibration

Since the energy distributions of the τ decay products are used to infer the τ decay parameters and the τ polarization, a precise understanding of the energy measurement in the detector is required. Uncertainties in the energy resolution, such as scale or non-linearity of the energy measurement in the various subdetectors, are potentially serious sources of the systematic error. Furthermore, the statistical precision of the results depends on the detector resolution.

In this section the energy measurement for muons, electrons (photons) and charged pions is described. The checks used to verify the energy scales of the different subdetectors are discussed.

6.4.1 Muon Momentum Measurement

The muon momentum is calculated from the sagitta measurement in the muon spectrometer, corrected for the average energy loss in the material. The momentum resolution can be parameterized as follows:

$$p \cdot \sigma_{1/p} = \alpha \cdot p_t \oplus \beta \oplus \frac{\gamma}{p_t} \quad (6.6)$$

where $p(p_t)$ is the momentum (transverse momentum) of the muon, and α, β, γ describe the characteristics of the detector. The term proportional to α describes the intrinsic resolution of the spectrometer and has contributions from the precision of the

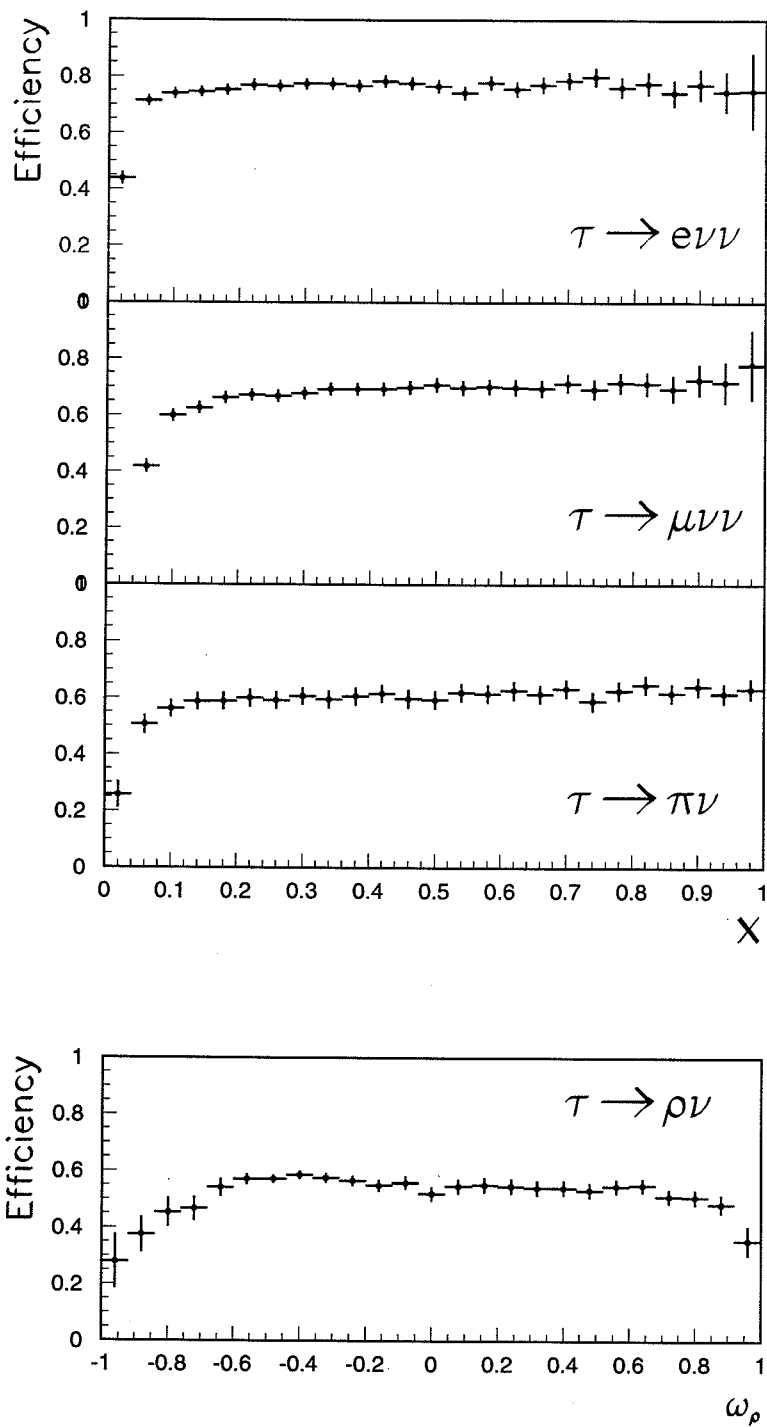


Figure 6.14: Identification efficiency in the fiducial volume for the different τ decay modes used in the analysis. $\tau \rightarrow \mu\bar{\nu}\nu$ corresponds to an identified muon traversing at least three layers of the muon spectrometer (“triplets”).

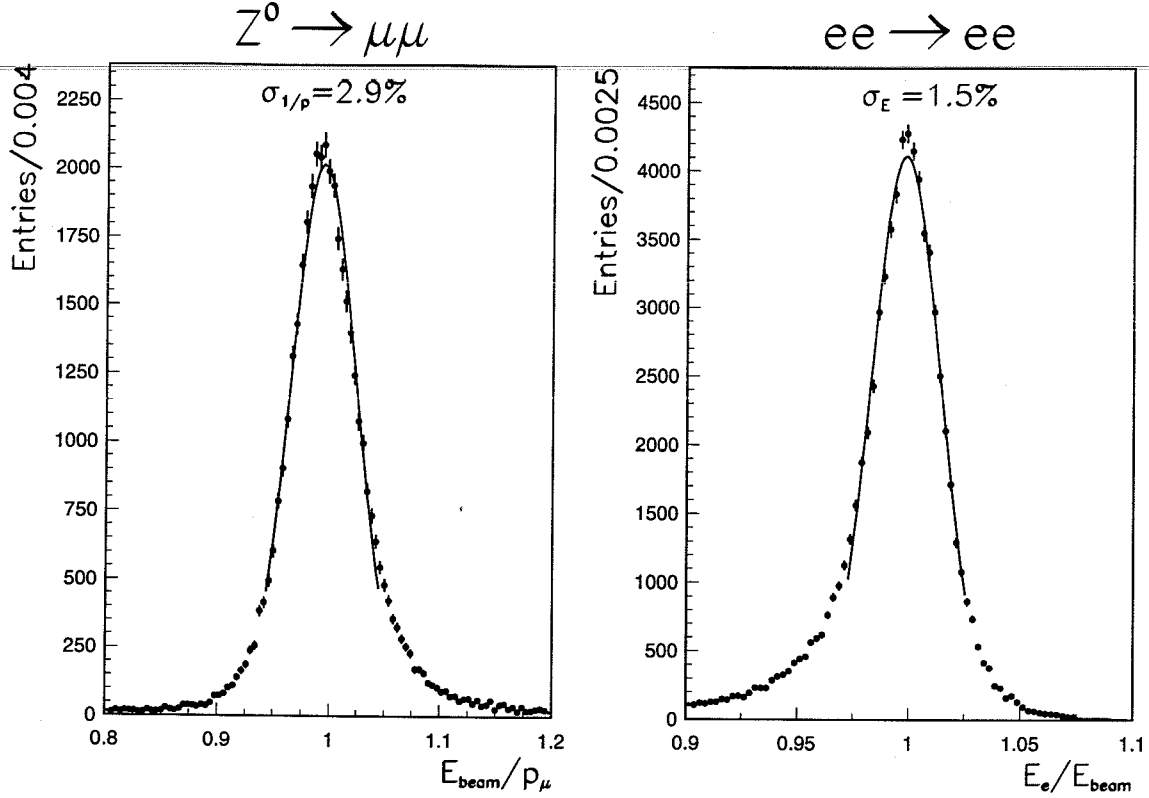


Figure 6.15: The resolution of $1/p_\mu$ for “triplet” muons from $Z^0 \rightarrow \mu\mu$ decays and the BGO energy resolution for electrons in Bhabha events. The solid lines are the results of a gaussian fit to the central part of these distributions.

coordinate reconstruction of the drift chambers and from the relative alignment of the drift chamber layers in one octant. β is due to the multiple scattering of the muons in the regions between the chamber layers. The term proportional to γ is due to the uncertainty on the average energy loss of muons traversing through the detector material from the interaction vertex to the spectrometer.

The time-to-distance relation (*cell map*) in the muon chambers has been determined by analysis of the test beam data [78]. The results of this calibration are used in the reconstruction of the muon momentum for the data, with the exception of the drift velocity and the drift angle, which are adjusted to optimize the momentum resolution in the data using $Z^0 \rightarrow \mu^+\mu^-$ events. In the $Z^0 \rightarrow \mu^+\mu^-$ events, the muon momenta are known from the beam energy, and, hence, the resolution at $p_\mu = \frac{1}{2}\sqrt{s}$ is determined from the distribution of E_{beam}/p_μ (Figure 6.15).

The momentum dependence of the resolution for the entire momentum range is determined from the Monte Carlo simulation of $\tau \rightarrow \mu\bar{\nu}\nu$ and $Z^0 \rightarrow \mu^+\mu^-$ decays. A fit to equation (6.6) fixes three parameters α , β and γ for the Monte Carlo (Figure 6.16).

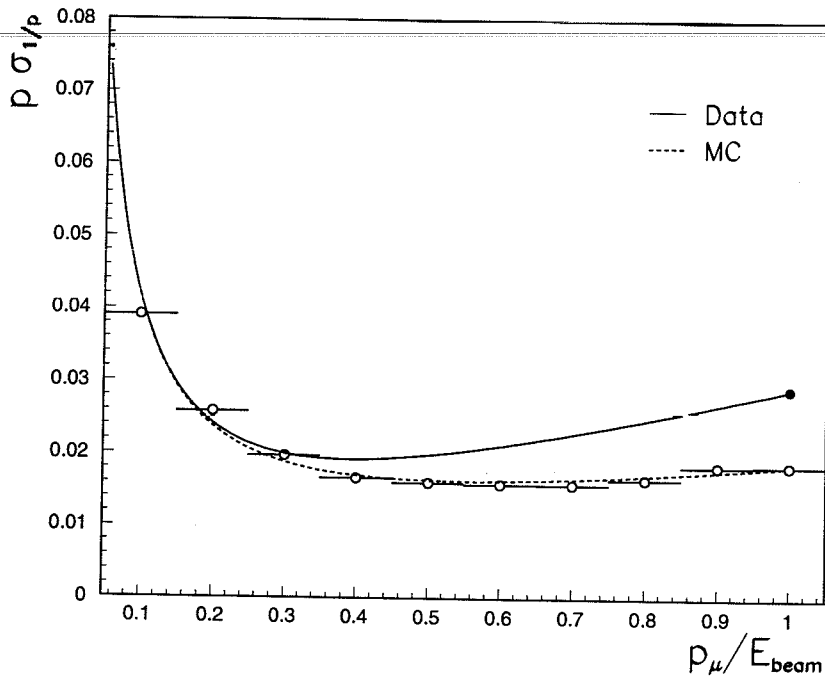


Figure 6.16: The muon momentum resolution for “triplets”.

The data resolution function is obtained by taking β and γ from the Monte Carlo, and constraining α by the requirement, that the resolution function at $p_\mu = \frac{1}{2}\sqrt{s}$ to be equal to the resolution in the data, measured from $Z^0 \rightarrow \mu^+\mu^-$ events [118]. This procedure assumes that the Monte Carlo correctly simulates multiple scattering for muons and any discrepancy between data and Monte Carlo is most likely due to Monte Carlo idealization of certain effects in the drift chambers of the muon spectrometer. Thus, the Monte Carlo resolution is corrected afterwards to reproduce data, see Figure 6.16.

Possible sources of systematic uncertainty in the momentum scale include the energy loss calculation and the sagitta measurement. The accuracy of the muon momentum scale is estimated to be 0.2% at 45.6 GeV using $Z^0 \rightarrow \mu^+\mu^-$ decays. The momentum scale at low energies is dominated by muon energy loss in the calorimeters, which is known to an accuracy of 50 MeV, and is checked by comparing measured transverse momenta in the TEC and the muon spectrometer for $\tau \rightarrow \mu\bar{\nu}\nu$ decays [116].

6.4.2 Electromagnetic Energy Measurement

The reconstruction in the BGO starts from the formation of geographical clusters: neighboring crystals with energy above a threshold are grouped in a cluster. Then, all local maxima inside a cluster are searched. Each local maximum with energy greater

than 40 MeV forms a bump ².

Due to the size of a crystal almost being equal to the Molière radius of the BGO, 93% of the energy deposited by an incident electron (photon) is spread over a crystal matrix of 3×3 around the bump crystal. It is known from the test beam study that this fraction weakly depends on the impact point of the incident particle [117]. Using this fact, the energy of the showering particle, assuming its electromagnetic origin, is calculated from the sum of crystal energies in 3×3 matrix, which is corrected for the impact point position as well as for the rear and lateral losses:

$$E_{em} = \frac{\sum_{j=1}^9 E_j}{0.1231 \frac{E_1}{\sum_{j=1}^9 E_j} + 0.8222} \quad (6.7)$$

The correction factors used in this formula have been determined for the barrel part from the test beam of 10 GeV electrons. For energies below 3 GeV, the sum of six most energetic crystals within 3×3 matrix is used instead of all nine.

The energy dependence of the BGO energy resolution has been measured during the test beam study and Bhabha data sample, and can be parametrized as

$$\frac{\sigma_E}{E} = \left(\frac{a}{\sqrt{E}} + b \right) \oplus \frac{c}{E} \quad (6.8)$$

where E is an electron energy in GeV and parameters $a = (1.50 \pm 0.05) \times 10^{-2}$, $b = (1.02 \pm 0.09) \times 10^{-2}$, $c = (1.06 \pm 0.17) \times 10^{-2}$ [87] correspond to the resolution in the data known from the Bhabha peak (Figure 6.15).

An absolute *in situ* calibration of the BGO calorimeter is performed using the electrons from Bhabha events. The Xenon system [88] is necessary to monitor possible variations of the light collection efficiency. Dedicated cosmic ray runs [90] and the RFQ accelerator are used to update and cross-check calibration constants. The BGO energy scale for the electromagnetic energy measurement is known to 0.1% accuracy at 45 GeV from the Bhabha events and is estimated to be accurate to 1.0% at 1 GeV from the π^0 peak position (Figure 6.10) [116].

6.4.3 Charged Pion Energy Measurement

The energy of charged pions is measured in two independent and supplementary ways by the momentum measurement in the TEC and the calorimetric energy measurement in the BGO and HCAL.

²If there is no crystals with energy more than 40 MeV in a cluster, then the most energetic crystal is assigned as a bump.

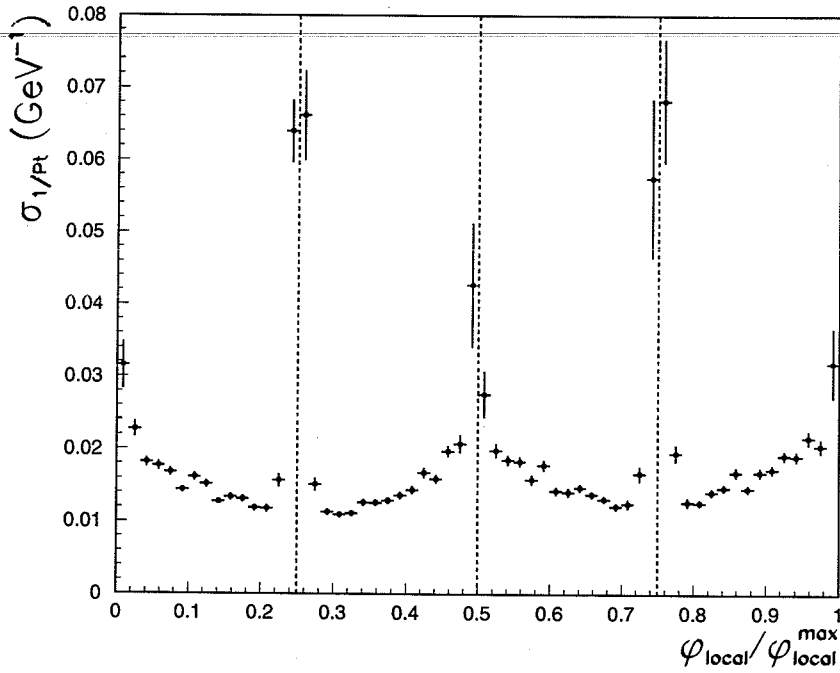


Figure 6.17: The TEC p_t resolution in the barrel as a function of φ_{local} as obtained from dimuon events in 1993. φ_{local} spans a size of one Inner TEC sector, i.e. $\varphi_{\text{local}}^{\text{max}} = \pi/6$. The leftmost and rightmost dashed vertical lines give the anode positions in Outer TEC. The middle line corresponds to the anode plane in Inner TEC and the cathode plane of Outer TEC.

TEC Momentum Measurement

The parameters of a track in the TEC, such as transverse momentum (p_t), distance of closest approach to the interaction vertex (DCA) and azimuthal angle at vertex (φ), are determined by fitting a circle to the reconstructed space points associated with the track, where the space points are computed from the position of the hit anodes and the measured drift times. Since it is expected the measured drift distances to be normally distributed around their true values, the track sagitta is also normally distributed. As sagitta is related to p_t by $s \sim 1/p_t$, the TEC resolution is evaluated in terms of $1/p_t$. Also note that the curvature resolution is virtually independent of the curvature itself, thus σ_{1/p_t} is independent of p_t .

The TEC resolution in the barrel ($|\cos\theta| < 0.82$) has been measured using dimuon events, which provide a sample of charged tracks with known energy ($E_{\text{track}} = E_{\text{beam}}$) and charge determined unambiguously by the muon spectrometer. The TEC resolution can thus be determined by comparing the curvature measured by the TEC with the

curvature computed from E_{beam} :

$$\sigma_{1/p_t} = \frac{1}{E_{\text{beam}} Q \sin \theta} - \frac{1}{p_t} \quad (6.9)$$

where Q and θ are a sign and polar angle of the momentum measured in the muon spectrometer. The TEC resolution demonstrates a strong dependence on the azimuthal angle, see Figure 6.17. The resolution in the amplification region is severely degraded due to the high and nonuniform electric field. At the same time, tracks which pass far from the anodes suffer from the diffusion along the drift path. The average TEC resolution is measured to be 0.018 GeV^{-1} . The details of the TEC calibration procedure could be found in [94]. The improvement of the $1/p_t$ resolution by including the fill vertex in the fit for transverse momentum is described in [119].

The TEC momentum scale was verified to 1% accuracy from 1 GeV to 45 GeV using a data sample of dimuon events and identified $\tau \rightarrow \mu \bar{\nu} \nu$ decays by comparison of track curvature measurements in the TEC and in the muon spectrometer.

Calorimetric Energy Measurement

A calorimetric calibration has been developed [118] using a test beam sample of over 10^6 monochromatic charged pions with energies ranging from 4 to 50 GeV [84]. The pion calorimetric energy is given by the weighted sum of the measured energies in the BGO and HCAL

$$E_{\text{CAL}} = f_B(E_{\pi^\pm}) \cdot E_{\text{BGO}} + g_H(\theta, \varphi) \cdot f_H(E_{\pi^\pm}) \cdot E_{\text{HCAL}} \quad (6.10)$$

where f_B , g_H , f_H are calibration functions determined from the test beam data. In particular, $g_H(\theta, \varphi)$ equalizes nonuniformity in θ and φ of HCAL energy response which is due to its modular structure. The energy dependence of (6.10) has been found to be mild, allowing the application of an iterative procedure. The calorimetric energy resolution for charged pions is determined to be $\sigma_E/E = 0.55/\sqrt{E} + 0.08$.

The absolute energy scales of the BGO and HCAL for charged pions are estimated to 1.5% in the barrel from the peak position of the $\pi^\pm \pi^0$ invariant mass distribution for the identified $\tau \rightarrow \rho \nu$ decays (Figure 6.11).

Combined Energy Measurement

The procedure for combining the calorimetric energy measurement with the momentum measurement from the TEC consists of determining the π^\pm energy, E_π , that maximizes the probability of these two measurements arise from the same source:

$$P(E_{\text{CAL}}|p_t) = P(E_{\text{CAL}}|E_\pi) \cdot P(p_t, \sin \theta | p_\pi = \sqrt{E_\pi^2 - m_\pi^2}) \quad (6.11)$$

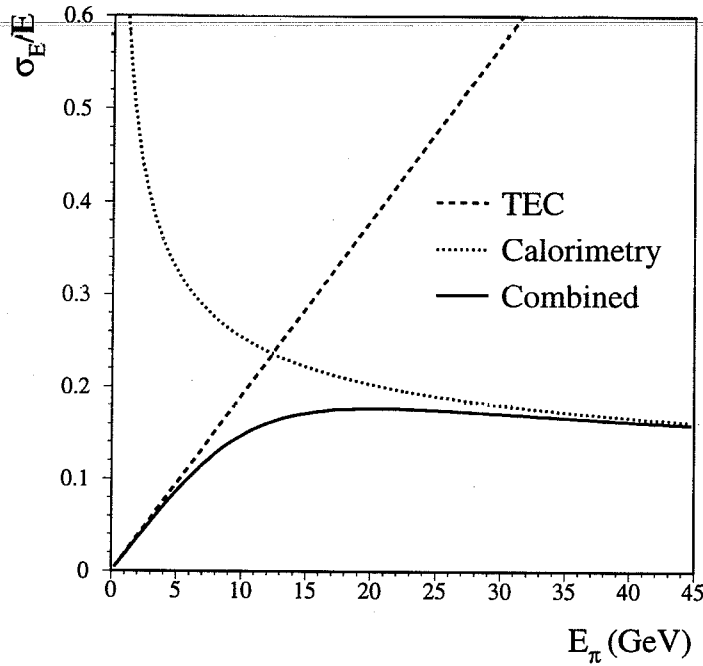


Figure 6.18: Average energy resolution for charged pions attained by combining independent measurements of TEC momentum and calorimetric energy.

$$= \frac{1}{\sqrt{2\pi}\sigma_{CAL}(E_\pi)} e^{-\frac{(E_{CAL} - E_\pi)^2}{2\sigma_{CAL}^2(E_\pi)}} \cdot \frac{1}{\sqrt{2\pi}\sigma_{1/p_t}} e^{-\frac{(\frac{1}{p_t} - \frac{1}{p_\pi \sin \theta})^2}{2\sigma_{1/p_t}^2}}$$

where E_{CAL} is the calorimetric energy, p_t is the transverse momentum measured by the TEC, and σ_{CAL} and σ_{1/p_t} are the estimated errors on these measurements. σ_{CAL} and σ_{1/p_t} depend on the track polar angles φ and θ .

This procedure also provides a test of the compatibility of these two independent measurements. The quantity for such test is given by the maximum value of $P(E_\pi) = P(E_{CAL}|E_\pi) \cdot P(p_t|E_\pi)$, obtained from the above procedure.

Combining calorimetric and TEC measurements improves charged pion energy resolution as it is illustrated on Figure 6.18 for the calorimetric and TEC average resolutions.

Chapter 7

Measurement

In this chapter the measurement of the Michel parameters and the hadronic chirality parameter in τ lepton decays is described. These τ decay parameters are extracted together with the average τ polarization from a binned maximum likelihood fit to the distributions of the τ pair decay products in the following channels: $Z^0 \rightarrow \tau^+\tau^- \rightarrow ee, e\mu, e\pi, e\rho, eX, \mu\pi, \mu\rho, \mu X, \pi\pi, \pi\rho, \pi X, \rho\rho, \rho X$, where X designates a τ decay not identified as e, μ , π and ρ . First, it is described how the likelihood function is constructed. Then, the measurement of the Michel parameters $\rho, \eta, \xi, \xi\delta$, the hadronic chirality parameter ξ_h and the average τ polarization P_τ is presented both with and without universality assumption in the τ lepton decays. Finally, the evaluation of the systematic errors is described.

7.1 The Likelihood Function

Data events selected as one of the following exclusive channels: $Z^0 \rightarrow \tau^+\tau^- \rightarrow ee, e\mu, e\pi, e\rho, eX, \mu\pi, \mu\rho, \mu X, \pi\pi, \pi\rho, \pi X, \rho\rho, \rho X$ are retained for the further fit. For every identified τ decay in an event, the respective decay variable, $x_l = E_l/E_{\text{beam}}$ for the identified leptonic τ decays, $x_\pi = E_\pi/E_{\text{beam}}$ for the identified $\tau \rightarrow \pi\nu_\tau$ decays and ω_ρ for the identified $\tau \rightarrow \rho\nu_\tau$ decays, is calculated. Then, each event enters into only one distribution, according to its channel. Thus, eX, $\mu X, \pi X, \rho X$ form one-dimensional distributions, and ee, e $\mu, e\pi, e\rho, \mu\pi, \mu\rho, \pi\pi, \pi\rho, \rho\rho$ form two-dimensional distributions. The decay variables are binned in steps of 0.05 for x_e and x_μ , 0.0875 for x_π , 0.1 for ω_ρ . The range of the variables for every distribution is shown in Table 7.2. Distributions for the ee, $\pi\pi$ and $\rho\rho$ channels are folded across the diagonal.

The signal distributions are obtained in the following way. First, the theoretical cross-sections

$$\frac{1}{\Gamma} \frac{d\Gamma}{dx_A} = H_0^{(A)}(x_A) - P_\tau H_1^{(A)}(x_A) \quad (7.1)$$

and

$$\frac{1}{\sigma} \frac{d^2\sigma}{dx_A dx_B} = H_0^{(A)}(x_A) H_0^{(B)}(x_B) + H_1^{(A)}(x_A) H_1^{(B)}(x_B) \quad (7.2)$$

$$- P_\tau \left[H_1^{(A)}(x_A) H_0^{(B)}(x_B) + H_0^{(A)}(x_A) H_1^{(B)}(x_B) \right]$$

are convoluted with the L3 detector resolution. Owing to the form of these cross-sections, the detector resolution is applied to the H_0 and H_1 functions for every considered τ decay mode separately. In the case of leptonic τ decays, the same procedure as described in Section 4.1.1 is carried out in order to obtain the $h_0^{(l)}$, $h_\eta^{(l)}$, $h_\rho^{(l)}$, $h_\xi^{(l)}$, $h_{\xi\delta}^{(l)}$ functions. In course of this procedure, the resolution of the BGO energy response and the muon momentum reconstruction is applied in their analytical form (6.6) and (6.8) on the generated decays for every sample in Table 4.1. The result of this convolution is shown on Figures 7.1 and 7.2. In the case of the $\tau \rightarrow \pi\nu_\tau$ decay, first the resolutions of the calorimetric energy measurement and the sagitta measurement of the TEC are applied to each generated decay, which are then combined into the best pion energy estimate in the same way (6.11) as it is done for the data. Afterwards, the functions $h_0^{(\pi)}$ and $h_1^{(\pi)}$ are obtained using the method, described in Section 4.1.2. The resulting convoluted functions $h_0^{(\pi)}$ and $h_1^{(\pi)}$ are shown on Figure 7.3. In the case of the $\tau \rightarrow \rho\nu_\tau$ decay, the $h_0^{(\rho)}$ and $h_1^{(\rho)}$ functions are obtained from Monte Carlo signal decays which passed the full detector simulation, reconstruction and identification procedure. This was decided because of the complications of reproducing by analytical methods the resolution and the selection acceptance for two distinct cases of π^0 reconstruction in the $\tau \rightarrow \rho\nu_\tau$ decay: first, when a π^0 is formed by one neutral cluster ($\approx 78\%$), and, second, when it is formed by two separate neutral clusters in the BGO ($\approx 22\%$). In addition, this was justified by the fact that the final event selection of $e\rho$, $\mu\rho$, $\pi\rho$, $\rho\rho$ and ρX channels *does not* distort these functions. The method of obtaining $h_0^{(\rho)}$ and $h_1^{(\rho)}$ functions is similar as described in Section 4.1.2. The resulting convoluted functions $h_0^{(\rho)}$ and $h_1^{(\rho)}$ are shown on Figure 7.4. Binning of the convoluted h functions is the same as in data.

In order to account for distortion of the distributions due to the particle identification procedure and the final event selection, theoretical cross-sections, already convoluted with the detector resolution, have to be corrected for possible non-uniformity of the signal acceptance. For this purpose, the efficiency of the particle identification and event selection has been determined for every decay channel in the histogram form of the *generated* decay variables from the Monte Carlo sample of $Z^0 \rightarrow \tau^+\tau^-$ events. Applying these efficiencies to the sample of the generated τ decays and using the detector resolutions described above, the efficiency for every decay channel is obtained now in the histogram form of the *reconstructed* decay variables. Binning of the efficiency histograms is the same as in data.

Finally, the signal distributions are obtained by putting the H_0 and H_1 functions,

$$\tau \rightarrow e \nu \nu$$

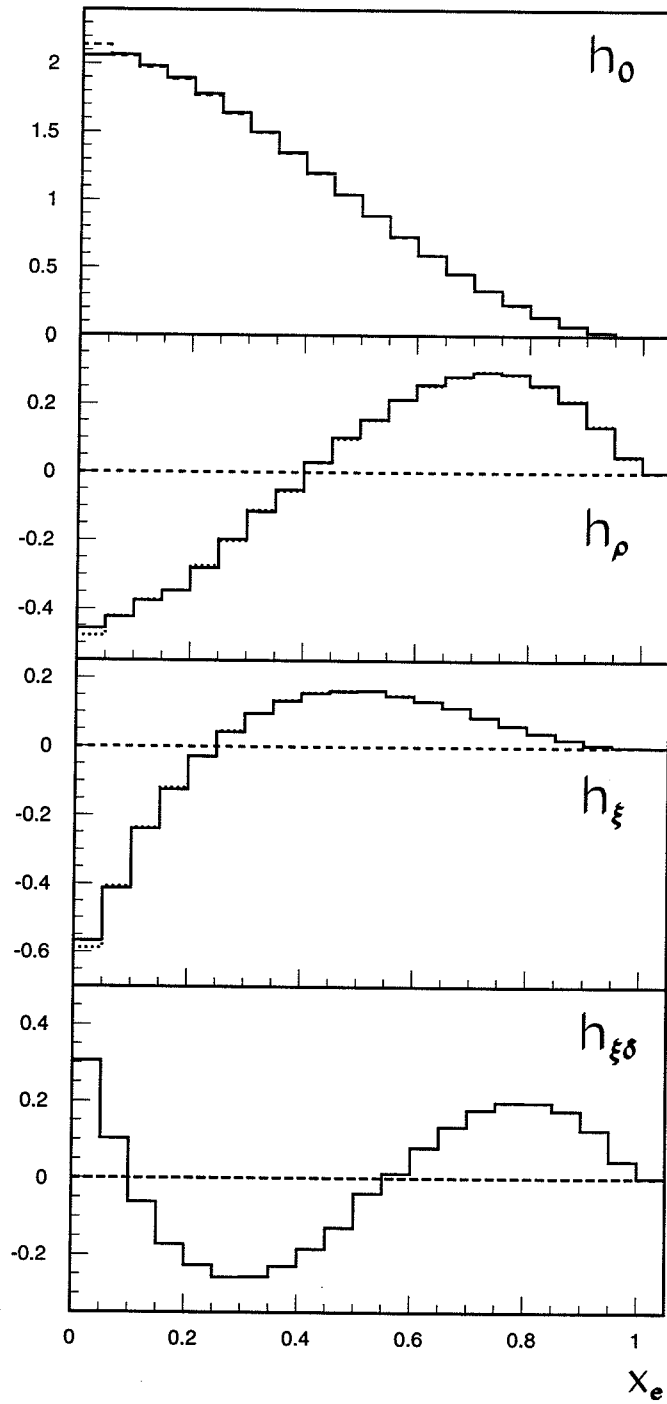


Figure 7.1: Functions h_0 , h_ρ , h_ξ , $h_{\xi\delta}$ of the decay $\tau \rightarrow e \bar{\nu}_e \nu_\tau$ convoluted with the detector resolution are shown as solid histograms. Superimposed (dotted) histograms represent these functions before the detector resolution has been applied.

$$\tau \rightarrow \mu\bar{\nu}_\mu\nu_\tau$$

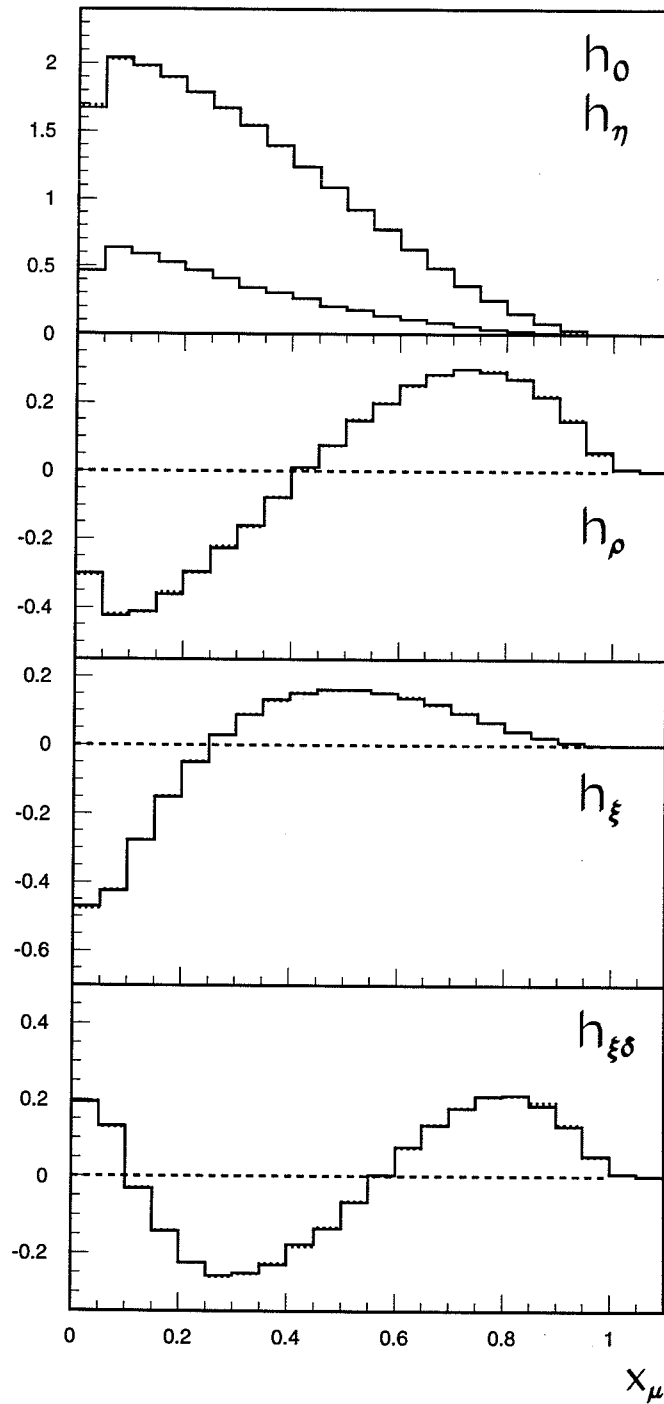


Figure 7.2: Functions h_0 , h_η , h_ρ , h_ξ , $h_{\xi\delta}$ of the decay $\tau \rightarrow \mu\bar{\nu}_\mu\nu_\tau$ convoluted with the detector resolution are shown as solid histograms. Superimposed (dotted) histograms represent these functions before the detector resolution has been applied.

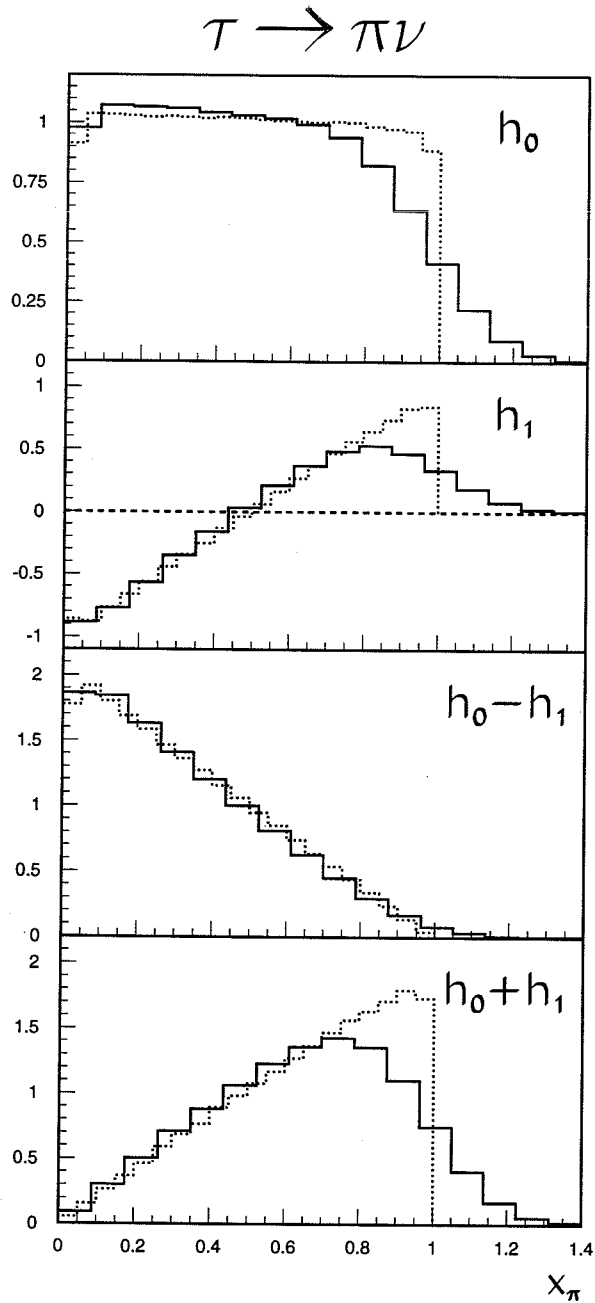


Figure 7.3: Functions h_0 and h_1 of the decay $\tau \rightarrow \pi \nu_\tau$ convoluted with the detector resolution are shown as solid histograms. Superimposed (dotted) histograms represent these functions before the detector resolution has been applied. The difference $h_0 - h_1$ and the sum $h_0 + h_1$ give the π spectrum from *left-handed* and *right-handed* τ decays, respectively.

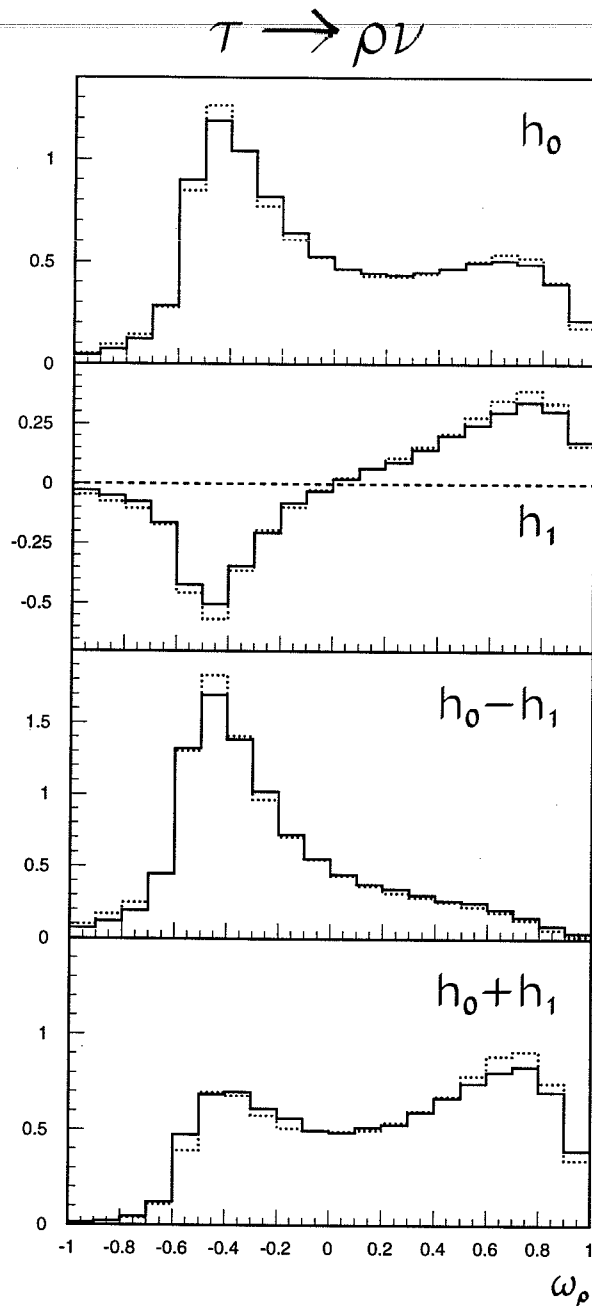


Figure 7.4: Shown as solid histograms are the h_0 and h_1 functions of the decay $\tau \rightarrow \rho \nu_\tau$ as obtained from selected Monte Carlo $\tau \rightarrow \rho \nu_\tau$ decays after the full detector simulation and reconstruction have been applied. Superimposed (dotted) histograms represent these functions before the detector resolution has been applied. Their difference $h_0 - h_1$ and the sum $h_0 + h_1$ give the ρ spectrum from *left-handed* and *right-handed* τ decays, respectively.

convoluted with the L3 detector resolution, \mathcal{H}_0 and \mathcal{H}_1 , into the theoretical cross-sections (7.1) and (7.2) and multiplying them by the selection efficiency, ε :

$$S_{Aj}(\alpha) = \mathcal{N}_A \varepsilon_A(j) \left\{ \mathcal{H}_0^{(A)}(j) - P_\tau \mathcal{H}_1^{(A)}(j) \right\} \quad (7.3)$$

$$S_{ABjk}(\alpha) = \mathcal{N}_{AB} \varepsilon_{AB}(j, k) \left\{ \mathcal{H}_0^{(A)}(j) \mathcal{H}_0^{(B)}(k) + \mathcal{H}_1^{(A)}(j) \mathcal{H}_1^{(B)}(k) \right. \\ \left. - P_\tau \left[\mathcal{H}_1^{(A)}(j) \mathcal{H}_0^{(B)}(k) + \mathcal{H}_0^{(A)}(j) \mathcal{H}_1^{(B)}(k) \right] \right\}, \quad (7.4)$$

where α denotes a set of the fitted parameters and \mathcal{N} is a normalization. For example, in the fit assuming universality in τ decays:

$$\alpha = \{P_\tau, \rho, \eta, \xi, \xi\delta, \xi_h\}.$$

The expectation is given by the sum of the signal (S), τ background from the particle misidentification (B^τ) and non- τ background (B^{other}) distributions:

$$\nu_{Aj}(\alpha) = S_{Aj}(\alpha) + B_{Aj}^\tau(P_\tau) + B_{Aj}^{other} \quad (7.5)$$

$$\nu_{ABjk}(\alpha) = S_{ABjk}(\alpha) + B_{ABjk}^\tau(P_\tau) + B_{ABjk}^{other} \quad (7.6)$$

For each decay channel the signal normalization \mathcal{N} is fixed by the requirement that the total expectation value equals the number of events in the data N :

$$\sum_j \nu_{Aj} = N_A \quad \text{and} \quad \sum_{j,k} \nu_{ABjk} = N_{AB} \quad (7.7)$$

Then, assuming Poisson statistics in every bin, the total likelihood function is formed

$$\mathcal{L} = \prod_s \prod_i \frac{\nu_{si}^{n_{si}} e^{-\nu_{si}}}{n_{si}!} \quad (7.8)$$

where the index s denotes the spectra used in the fit and runs over $ee, e\mu, e\pi, e\rho, eX, \mu\pi, \mu\rho, \mu X, \pi\pi, \pi\rho, \pi X, \rho\rho, \rho X$; index i runs over all bins included in the fit for the particular distribution; n_{si} and ν_{si} are, respectively, the number of data events in bin i of distribution s and the expectation value for this number.

Distributions of the τ background and their fractions have been obtained from the $Z^0 \rightarrow \tau^+\tau^-$ Monte Carlo. Distributions of Bhabha, dimuon and two-photon background have been obtained from their respective Monte Carlo samples and normalized using the ratio of the integrated luminosity in the data and in the generator. Distributions and normalizations of residual cosmic ray events have been obtained directly from the data.

7.2 Fit Results

Assuming universality in the τ decays, the best estimates for $\rho_i, \eta_i, \xi_i, \xi_i\delta_i, \xi_h$ and P_τ are obtained by performing a minimization of the negative logarithm of (7.8), $-\ln \mathcal{L}$,

with respect to these parameters, using the MINUIT function minimization and error analysis package [68]. The resulting values and their corresponding statistical errors are

$$\begin{aligned}
P_\tau &= -0.154 \pm 0.018 \\
\rho_l &= 0.794 \pm 0.039 \\
\eta_l &= 0.25 \pm 0.17 \\
\xi_l &= 0.94 \pm 0.21 \\
\xi_l \delta_l &= 0.81 \pm 0.14 \\
\xi_h &= -0.970 \pm 0.053
\end{aligned}$$

Parameter correlations matrix of the fit is shown in Table 7.1. The goodness of the

	ρ_l	η_l	ξ_l	$\xi_l \delta_l$	ξ_h
P_τ	0.421	0.020	0.144	-0.262	-0.447
ρ_l		0.445	-0.165	-0.279	-0.324
η_l			0.119	0.076	-0.010
ξ_l				0.033	0.106
$\xi_l \delta_l$					0.365

Table 7.1: The parameter correlation matrix of the fit, assuming universality in τ decays.

fit was estimated by the χ^2 test [120]. The χ^2 of the fit, calculated using statistical errors only, is 3053.2 for 2626 degrees of freedom ($\chi^2/dof = 1.163$), suggesting that the systematic errors contribution is not negligible in the comparison to the statistical ones.

The breakdown of the number of events used in the fit, the background fraction, the range of variables in the fit, number of fitted bins and the resulting χ^2 of the fit for every decay channel is shown in Table 7.2. Decay distributions of the data and the result of the fit are shown on Figures 7.5–7.15.

Without assuming $e-\mu$ universality in the leptonic τ decays and considering the hadronic chirality parameter separately for $\tau \rightarrow \pi\nu$ and $\tau \rightarrow \rho\nu$ decays, a minimization of the negative logarithm of the same likelihood (7.8) is made with respect to the following set of parameters: ρ_e , ξ_e , $\xi_e \delta_e$, ρ_μ , η_μ , ξ_μ , $\xi_\mu \delta_\mu$, ξ_π , ξ_ρ and P_τ . The resulting values and their corresponding statistical errors are

$$P_\tau = -0.155 \pm 0.018$$

Channel	Fit range	Events	Bkg.(%)	Bins	χ^2_{fit}
e e	min x_e [0.05, 0.8]	1005	5.1	159/151	211.1
	max x_e [0.15, 0.95]				
e μ	x_e [0.05, 1.05]	1322	2.3	420/295	395.3
	x_μ [0.05, 1.1]				
e π	x_e [0.05, 1.05]	1092	10.3	300/217	336.6
	x_π [0.0875, 1.4]				
e ρ	x_e [0.05, 1.]	2269	14.0	380/312	410.8
	ω_ρ [-1., 1.]				
e X	x_e [0.05, 1.1]	5891	7.3	21/21	20.8
μ π	x_μ [0.05, 1.]	802	16.6	285/200	381.0
	x_π [0.0875, 1.4]				
μ ρ	x_μ [0.05, 1.]	1743	16.5	380/317	437.6
	ω_ρ [-1., 1.]				
μ X	x_μ [0.05, 1.1]	3870	6.3	21/21	13.5
π π	min x_π [0.0875, 1.4]	371	17.8	120/88	123.8
	max x_π [0.0875, 1.4]				
π ρ	x_π [0.0875, 1.4]	1460	20.4	300/236	446.9
	ω_ρ [-1., 1.]				
π X	x_π [0., 1.4]	3733	12.6	16/16	24.1
ρ ρ	min ω_ρ [-1., 1.]	1624	24.2	210/186	214.1
	max ω_ρ [-1., 1.]				
ρ X	ω_ρ [-1., 1.]	6830	13.4	20/20	37.6
<i>Total</i>		32012		2632/2080	3053.2

Table 7.2: The range of the decay variables and number of selected events for every channel considered in the fit, assuming universality in the τ decays, are shown together with the background fraction, number of fitted bins, number of bins populated by the data and the resulting χ^2 of the fit.

$$\begin{aligned}
\rho_e &= 0.776 \pm 0.042 & \rho_\mu &= 1.02 \pm 0.19 \\
& & \eta_\mu &= 0.98 \pm 0.66 \\
\xi_e &= 0.82 \pm 0.25 & \xi_\mu &= 1.66 \pm 0.56 \\
\xi_e \delta_e &= 1.01 \pm 0.18 & \xi_\mu \delta_\mu &= 0.56 \pm 0.26 \\
\xi_\pi &= -0.911 \pm 0.084 & \xi_\rho &= -0.996 \pm 0.072
\end{aligned}$$

Their correlations matrix is shown in Table 7.3. The χ^2 of the fit, calculated using statistical errors only, is 3011.1 for 2622 degrees of freedom ($\chi^2/dof = 1.148$).

	ρ_e	ξ_e	$\xi_e \delta_e$	ρ_μ	η_μ	ξ_μ	$\xi_\mu \delta_\mu$	ξ_π	ξ_ρ
P_τ	0.442	0.110	-0.271	0.008	-0.079	-0.011	-0.060	-0.201	-0.429
ρ_e		-0.237	-0.344	-0.007	-0.050	-0.027	-0.019	-0.196	-0.280
ξ_e			0.001	-0.016	-0.008	0.012	0.050	0.127	-0.008
$\xi_e \delta_e$				0.013	0.019	-0.044	-0.062	0.175	0.318
ρ_μ					0.946	0.572	-0.075	0.036	-0.004
η_μ						0.683	0.040	0.078	0.047
ξ_μ							0.081	0.147	0.063
$\xi_\mu \delta_\mu$								0.040	0.075
ξ_π									-0.020

Table 7.3: The parameter correlation matrix of the fit, not assuming universality in τ decays.

7.3 Systematic Errors

Systematic errors may arise from the following sources: selection procedure, modeling of the background, detector calibration and finite Monte Carlo statistics. These sources are considered to be independent. The corresponding systematic errors have been estimated as the change in the fitted values of the τ decay parameters and τ polarization, varying the most important cuts for the particle identification and event selection, the fraction of background contamination and the energy scales of different subdetectors, and taking into account the finite size of the $Z^0 \rightarrow \tau^+ \tau^-$ Monte Carlo sample.

The effect of an incorrect modeling of non- τ background fractions is determined by scaling them separately within the statistical errors of their normalization. The influence of the event selection procedure on the result is studied by varying the values of the principal cuts, used in the particle identification and the final event selection, within the uncertainties of their modeling in the Monte Carlo. The systematic error due to the uncertainty in the rate of misidentified τ decays, which influences the cross

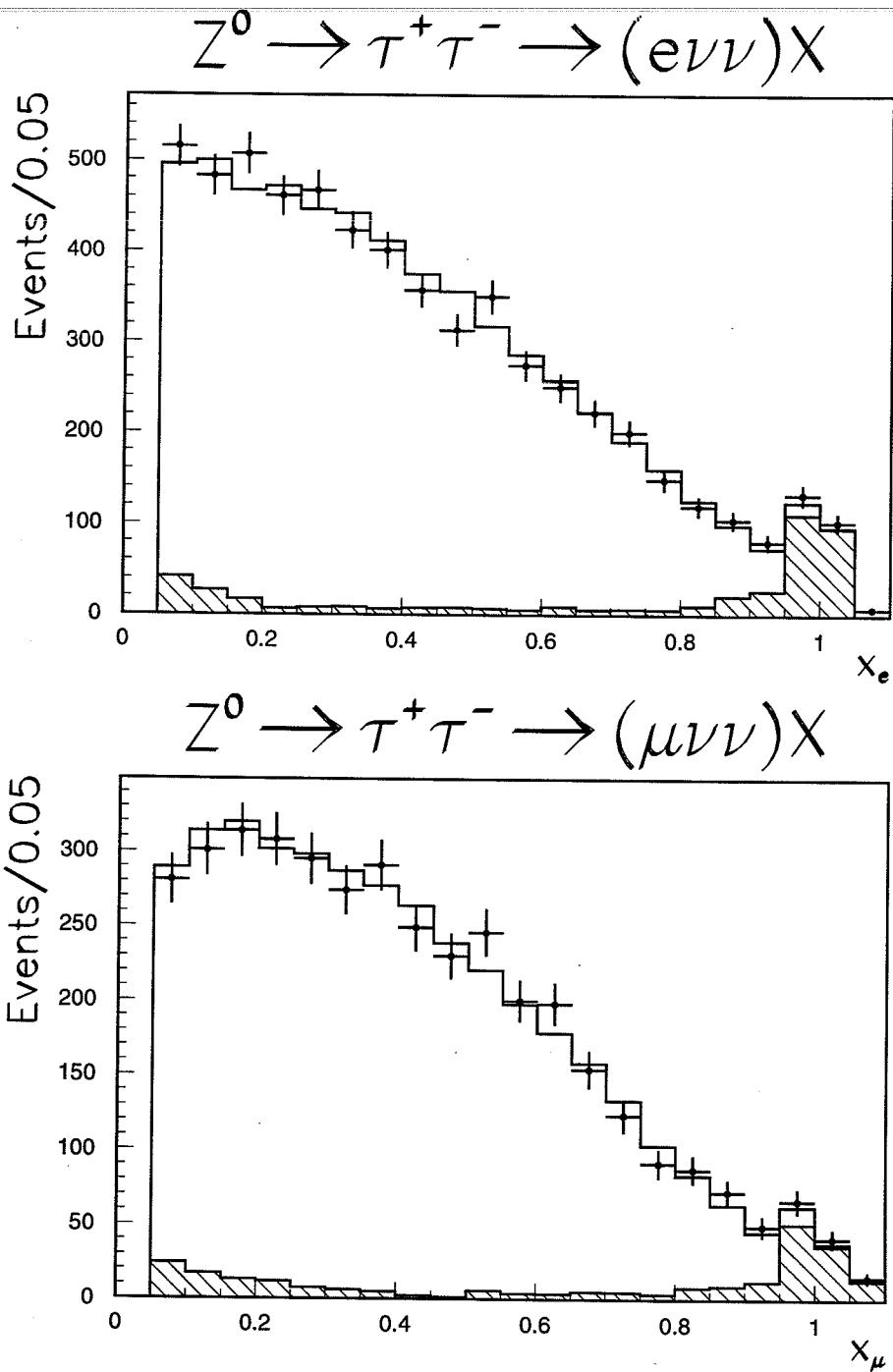


Figure 7.5: Distributions of x_e for the eX channel and x_μ for the μX channel. The data are shown as points with statistical error bars. The solid-line histogram represents the result of the fit. Total background is superimposed as a hatched histogram.

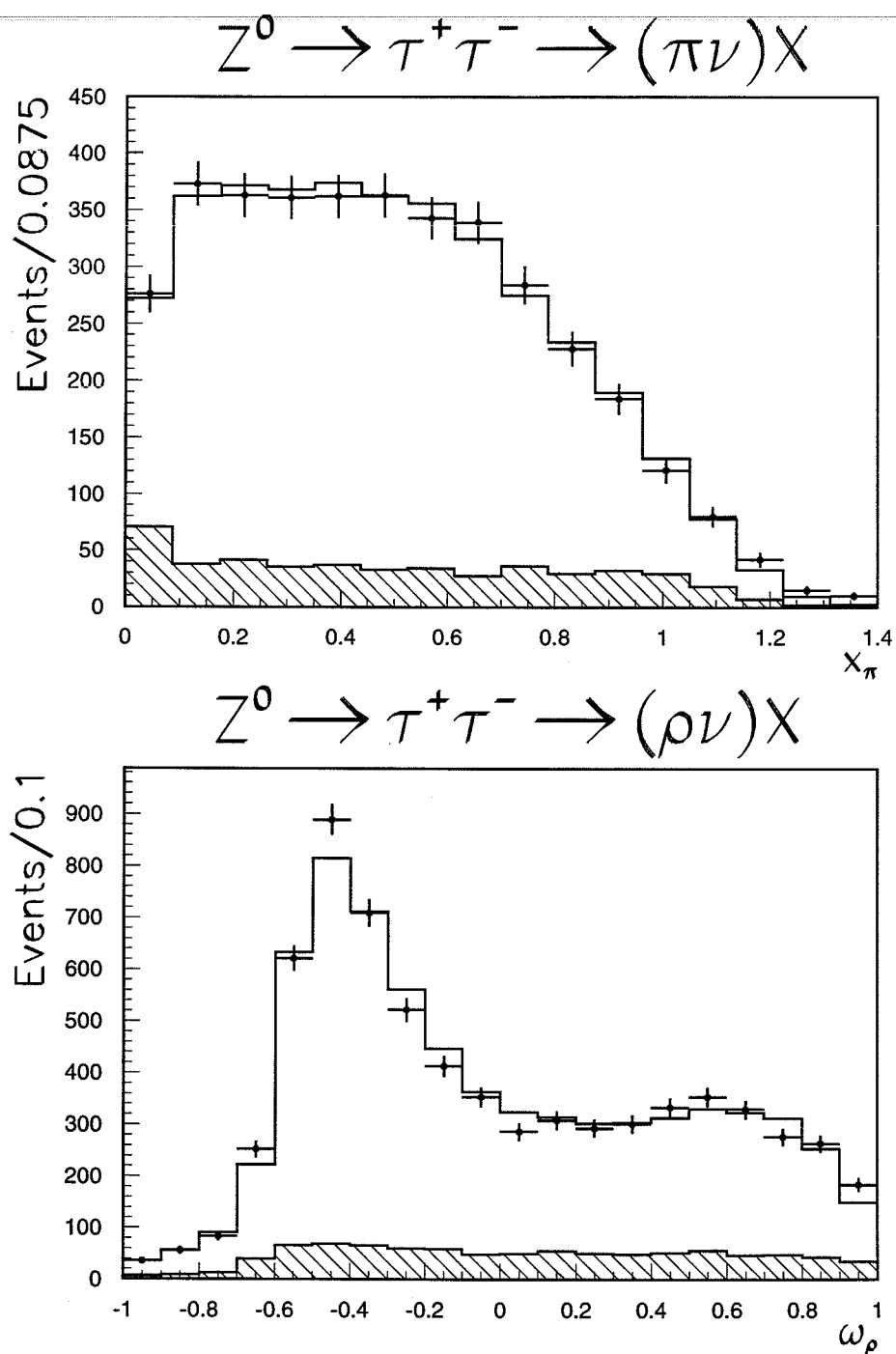


Figure 7.6: Distributions of x_π for the πX channel and ω_ρ for the ρX channel. The data are shown as points with statistical error bars. The solid-line histogram represents the result of the fit. Total background is superimposed as a hatched histogram.

$$Z^0 \rightarrow \tau^+ \tau^- \rightarrow (e\nu\nu)(e\nu\nu)$$

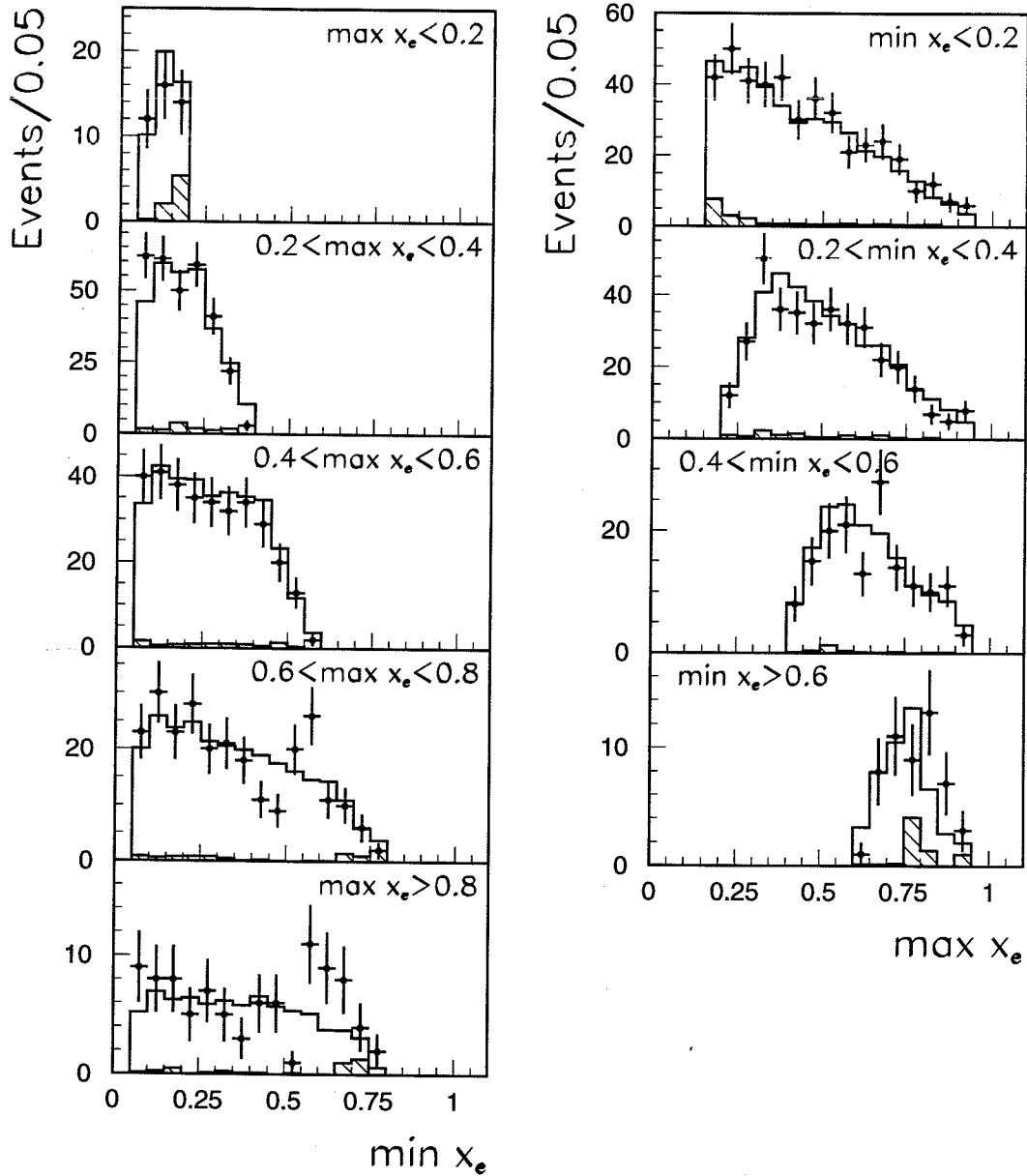


Figure 7.7: Distributions of x_e for the ee channel shown for five (four) slices of the distribution on the opposite hemisphere. The data are shown as points with statistical error bars. The solid-line histogram represents the result of the fit. Total background is superimposed as a hatched histogram.

$$Z^0 \rightarrow \tau^+ \tau^- \rightarrow (e\nu\nu)(\mu\nu\nu)$$

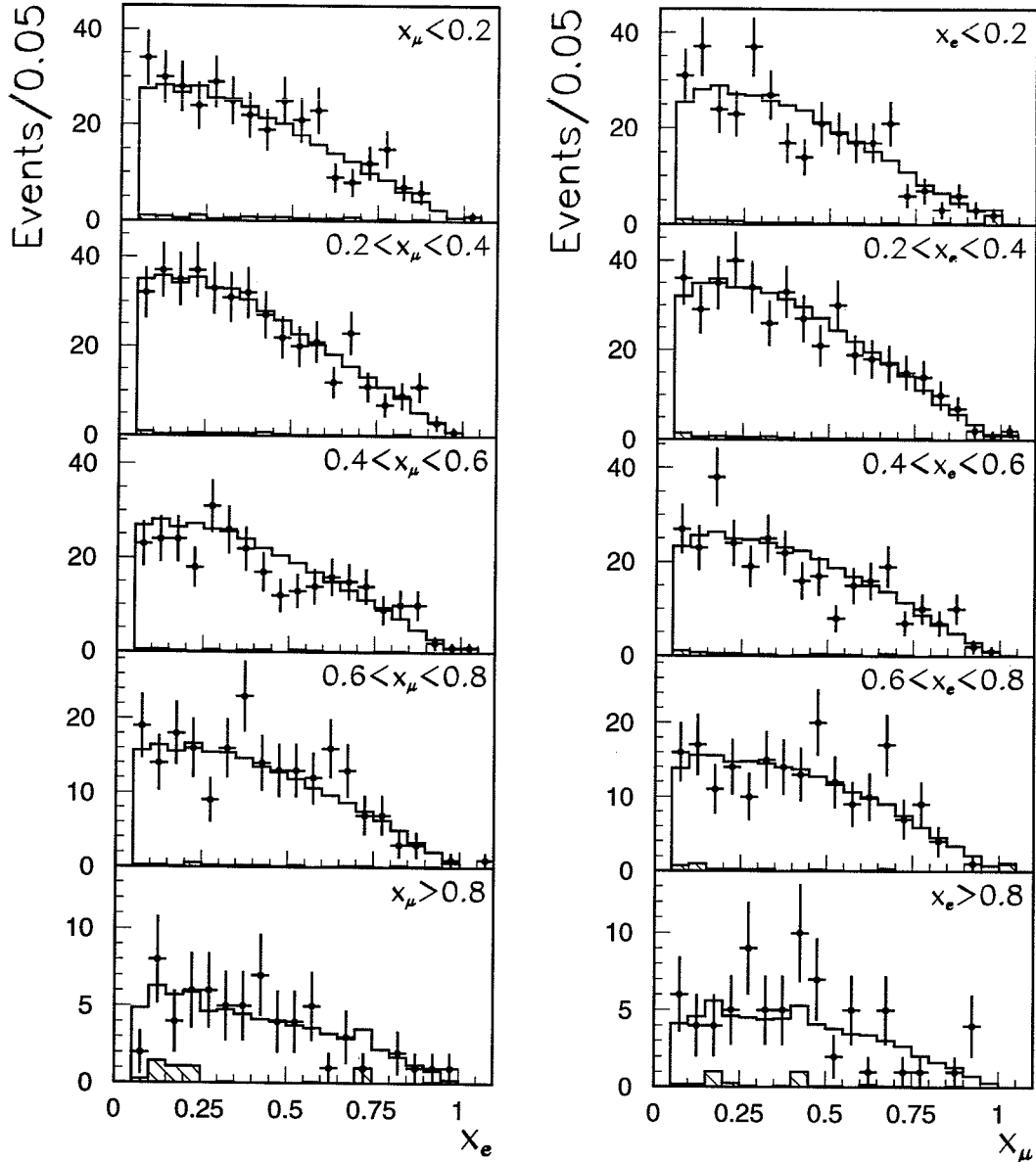


Figure 7.8: Distributions of x_e and x_μ for the $e\mu$ channel shown for five slices of the distribution on the opposite hemisphere. The data are shown as points with statistical error bars. The solid-line histogram represents the result of the fit. Total background is superimposed as a hatched histogram.

$$Z^0 \rightarrow \tau^+ \tau^- \rightarrow (e\nu\nu)(\pi\nu)$$

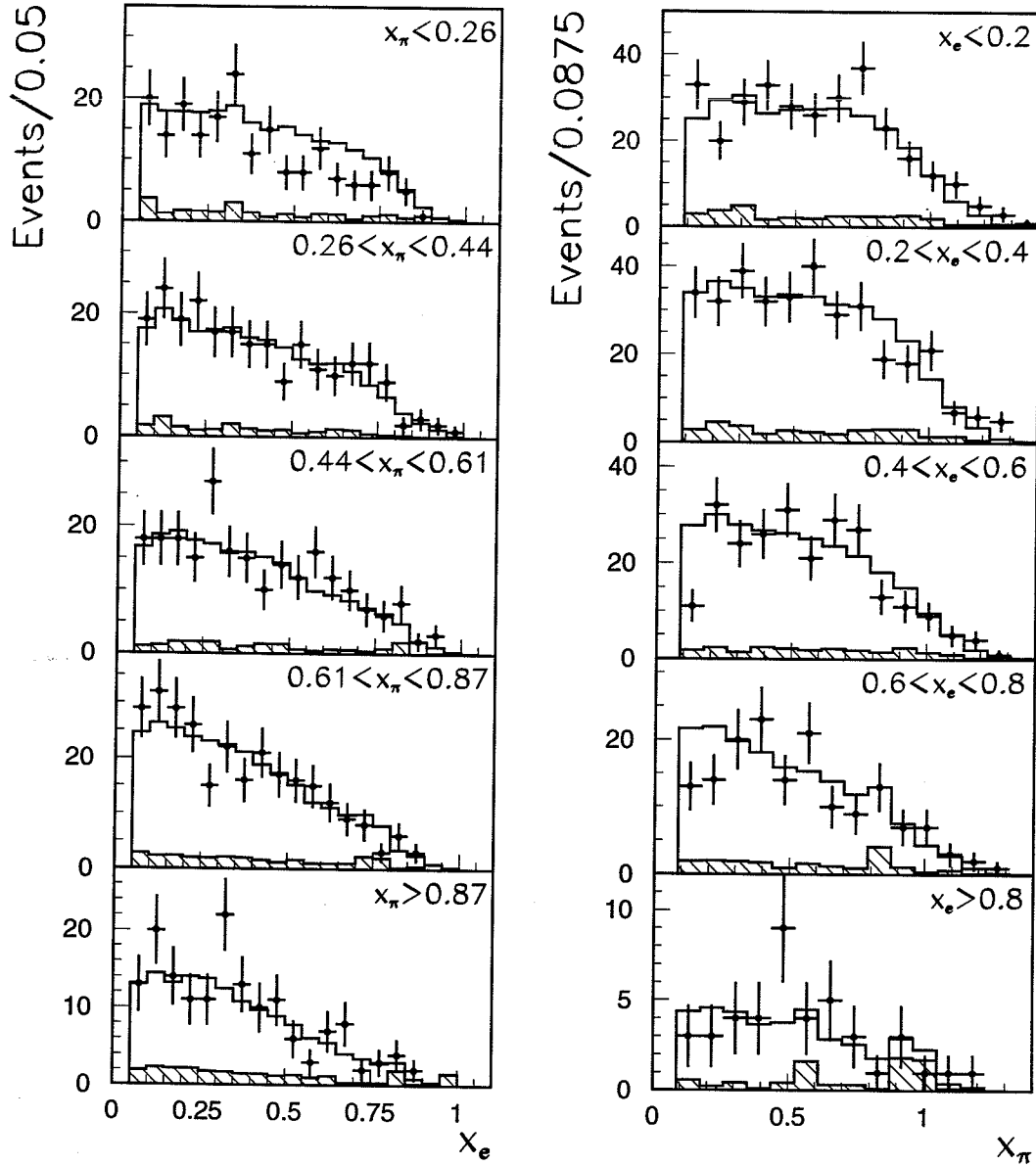


Figure 7.9: Distributions of x_e and x_π for the $e\pi$ channel shown for five slices of the distribution on the opposite hemisphere. The data are shown as points with statistical error bars. The solid-line histogram represents the result of the fit. Total background is superimposed as a hatched histogram.

$$Z^0 \rightarrow \tau^+ \tau^- \rightarrow (e\nu)(\rho\nu)$$

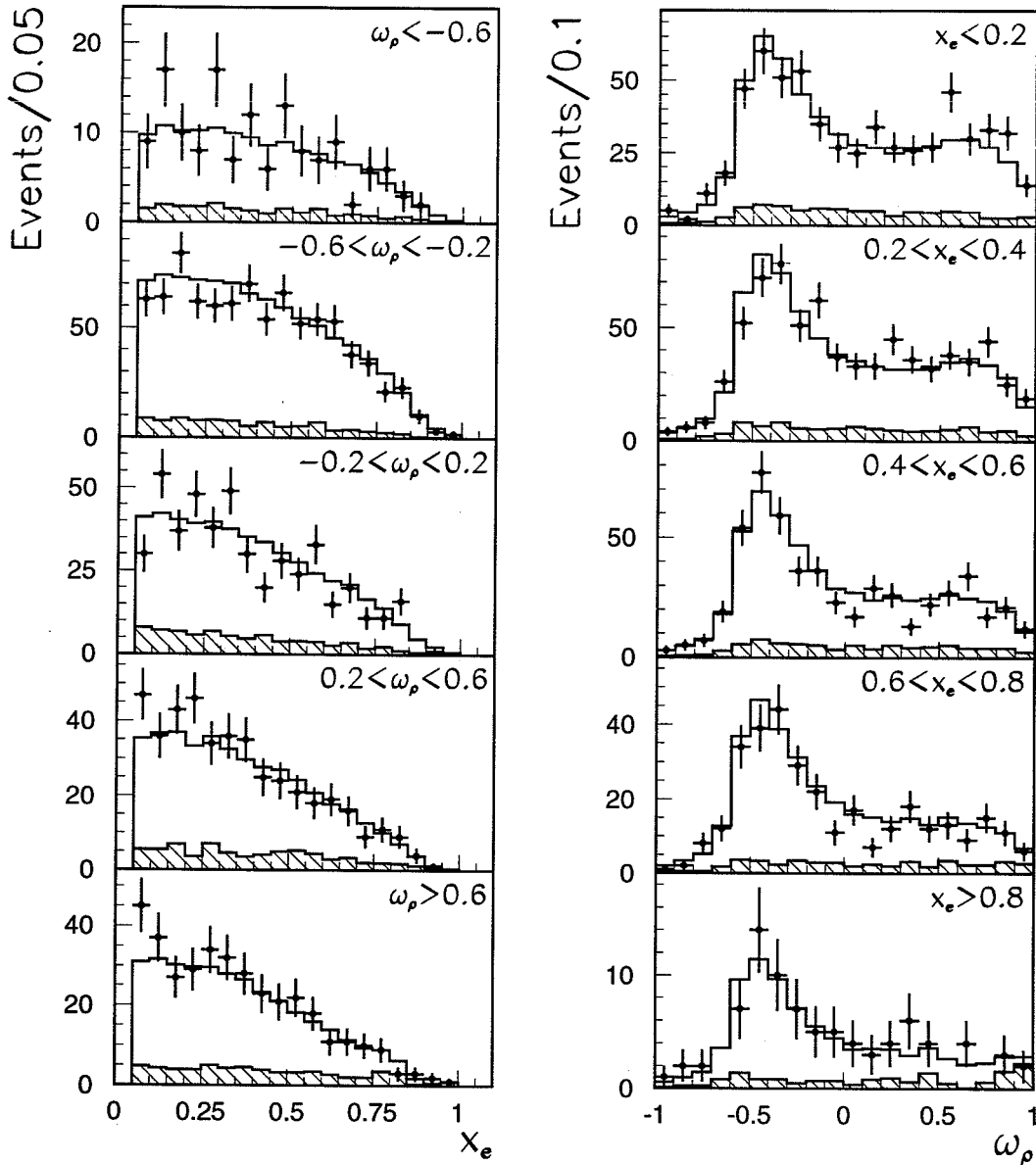


Figure 7.10: Distributions of x_e and ω_ρ for the $e\rho$ channel shown for five slices of the distribution on the opposite hemisphere. The data are shown as points with statistical error bars. The solid-line histogram represents the result of the fit. Total background is superimposed as a hatched histogram.

$$Z^0 \rightarrow \tau^+ \tau^- \rightarrow (\mu\nu\nu)(\pi\nu)$$

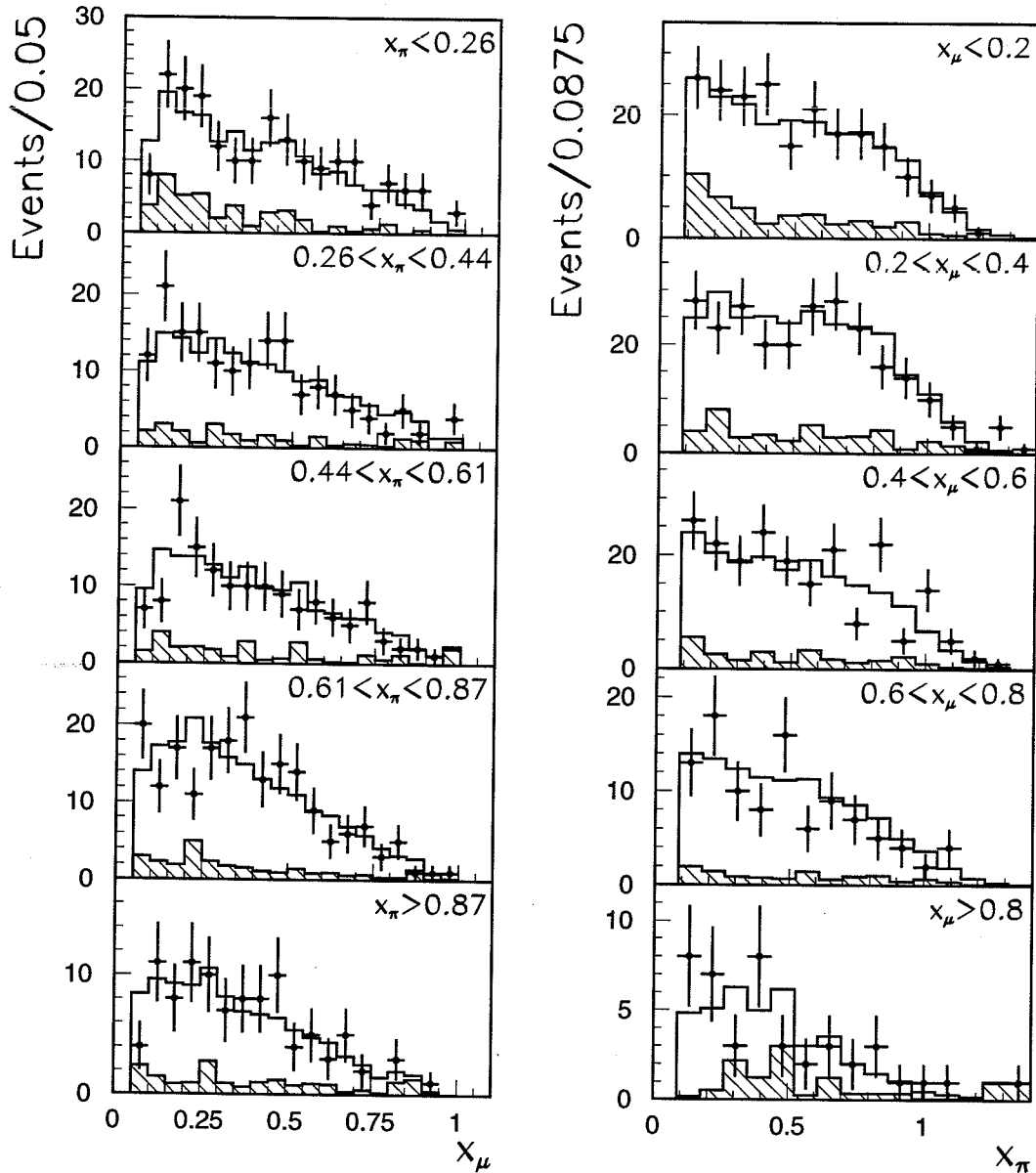


Figure 7.11: Distributions of x_μ and x_π for the $\mu\pi$ channel shown for five slices of the distribution on the opposite hemisphere. The data are shown as points with statistical error bars. The solid-line histogram represents the result of the fit. Total background is superimposed as a hatched histogram.

$$Z^0 \rightarrow \tau^+ \tau^- \rightarrow (\mu\nu\nu)(\rho\nu)$$

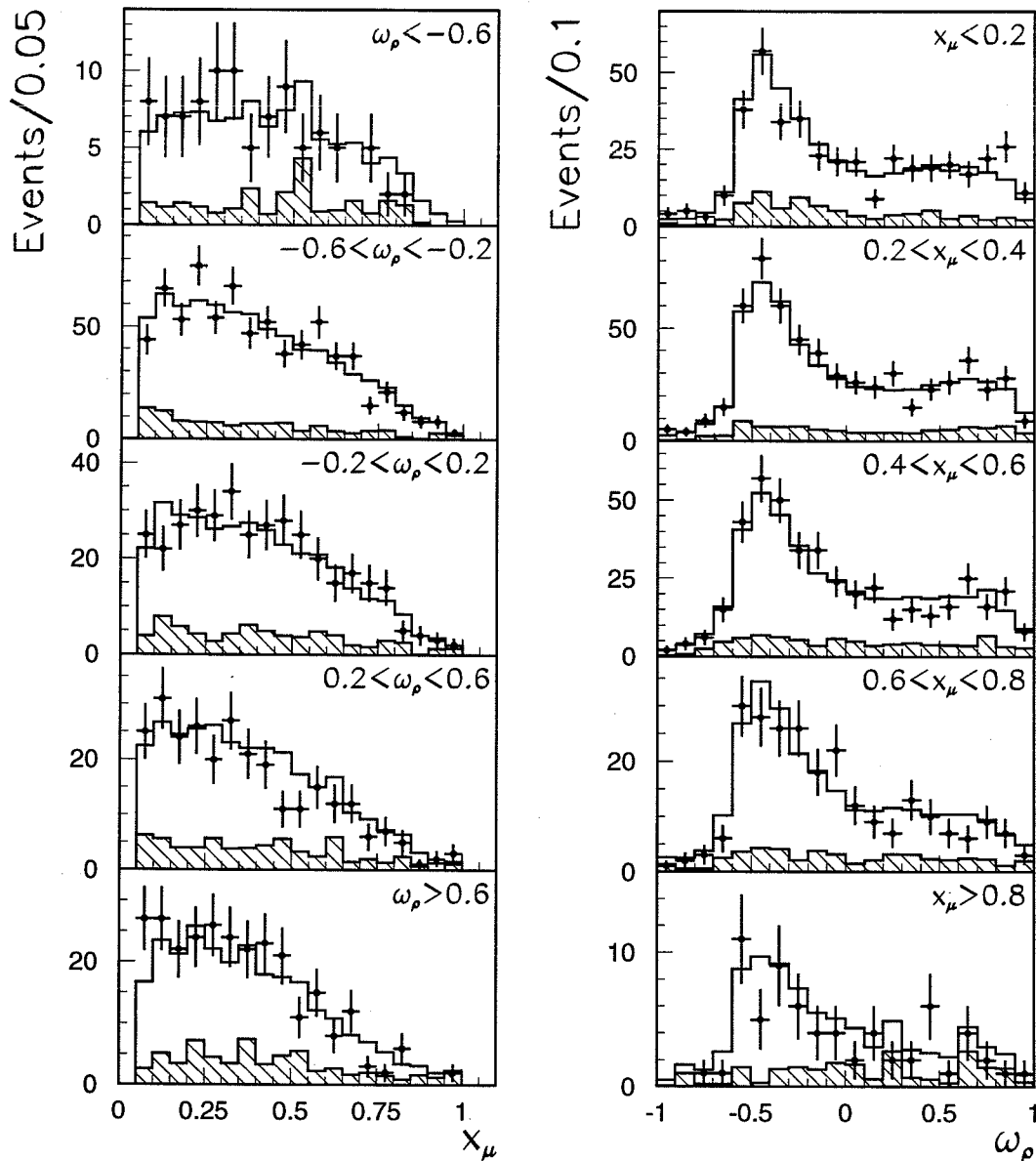


Figure 7.12: Distributions of x_μ and ω_ρ for the $\mu\rho$ channel shown for five slices of the distribution on the opposite hemisphere. The data are shown as points with statistical error bars. The solid-line histogram represents the result of the fit. Total background is superimposed as a hatched histogram.

$$Z^0 \rightarrow \tau^+ \tau^- \rightarrow (\pi\nu)(\pi\nu)$$

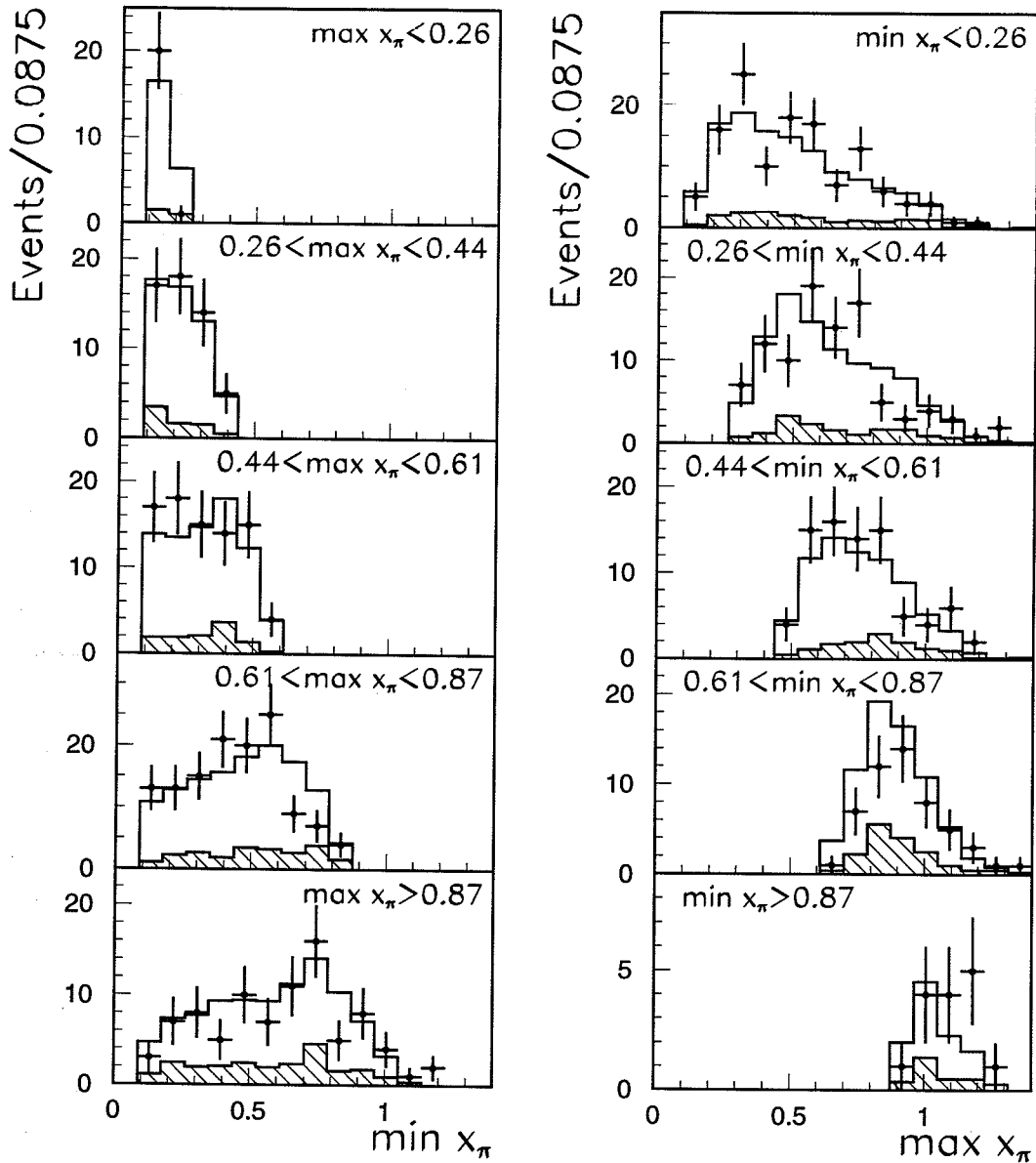


Figure 7.13: Distributions of x_π for the $\pi\pi$ channel shown for five slices of the distribution on the opposite hemisphere. The data are shown as points with statistical error bars. The solid-line histogram represents the result of the fit. Total background is superimposed as a hatched histogram.

$$Z^0 \rightarrow \tau^+ \tau^- \rightarrow (\pi\nu)(\rho\nu)$$

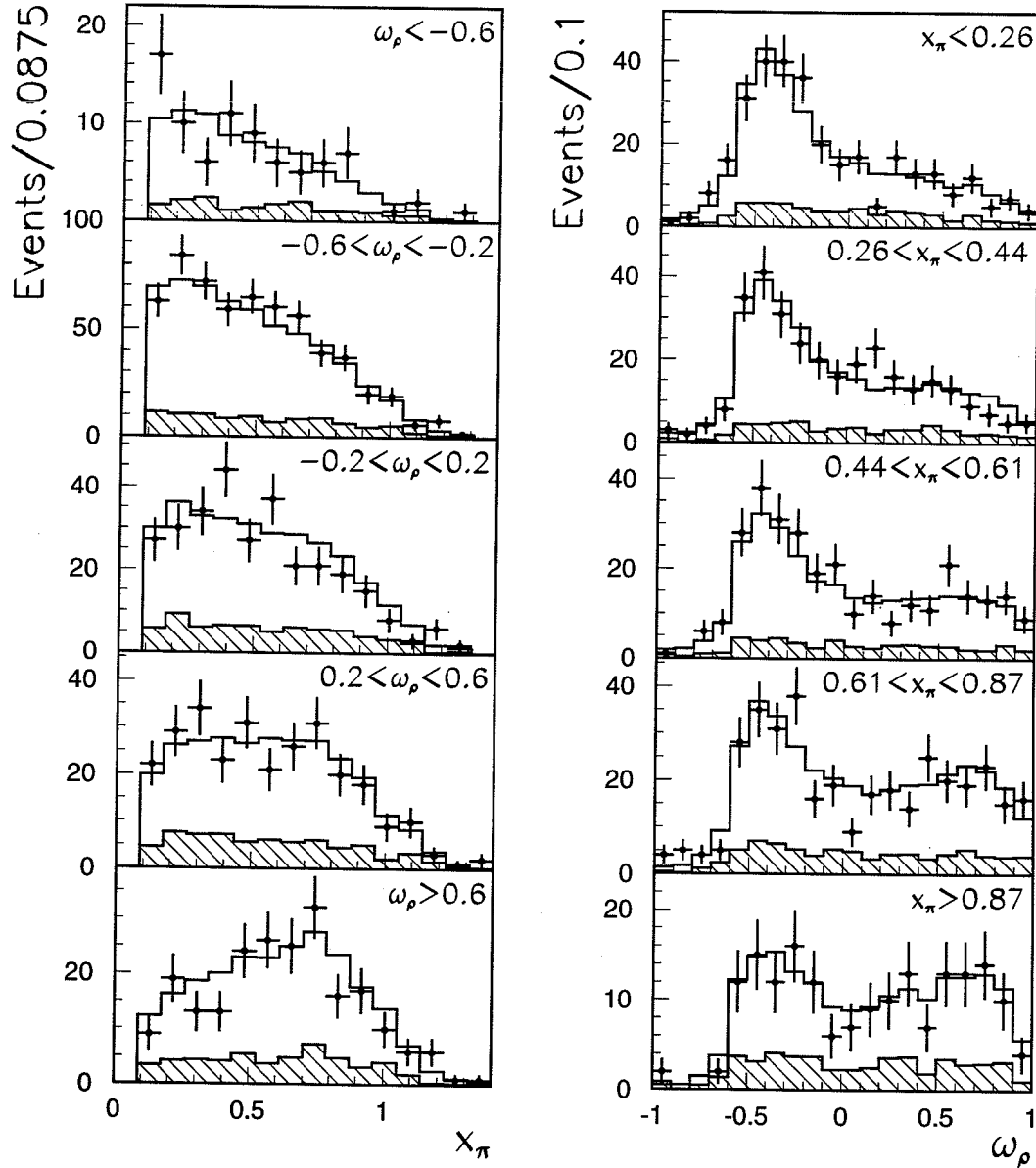


Figure 7.14: Distributions of x_π and ω_ρ for the $\pi\rho$ channel shown for five slices of the distribution on the opposite hemisphere. The data are shown as points with statistical error bars. The solid-line histogram represents the result of the fit. Total background is superimposed as a hatched histogram.

$$Z^0 \rightarrow \tau^+ \tau^- \rightarrow (\rho\nu)(\rho\nu)$$

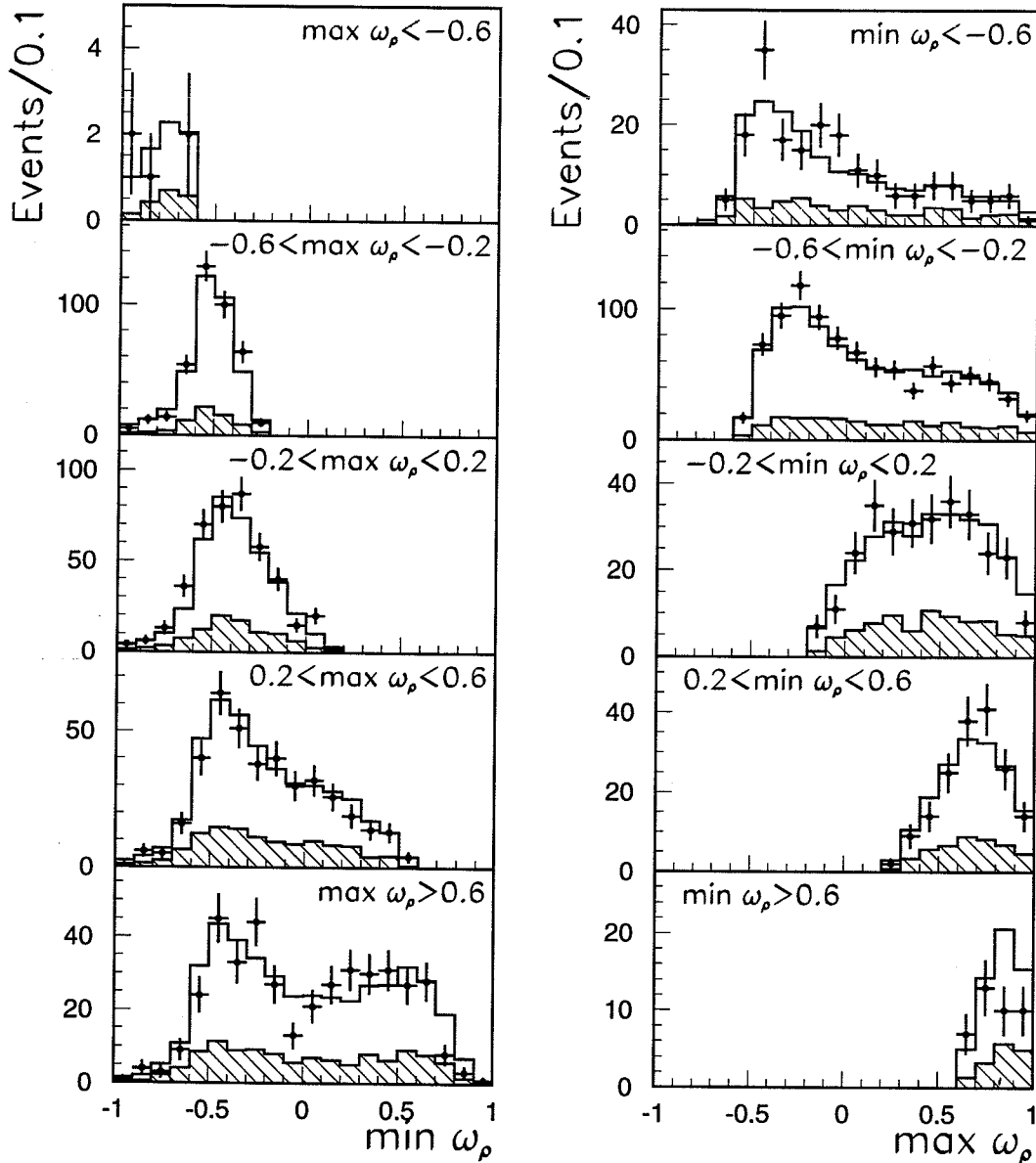


Figure 7.15: Distributions of ω_ρ for the $\rho\rho$ channel shown for five slices of the distribution on the opposite hemisphere. The data are shown as points with statistical error bars. The solid-line histogram represents the result of the fit. Total background is superimposed as a hatched histogram.

<i>Uncertainty</i>	ΔP_τ	$\Delta \rho_l$	$\Delta \eta_l$	$\Delta \xi_l$	$\Delta \xi_l \delta_l$	$\Delta \xi_h$
Event selection	0.006	0.007	0.014	0.016	0.010	0.007
non- τ backg. rate	0.003	0.011	0.025	0.051	0.038	0.004
τ branching ratios	0.005	0.009	0.007	0.031	0.030	0.011
Calibration	0.011	0.029	0.080	0.035	0.025	0.006
MC statistics	0.005	0.012	0.063	0.017	0.044	0.003
<i>Total</i>	0.015	0.035	0.106	0.073	0.071	0.016

Table 7.4: Systematic uncertainties on parameters of the fit, assuming universality in the τ decays.

<i>Uncertainty</i>	$\Delta \rho_e$	$\Delta \xi_e$	$\Delta \xi_e \delta_e$	$\Delta \rho_\mu$	$\Delta \xi_\mu$	$\Delta \xi_\mu \delta_\mu$	$\Delta \xi_\pi$	$\Delta \xi_\rho$
Event selection	0.004	0.009	0.007	0.001	0.010	0.010	0.005	0.013
non- τ backg. rate	0.006	0.035	0.034	0.007	0.063	0.021	0.002	0.006
τ branching ratios	0.008	0.009	0.026	0.005	0.037	0.018	0.010	0.019
Calibration	0.031	0.028	0.033	0.018	0.046	0.014	0.036	0.018
MC statistics	0.018	0.012	0.041	0.042	0.030	0.021	0.018	0.005
<i>Total</i>	0.037	0.048	0.068	0.046	0.092	0.039	0.042	0.030

Table 7.5: Systematic uncertainties on parameters of the fit, not assuming universality in the τ decays.

channel background spectra, is estimated by varying the branching ratios of τ decays within their errors in PDG94 [24], with the constraint that they sum to unity.

In order to estimate to which extent the uncertainty in the knowledge of the detector calibration influence fitted values, the scale of the BGO electromagnetic energy measurement, muon momentum reconstruction, p_t measurement in the TEC and calorimetric energy measurement for the charged pion has been varied. These scales are varied within their errors, described in Section 6.4.

The fit results depend on the uncertainty in the efficiencies ε , which are determined using the finite Monte Carlo sample. Another source of uncertainty due to the finite Monte Carlo sample is the distributions of the selected Monte Carlo $\tau \rightarrow \rho\nu$ decays, which are used in obtaining the $h_0^{(\rho)}$ and $h_1^{(\rho)}$ functions for the signal. These uncertainties were estimated by varying values of the efficiency and of the $h_0^{(\rho)}$ and $h_1^{(\rho)}$ functions in every bin within their statistical errors.

The summary of the systematic error study is given in Table 7.4 for the fit, assuming universality in τ decays, and in Table 7.5 for the fit not assuming universality in τ decays.

Chapter 8

Conclusions

8.1 Results

Using a data sample of 69 pb^{-1} integrated luminosity collected by the L3 detector during the 1991, 1992 and 1993 LEP runs, $Z^0 \rightarrow \tau^+\tau^-$ decays with at least one τ decaying into e, μ, π and ρ have been selected. Assuming only vector (g_V^τ) and axial-vector (g_A^τ) coupling constants in the τ pair production through the electroweak neutral current, the Michel parameters $\rho, \eta, \xi, \xi\delta$ and the average ν_τ helicity $\langle h_{\nu_\tau} \rangle$ in τ lepton decays have been measured. Their values together with the average τ lepton polarization $P_\tau = -\frac{2g_V^\tau g_A^\tau}{g_V^{\tau 2} + g_A^{\tau 2}}$ were derived from a binned maximum likelihood fit, performed simultaneously to the distributions of the τ pair decay products in the following channels: $ee, e\mu, e\pi, e\rho, eX, \mu\pi, \mu\rho, \mu X, \pi\pi, \pi\rho, \pi X, \rho\rho, \rho X$, where X designates a τ decay not identified as e, μ, π or ρ .

Using 32138 events, selected in each of the above channels, and assuming universality in τ lepton decays, the measured values are:

	<i>this measurement</i>	V-A
$\rho_l =$	$0.794 \pm 0.039 \pm 0.035$	0.75
$\eta_l =$	$0.25 \pm 0.17 \pm 0.11$	0
$\xi_l =$	$0.94 \pm 0.21 \pm 0.07$	1
$\xi_l \delta_l =$	$0.81 \pm 0.14 \pm 0.07$	0.75
$\langle h_{\nu_\tau} \rangle =$	$-0.970 \pm 0.053 \pm 0.016$	-1

and $P_\tau = -0.154 \pm 0.018 \pm 0.015$, where the first error is statistical and the second error is systematic. This measurement implies that the sign of P_τ is unambiguously defined by the LEP results on forward-backward polarization asymmetry [69, 70] and the SLD measurement of left-right asymmetry [71].

The measured values of $\rho_l, \eta_l, \xi_l, \delta_l \xi_l$ and $\langle h_{\nu_\tau} \rangle$ are in agreement with the V-A structure of the weak charged current interaction in τ lepton decays. In addition, this

measurement confirms that parity is violated both in τ pair production through the weak neutral current and in the τ lepton decay through the weak charged current.

Using this measurement only, an upper limit on the contribution of right-handed τ 's to the total τ decay has been determined. Following the Bayesian approach for obtaining one-sided limits [24], the upper limit

$$Q_R^\tau = \frac{1}{4}|g_{RR}^S|^2 + \frac{1}{4}|g_{LR}^S|^2 + |g_{RR}^V|^2 + |g_{LR}^V|^2 + 3|g_{LR}^T|^2 < 0.20$$

is set at 90% CL.

Not assuming e - μ universality in leptonic τ decays, and fitting the hadronic chirality parameter $\xi_h \equiv \langle h_{\nu_\tau} \rangle$ separately for $\tau \rightarrow \pi\nu$ and $\tau \rightarrow \rho\nu$ decays, the following values are obtained for $\rho_e, \xi_e, \xi_e\delta_e, \rho_\mu, \eta_\mu, \xi_\mu, \xi_\mu\delta_\mu, \xi_\pi, \xi_\rho$:

<i>this measurement</i>		<i>V-A</i>
$\rho_e = 0.778 \pm 0.042 \pm 0.037$	$\rho_\mu = 1.02 \pm 0.19 \pm 0.05$	0.75
	$\eta_\mu = 0.98 \pm 0.66 \pm 0.11$	0
$\xi_e = 0.82 \pm 0.25 \pm 0.05$	$\xi_\mu = 1.66 \pm 0.56 \pm 0.09$	1
$\xi_e\delta_e = 1.01 \pm 0.18 \pm 0.07$	$\xi_\mu\delta_\mu = 0.56 \pm 0.26 \pm 0.04$	0.75
$\xi_\pi = -0.911 \pm 0.084 \pm 0.042$	$\xi_\rho = -0.996 \pm 0.072 \pm 0.030$	-1

and $P_\tau = -0.155 \pm 0.018 \pm 0.015$, where the first error is statistical and the second error is systematic. This result confirms, within its present errors, the hypothesis of e - μ universality in the weak charged interaction in leptonic τ decays.

8.2 Outlook and Prospects

In conclusion, the LEP collider running at the Z^0 peak provides a clean source of polarized τ leptons, which are produced in the $Z^0 \rightarrow \tau^+\tau^-$ decay with opposite helicities. This allows, using the correlations of the τ pair decay products, to make a *simultaneous* measurement of the Michel parameters $\rho, \eta, \xi, \xi\delta$ and the average ν_τ helicity $\langle h_{\nu_\tau} \rangle$ in τ lepton decays. This measurement gives a possibility to test the V - A hypothesis for τ lepton decays and to check lepton universality in the weak charged interaction. The result of the measurement presented here shows no evidence for a deviation from the V - A structure in τ lepton decays and confirms lepton universality in the weak charged interaction.

This result is also in agreement with other recent measurements from the ARGUS [122, 123, 124, 125, 126] and the ALEPH [121] collaborations, which are summarized in Table 8.1 and Table 8.2.

The statistical precision of this measurement will be considerably increased in the future by including L3 data collected during the 1994 and the 1995 LEP runs. This will allow to test further the validity of the V - A hypothesis in the weak charged current interaction in τ lepton decays.

Measurement	Parameter	Measured Value	V-A
ARGUS [125]	ρ_l	$0.732 \pm 0.034 \pm 0.020$	0.75
ALEPH [121]		$0.751 \pm 0.039 \pm 0.022$	
L3 (<i>this measurement</i>)		$0.794 \pm 0.039 \pm 0.035$	
ARGUS [125]	η_l	$0.03 \pm 0.18 \pm 0.12$	0
ALEPH [121]		$-0.04 \pm 0.15 \pm 0.11$	
L3 (<i>this measurement</i>)		$0.25 \pm 0.17 \pm 0.11$	
ARGUS [126]	ξ_l	$1.26^{+0.30}_{-0.26} \pm 0.09$	1
ALEPH [121]		$1.18 \pm 0.15 \pm 0.06$	
L3 (<i>this measurement</i>)		$0.94 \pm 0.21 \pm 0.07$	
ARGUS [126]	$\xi_l \delta_l$	$0.77^{+0.18}_{-0.16} \pm 0.05$	0.75
ALEPH [121]		$0.88 \pm 0.11 \pm 0.07$	
L3 (<i>this measurement</i>)		$0.81 \pm 0.14 \pm 0.07$	
ARGUS [123, 124]	$\langle h_{\nu_\tau} \rangle$	$-1.022 \pm 0.028 \pm 0.030$	-1
ARGUS [126]		$-0.85^{+0.15}_{-0.17} \pm 0.05$	
ALEPH [121]		$-1.006 \pm 0.032 \pm 0.019$	
L3 (<i>this measurement</i>)		$-0.970 \pm 0.053 \pm 0.016$	

Table 8.1: Comparison of the results for ρ_l , η_l , ξ_l , $\xi_l \delta_l$ and $\xi_h \equiv \langle h_{\nu_\tau} \rangle$ of this measurement with other measurements.

Measurement	Parameter	Measured Value	V-A
ARGUS [125]	ρ_e	$0.735 \pm 0.036 \pm 0.020$	0.75
ALEPH [121]		$0.793 \pm 0.050 \pm 0.025$	
L3 (<i>this measurement</i>)		$0.776 \pm 0.042 \pm 0.037$	
ALEPH [121]	ξ_e	$1.03 \pm 0.23 \pm 0.09$	1
L3 (<i>this measurement</i>)		$0.82 \pm 0.25 \pm 0.05$	
ALEPH [121]	$\xi_e \delta_e$	$1.11 \pm 0.17 \pm 0.07$	0.75
L3 (<i>this measurement</i>)		$1.01 \pm 0.18 \pm 0.07$	
ARGUS [122]	ρ_μ	$0.734 \pm 0.055 \pm 0.027$	0.75
ALEPH [121]		$0.693 \pm 0.057 \pm 0.028$	
L3 (<i>this measurement</i>)		$1.02 \pm 0.19 \pm 0.05$	
ALEPH [121]	η_μ	$-0.24 \pm 0.23 \pm 0.18$	0
L3 (<i>this measurement</i>)		$0.98 \pm 0.66 \pm 0.11$	
ALEPH [121]	ξ_μ	$1.23 \pm 0.22 \pm 0.10$	1
L3 (<i>this measurement</i>)		$1.66 \pm 0.56 \pm 0.09$	
ALEPH [121]	$\xi_\mu \delta_\mu$	$0.71 \pm 0.14 \pm 0.06$	0.75
L3 (<i>this measurement</i>)		$0.56 \pm 0.26 \pm 0.04$	
ALEPH [121]	ξ_π	$-0.987 \pm 0.057 \pm 0.027$	-1
L3 (<i>this measurement</i>)		$-0.911 \pm 0.084 \pm 0.042$	
ALEPH [121]	ξ_ρ	$-1.045 \pm 0.058 \pm 0.032$	-1
L3 (<i>this measurement</i>)		$-0.996 \pm 0.072 \pm 0.030$	
ARGUS [123]	ξ_{a_1}	$-1.25 \pm 0.23^{+0.08}_{-0.15}$	-1
ALEPH [121]		$-0.937 \pm 0.116 \pm 0.064$	

Table 8.2: Comparison of the results for ρ , η , ξ , $\xi\delta$ and ξ_h without assuming universality in τ decays.

Bibliography

- [1] S. L. Glashow, *Nucl. Phys.* **22** (1961) 579
- [2] S. Weinberg, *Phys. Rev. Lett.* **19** (1967) 1264
- [3] A. Salam, in *Elementary Particle Theory: Relativistic Groups and Analyticity (Nobel Symposium No. 8)*, edited by N. Svartholm (Almquist and Wiksell, Stockholm, 1968), p. 367
- [4] W. Fetscher, H. J. Gerber and K. F. Johnson, *Phys. Lett. B* **173** (1986) 102
- [5] E. Rutherford, *Philos. Mag.* **42** (1898) 392
- [6] W. Pauli, American Physical Society Meeting, Pasadena, June 1931
- [7] E. Fermi, *Ric. Scient.* **4** (1934) 491; *Nuovo Cim.* **11** (1934) 1; *Z. Phys.* **88** (1934) 161
- [8] T. D. Lee and C. N. Yang, *Phys. Rev.* **104** (1956) 254
- [9] E. Ambler, R. W. Hayward, D. D. Hoppes, R. P. Hudson and C. S. Wu, *Phys. Rev.* **105** (1957) 1413; R. L. Garwin, L. M. Lederman and M. Weinrich *Phys. Rev.* **105** (1957) 1415; J. J. Friedman and V. L. Telegdi *Phys. Rev.* **105** (1957) 1681
- [10] R. P. Feynman and M. Gell-Mann, *Phys. Rev.* **109** (1958) 193; R. E. Marshak and E. C. G. Sudarshan *Phys. Rev.* **109** (1958) 1860; J. J. Sakurai *Nuovo Cim.* **7** (1958) 649;
- [11] C. N. Yang and R. L. Mills, *Phys. Rev.* **96** (1954) 191
- [12] J. Schwinger, *Ann. Phys. (N.Y.)* **2** (1957) 407
- [13] P. W. Higgs, *Phys. Rev. Lett.* **12** (1964) 508; *Phys. Rev.* **145** (1966) 1156
- [14] S. L. Glashow, J. Iliopoulos and L. Maiani, *Phys. Rev. D* **2** (1970) 1285
- [15] M. Gell-Mann, *Phys. Lett.* **8** (1964) 214
- [16] G. 't Hooft, *Nucl. Phys. B* **33** (1971) 173; *Nucl. Phys. B* **35** (1971) 167

- [17] F. J. Hasert *et al.*, *Phys. Lett. B* **46** (1973) 121; *Phys. Lett. B* **46** (1973) 138; *Nucl. Phys. B* **73** (1974) 1
- [18] G. Arnison *et al.* (UA1 Collaboration), *Phys. Lett. B* **122** (1983) 103; M. Banner *et al.* (UA2 Collaboration), *Phys. Lett. B* **122** (1983) 476; G. Arnison *et al.* (UA1 Collaboration), *Phys. Lett. B* **126** (1983) 398; P. Bagnaia *et al.* (UA2 Collaboration), *Phys. Lett. B* **129** (1983) 310
- [19] L. B. Okun, *Leptons and Quarks*, North-Holland, Amsterdam, 1982
- [20] F. Halzen and A. D. Martin, *Quarks and Leptons: An Introductory Course in Modern Particle Physics*, John Wiley & Sons, New York, NY, 1984
- [21] R. Alemany, N. Rius, J. Bernabéu, J. J. Gómez-Cadenas, A. Pich, *Nucl. Phys. B* **379** (1992) 3
- [22] N. Rius, *Análisis de la polarización del tau y correlaciones de espín a las energías de LEP*, Ph.D. Thesis, University of Valencia (1991)
- [23] J. Bernabéu, N. Rius and A. Pich, *Phys. Lett. B* **257** (1991) 219
- [24] M. Aguilar-Benitez *et al.*, *Review of Particle Properties*, *Phys. Rev. D* **50** (1994) 1173
- [25] The LEP Collaborations ALEPH, DELPHI, L3, OPAL and the LEP Electroweak Working Group, *Combined Preliminary Data on Z Parameters from the LEP Experiments and Constraints on the Standard Model*, CERN-PPE/94-187, 25 November 1994
- [26] D. Bardin *et al.*, Fortran package *ZFITTER*, CERN-TH 6443/92 (1992); D. Bardin *et al.*, *Zeit. Phys. C* **44** (1989) 493; D. Bardin *et al.*, *Nucl. Phys. B* **351** (1991) 1; D. Bardin *et al.*, *Phys. Lett. B* **255** (1991) 290
- [27] Y.-S. Tsai, *Phys. Rev. D* **4** (1971) 2821; *Erratum Phys. Rev. D* **13** (1976) 771
- [28] M. Consoli and W. Hollik, Electroweak radiative corrections for Z physics, in *Z Physics at LEP I*, edited by G. Altarelli, R. Kleiss, C. Verzegnassi, CERN Yellow Report 89-08, vol.1 (1989) p. 7
- [29] F. Berends, Z line shape, in *Z Physics at LEP I*, edited by G. Altarelli, R. Kleiss, C. Verzegnassi, CERN Yellow Report 89-08, vol.1 (1989) p. 89
- [30] M. L. Perl *et al.*, *Phys. Rev. Lett.* **35** (1975) 1489
- [31] M. L. Perl *et al.*, *Phys. Lett. B* **63** (1976) 466; G. L. Feldman *et al.*, *Phys. Rev. Lett.* **38** (1977) 117

- [32] J. Burmester *et al.*, *Phys. Lett. B* **68** (1977) 297,301; R. Brandelik *ite*, *Phys. Lett. B* **70** (1977) 125; R. Brandelik *ite*, *Phys. Lett. B* **73** (1978) 109
- [33] M. L. Perl *et al.*, *Phys. Lett. B* **70** (1977) 487
- [34] J. A. Jaros, *J. Physique* **43** Supp. C-3 (1982) 106
- [35] B. C. Barish and R. Stroynowski, *Phys. Rep.* **157** (1988) 1
- [36] BES Collaboration, J. Z. Bai *et al.*, *Measurement of the Mass of the Tau Lepton*, SLAC-PUB-95-6930 (July 1995), submitted to *Phys. Rev. D*
- [37] M. Davier, The τ leptonic current: lifetime, leptonic branching ratios and Michel parameters, in *Proceedings of the Third Workshop on Tau Lepton Physics*, Montreux, Switzerland, (19-22 September 1994), ed. by L. Rolandi, *Nucl. Phys. B (Proc. Suppl.)* **40** (1995) 395
- [38] B. K. Heltsley, Hadronic Decay Modes of the Tau Lepton: A TAU94 Review, in *Proceedings of the Third Workshop on Tau Lepton Physics*, Montreux, Switzerland, (19-22 September 1994), ed. by L. Rolandi, *Nucl. Phys. B (Proc. Suppl.)* **40** (1995) 413
- [39] ALEPH Collaboration, D. Buskulic *et al.*, *Phys. Lett. B* **349** (1995) 585
- [40] R. Stroynowski, Summary talk, in *Proceedings of the Third Workshop on Tau Lepton Physics*, Montreux, Switzerland, (19-22 September 1994), ed. by L. Rolandi, *Nucl. Phys. B (Proc. Suppl.)* **40** (1995) 569
- [41] L. Michel, *Proc. Phys. Soc. A* **63** (1950) 514; *ibid.* **63** (1950) 1371
- [42] C. Bouchiat and L. Michel, *Phys. Rev.* **106** (1957) 170
- [43] T. Kinoshita and A. Sirlin, *Phys. Rev.* **107** (1957) 593
- [44] T. Kinoshita and A. Sirlin, *Phys. Rev.* **108** (1957) 844
- [45] L. Okun and A. Rudik, *Zh. Eksp. Teor. Fiz.* **32** (1957) 627 [*Sov. Phys. - JETP* **6** (1957) 520]
- [46] M. Fierz, *Zeit. Phys.* **101** (1937) 553
- [47] F. Scheck, *Leptons, hadrons and nuclei*, North Holland, Amsterdam, 1983
- [48] W. Fetscher and H.-J. Gerber, Precision Measurements in Muon and Tau Decays, in *Precision Tests of the Standard Electroweak Model*, ed. by P. Langacker, World Scientific, Singapore, 1993; also ETHZ-IMP PR/93-1 (1993)

- [49] P. Langacker and D. London, *Phys. Rev. D* **39** (1989) 266
- [50] W. Fetscher, *Phys. Rev. D* **42** (1990) 1544
- [51] C. Greub, D. Wyler and W. Fetscher, *Phys. Lett. B* **324** (1994) 109; *Erratum Phys. Lett. B* **329** (1994) 526
- [52] W. J. Marciano and A. Sirlin, *Phys. Rev. Lett.* **61** (1988) 1815
- [53] A. Rougé, ALEPH Note 88-15 (1988)
- [54] A. Rougé, *Zeit. Phys. C* **48** (1990) 75
- [55] K. Hagiwara, A. D. Martin and D. Zeppenfeld, *Phys. Lett. B* **235** (1990) 198
- [56] S. Kawasaki, T. Shirafuji and Y.S. Tsai, *Prog. Theor. Phys.* **49** (1972) 1773
- [57] S. Y. Pi, A. I. Sanda, *Ann. Phys. (N. Y.)* **106** (1977) 177
- [58] S. Jadach, Z. Wąs, *Acta Physica Polonica* **B15** (1151) 1984; *Erratum Acta Physica Polonica* **B16** (483) 1985
- [59] Charles A. Nelson, *Phys. Rev. D* **40** (1989) 123; *Erratum Phys. Rev. D* **41** (1990) 2327
- [60] J. J. Gómez-Cadenas, in *Proceedings of Tau-Charm Factory Workshop*, SLAC Report 343 (1989) p.89
- [61] A. Rougé, Tau decays as polarization analysers, in *Proceedings of Workshop on Tau Lepton Physics, Orsay, 1990*, edited by M. Davier and B. Jean-Marie, Editions Frontières (1991), p.213
- [62] S. Jadach, B. F. L. Ward and Z. Wąs, *Comp. Phys. Comm.* **66** (1991) 276
- [63] S. Jadach, J. H. Kühn and Z. Wąs, *Comp. Phys. Comm.* **64** (1991) 275
- [64] M. Schmidtler, *A Convenient Parametrization for the General Matrix Element of Leptonic Tau Decay*, University Karlsruhe Preprint IEKP-KA/93-14, July 1993
- [65] M. Davier, L. Duflot, F. Le Diberder, A. Rougé, *Phys. Lett. B* **306** (1993) 411
- [66] J. H. Kühn and E. Mirkes, *Zeit. Phys. C* **56** (1992) 661
- [67] R. Barlow, *Nucl. Instrum. Methods A* **297** (1990) 496
- [68] F. James and M. Roos, *MINUIT – Function Minimization and Error Analysis*, CERN Program Library, D506

- [69] ALEPH Collaboration, D. Buskulic *et al.*, *Zeit. Phys. C* **59** (1993) 369
- [70] L3 Collaboration, M. Acciarri *et al.*, *Phys. Lett. B* **341** (1994) 245
- [71] SLD Collaboration, K. Abe *et al.*, *Phys. Rev. Lett.* **70** (1993) 2515
- [72] I. Wilson and H. Henke, *The LEP Main Ring Accelerating Structure*, CERN Yellow Report 89-09 (1989); S. Myers, *The LEP Collider, from design to approval and commissioning*, CERN Yellow Report 91-08 (1991)
- [73] *Report of the Working Group on High Luminosity at LEP*, edited by E. Blucher *et al.*, CERN Yellow Report 91-02 (1991)
- [74] L3 Collaboration, B. Adeva *et al.*, *Nucl. Instrum. Methods A* **289** (1990) 35
- [75] L3 Collaboration, O. Adriani *et al.*, *Phys. Rep.* **236** (1993) 1
- [76] B. Adeva *et al.*, *Nucl. Instrum. Methods A* **277** (1989) 187; B. Adeva *et al.*, *Nucl. Instrum. Methods A* **323** (1992) 109
- [77] P. Duinker *et al.*, *Nucl. Instrum. Methods A* **273** (1988) 814
- [78] Riccardo de Asmundis, Ian J. Scott and Rajesh K. Sehgal, *The 1989 L3 Muon Chamber Test Beam Results*, L3 Note 907, March 1991
- [79] M. Cerrada *et al.*, *Nucl. Instrum. Methods A* **263** (1988) 343
- [80] R. Fabbretti *et al.*, *Nucl. Instrum. Methods A* **280** (1989) 13
- [81] F. Hartjes, J. Konijn, Y. Peng, *Nucl. Instrum. Methods A* **269** (1988) 544; *Straight line calibration in drift chambers over 8-meters*, NIKHEF-H/87-21, Nov. 1987; B. Adeva *et al.*, *Nucl. Instrum. Methods A* **289** (1990) 335
- [82] A. Arefiev *et al.*, *Nucl. Instrum. Methods A* **285** (1989) 403
- [83] S. Burov *et al.*, CERN-EP/88-84 (1988)
- [84] A. Arefiev *et al.*, *Nucl. Instrum. Methods A* **288** (1990) 364
- [85] O. Adriani *et al.*, *Nucl. Instrum. Methods A* **302** (1991) 53
- [86] Properties of the BGO crystals could be found in e.g. K. Hikasa *et al.*, *Review of Particle Properties*, *Phys. Rev. D* **45** (1992) III.24
- [87] J. Wenniger, *Measure de parametres electro-faibles du Z^0 avec le reaction $e^+e^- \rightarrow e^+e^-(\gamma)$* , Ph.D. Thesis, Université de Genève (1992)
- [88] A. Bay *et al.*, *Nucl. Instrum. Methods A* **321** (1992) 119

- [89] J. A. Bakken *et al.*, *Nucl. Instrum. Methods A* **275** (1989) 81
- [90] J. A. Bakken *et al.*, *Nucl. Instrum. Methods A* **343** (1994) 456
- [91] S. Jézéquel and Y. Karyotakis, *Results of the χ_{BGO}^2 method for the selection of the electromagnetic bumps*, L3 Note 1272, Sep. 1992
- [92] J. A. Bakken *et al.*, *Nucl. Instrum. Methods A* **254** (1987) 535; 1987-1988 L3 BGO Collaboration, *Calibration of the L3 electromagnetic calorimeter in electron beam*, L3 Note 1712, March 1995
- [93] H. Akbari *et al.*, *Nucl. Instrum. Methods A* **315** (1992) 161
- [94] F. Beissel *et al.*, *Nucl. Instrum. Methods A* **332** (1993) 33
- [95] K. Deiters *et al.*, *Nucl. Instrum. Methods A* **323** (1992) 162
- [96] H. Akbari *et al.*, *Nucl. Instrum. Methods A* **302** (1991) 415
- [97] G. Alverson *et al.*, *The Performance of the L3 Plastic Scintillating Fibre System in 1990 and 1991 LEP runs*, L3 Note 1105, Feb. 1992
- [98] T. Angelov *et al.*, *Nucl. Instrum. Methods A* **306** (1991) 536
- [99] IEEE Standart Fastbus Modular High-Speed Data Acquisition and Control System, Hardware: IEEE Std. 960-1989, Software: IEEE Std. 1177-1989
- [100] H. Müller *et al.*, CERN-EP/Electronics Note 87-04
- [101] L. Pregernig, *IEEE Trans. Nucl. Sci.* NS-**33** (1986) 797
- [102] H. Müller, *IEEE Trans. Nucl. Sci.* NS-**33** (1986) 819
- [103] H. Müller, *IEEE Trans. Nucl. Sci.* NS-**37** (1990) 361
- [104] R. Bizzarri *et al.*, *Nucl. Instrum. Methods A* **317** (1992) 463; P. Bagnaia *et al.*, *Nucl. Instrum. Methods A* **324** (1993) 101
- [105] P. Béné *et al.*, *Nucl. Instrum. Methods A* **306** (1991) 150
- [106] M. Fukushima, *L3 Level-1 Muon Trigger*, L3 Note 515, 1987; T. S. Dai and M. Fukushima, *L3 Level-1 Muon Trigger*, L3 Note 668, 1989
- [107] U. Uwer, *The L3 Scintillation Counter System*, L3 Note 1400, 1993
- [108] L3 Collaboration, M. Acciarri *et al.*, *Zeit. Phys. C* **62** (1994) 551

- [109] Y. Bertsch *et al.*, *Nucl. Instrum. Methods A* **340** (1994) 309; S. P. Beingessner *et al.*, *Nucl. Instrum. Methods A* **340** (1994) 322
- [110] P. Bähler *et al.*, CERN-DD/85-15, (1985)
- [111] M. Bourquin *et al.*, *Nucl. Instrum. Methods A* **325** (1993) 509
- [112] C. Dionisi *et al.*, *Nucl. Instrum. Methods A* **336** (1993) 78
- [113] P. F. Kunz *et al.*, in *Proceedings of "Three-day in-depth Review on the Impact of Specialized Processors in Elementary Particle Physics"*, Padova, Italy (1983)
- [114] The L3 detector simulation is based on the GEANT 3.14 program (R. Brun *et al.*, *GEANT 3*, CERN report DD/EE/84-1, Revised Sept. 1987). The GHEISHA program (H. Fesefeldt, RWTH Aachen report PITHA 85/02, 1985) is used to simulate hadronic interactions.
- [115] L3 Collaboration, O. Adriani *et al.*, *Phys. Lett. B* **294** (1992) 466
- [116] O. Adriani, S. Kirsch, A. Kunin, T. Paul, M. Pieri, J. Shukla and I. Vorobiev, *A Measurement of τ Polarization at LEP*, L3 Note 1637, 1994
- [117] Y. Karyotakis, *The L3 Electromagnetic Calorimeter*, a talk on the Calorimetry Symposium, Beijing, October 25-27, 1994
- [118] I. J. Scott, *A Measurement of the Polarization of the Tau Leptons in Z Decays with the L3 Detector at LEP*, Ph.D. Thesis, Harvard University (1993)
- [119] T. C. Paul, *A Measurement of Tau Lepton Polarization Using the L3 Detector at LEP*, Ph.D. Thesis, The Johns Hopkins University (1994)
- [120] R. Barlow, *Statistics*, John Wiley & Sons, Chichester, 1989
- [121] ALEPH Collaboration, D. Buskulic *et al.*, *Phys. Lett. B* **346** (1995) 379
- [122] ARGUS Collaboration, H. Albrecht *et al.*, *Phys. Lett. B* **246** (1990) 278
- [123] ARGUS Collaboration, H. Albrecht *et al.*, *Phys. Lett. B* **250** (1990) 164; *Zeit. Phys. C* **58** (1993) 61
- [124] ARGUS Collaboration, H. Albrecht *et al.*, *Phys. Lett. B* **337** (1994) 383
- [125] ARGUS Collaboration, H. Albrecht *et al.*, *Phys. Lett. B* **341** (1995) 441
- [126] ARGUS Collaboration, H. Albrecht *et al.*, *Phys. Lett. B* **349** (1995) 576